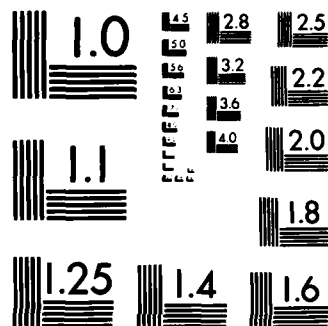


AD-A155 434 SOLAR ADAPTIVE OPTICS(U) ADAPTIVE OPTICS ASSOCIATES INC 1/2
CAMBRIDGE MA A WIRTH ET AL. SEP 84 AFGL-TR-84-0262
F19628-82-C-0035



MICROCOPY RESOLUTION TEST CHART
NATIONAL BUREAU OF STANDARDS-1963-A

AD-A155 434

AFGL-TR-84-0262

SOLAR ADAPTIVE OPTICS

Allan Wirth
Richard Ruquist

Adaptive Optics Associates, Inc.
2336 Massachusetts Avenue
Cambridge, MA 02140

Final Report
17 March 1982 - 30 September 1984

September 1984

Approved for public release; distribution unlimited

AIR FORCE GEOPHYSICS LABORATORY
AIR FORCE SYSTEMS COMMAND
UNITED STATES AIR FORCE
HANSCOM AFB, MASSACHUSETTS 01731

DTIC FILE COPY


DTIC
ELECTE
JUN 25 1985
S
4
B
D

85 06 10 11 2

(2)

This report has been reviewed by the ESD Public Affairs Office (PA) and is releasable to the National Technical Information Service (NTIS).

This technical report has been reviewed and is approved for publication.



Richard R. Radick
Contract Manager



STEPHEN L. KEIL
Branch Chief

FOR THE COMMANDER



RITA C. SAGALYN

Division Director

Qualified requestors may obtain additional copies from the Defense Technical Information Center. All others should apply to the National Technical Information Service.

If your address has changed, or if you wish to be removed from the mailing list, or if the addressee is no longer employed by your organization, please notify AFGL/DAA, Hanscom AFB, MA 01731. This will assist us in maintaining a current mailing list.

Do not return copies of this report unless contractual obligations or notices on a specific document require that it be returned.

Unclassified

SECURITY CLASSIFICATION OF THIS PAGE

REPORT DOCUMENTATION PAGE

1a. REPORT SECURITY CLASSIFICATION Unclassified		1b. RESTRICTIVE MARKINGS	
2a. SECURITY CLASSIFICATION AUTHORITY		3. DISTRIBUTION/AVAILABILITY OF REPORT Approved for public release; distribution unlimited	
2b. DECLASSIFICATION/DOWNGRADING SCHEDULE			
4. PERFORMING ORGANIZATION REPORT NUMBER(S)		5. MONITORING ORGANIZATION REPORT NUMBER(S) AFGL-TR-84-0262	
6a. NAME OF PERFORMING ORGANIZATION Adaptive Optics Assoc., Inc.	6b. OFFICE SYMBOL (If applicable)	7a. NAME OF MONITORING ORGANIZATION	
6c. ADDRESS (City, State and ZIP Code) 2336 Massachusetts Avenue Cambridge, MA 02140		7b. ADDRESS (City, State and ZIP Code)	
8a. NAME OF FUNDING/SPONSORING ORGANIZATION Air Force Geophysics Laboratory	8b. OFFICE SYMBOL (If applicable)	9. PROCUREMENT INSTRUMENT IDENTIFICATION NUMBER F19628-82-C-0035	
8c. ADDRESS (City, State and ZIP Code) Hanscom AFB, MA 01731		10. SOURCE OF FUNDING NOS.	
11. TITLE (Include Security Classification) Solar Adaptive Optics		PROGRAM ELEMENT NO. 61102F	PROJECT NO. 2311
		TASK NO. G3	WORK UNIT NO. CI
12. PERSONAL AUTHOR(S) Allan Wirth, Richard Rugquist			
13a. TYPE OF REPORT Final	13b. TIME COVERED FROM 17 Mar 82 TO 30 Sept 84	14. DATE OF REPORT (Yr., Mo., Day) 1984 September	15. PAGE COUNT 110
16. SUPPLEMENTARY NOTATION			
17. COSATI CODES		18. SUBJECT TERMS (Continue on reverse if necessary and identify by block number)	
FIELD	GROUP	SUB. GR.	
		Solar astronomy Imaging	
		Adaptive optics Atmospheric compensation	
19. ABSTRACT (Continue on reverse if necessary and identify by block number) The problem of imaging the solar surface is considered. A theoretical study is presented that indicates that traditional adaptive optic techniques are of limited usefulness for solar imaging. A new method for adaptive optic image sharpening for extended sources is described. Results from numerical simulations show that this technique shows promise for image sharpening under conditions of moderately severe turbulence.			
20. DISTRIBUTION/AVAILABILITY OF ABSTRACT UNCLASSIFIED/UNLIMITED <input type="checkbox"/> SAME AS RPT. <input checked="" type="checkbox"/> DTIC USERS <input type="checkbox"/>		21. ABSTRACT SECURITY CLASSIFICATION Unclassified	
22a. NAME OF RESPONSIBLE INDIVIDUAL Richard R. Radick		22b. TELEPHONE NUMBER (Include Area Code) 617-861-3227	22c. OFFICE SYMBOL PHS

SUMMARY OF SOLAR ADAPTIVE OPTICS PROJECT

This program consists of several parts. The first is a theoretical study of the problem of applying adaptive optical atmospheric correction to solar imaging. The results of this work show that, under typical daytime conditions, traditional adaptive optic methods will produce only very marginal improvement of image quality. The basic problem is quite simple to understand. As the strength of the atmospheric turbulence increases, the size of the region over which the aberration of the incoming wavefront may be approximated by a plane wave decreases. Since the size of the subapertures of a wavefront sensor must be comparable to the size of these regions, the required subaperture size also decreases. In sufficiently strong turbulence, this size may become small enough that the diffraction limit of the subapertures exceeds the isoplanatic angle. In other words, light reaching a point in the image plane of the subaperture may have come along paths experiencing different aberrations. This means that the wavefront is no longer approximately flat. Thus, any wavefront sensor depending upon subapertures will not work under these conditions. Based upon the available atmospheric data, typical daytime conditions at Sac Peak National Observatory (SPNO) place solar imaging in this regime.

The second part of this program consists of the identification of an approach to solar image correction that utilizes the full aperture of the telescope. Such a technique would not suffer from the problem outlined above. One such method has been found that shows promise; it is related to the multi-dither process of image sharpening. Simply, the incoming wavefront has added to it controlled amounts of various aberrations. The image quality is sensed and an error signal derived that allows iterative corrections to the wavefront to be determined. The measure of the image quality that is used is an integrated power spectrum of the →

image plane distribution. It is shown that quantity is maximized for an unaberrated input wave.

Finally, numerical simulations of this proposed image sharpening technique are used to show that it is possible to achieve very significant improvements in the resolution of a telescope under conditions of moderate turbulence. Typically, a fivefold reduction in spot size is possible in as few as five iterations. Translated into the performance of a real telescope, this is equivalent to an improvement of the resolution to within 10% of the theoretical diffraction limit. Further, it is shown that this system could be realized with existing processing technology.

Accession For	
NOIS DATA	<input checked="checked" type="checkbox"/>
NOIS 1/2	<input type="checkbox"/>
NOIS 1/4	<input type="checkbox"/>
Distribution/	
Availability Codes	
Dist	Special
A-1	



TABLE OF CONTENTS

	<u>Page</u>
SUMMARY OF SOLAR ADAPTIVE OPTICS PROJECT.	iii
LIST OF FIGURES/TABLES.	vii
SECTION I INTRODUCTION.	1
1.1 History of the program	1
II ADAPTIVE OPTIC LIMITATIONS FOR SOLAR IMAGING	3
2.1 Introduction	3
2.2 The Basic Principles of Adaptive Optics.	5
2.3 Characterization of the Turbulent Atmosphere	9
2.4 Wavefront Error Analysis of an Ideal Adaptive Optic System.	26
2.5 Extended Images.	27
2.6 Stellar And Solar Point-Like Images.	35
2.7 Solar Adaptive Optics Using LSI ³ Wavefront Sensor	40
2.8 LSI ³ Edge Tracker.	45
2.9 The LSI ³ Sensor.	46
2.10 Diffraction Effects.	52
2.11 LSI ³ Algorithm	53
III MODS FULL-APERTURE IMAGE SHARPENING	57
3.1 Full Aperture Extended Object Error Signal Algorithm.	57
3.2 MODS Servo System	60
3.3 Numerical Simulation of MODS.	63
IV RESULTS OF MODS SIMULATION.	71

4.1	Tests of Simulation Code	71
4.2	Tests of the Loop Simulation	77
4.3	Performance on Imaging Extended Objects. .	81
4.4	Summary.	82
V	CONCLUSIONS.	96
5.1	Description of Solar Adaptive Optics Project	96
5.2	Real Time MODS Operation.	96

LIST OF FIGURES AND TABLES

<u>Figure No.</u>		<u>Page</u>
1.	Model of coherence properties of the turbulent atmosphere.	8
2.	Maui Observatory Scintillometer C_n^2 Measurements and Modeling.	12
3.	Land Based (Continental) C_n^2 Models.	13
4.	In-Situ Balloon C_n^2 Measurements over Continental Europe.	14
5.	White Sands In-Situ Aircraft Daytime C_n^2 Measurements(Single Realization).	17
6a.	White Sands In-Situ Aircraft Daytime C_n^2 Measurements(Single Realization)	18
6b.	White Sands In-Situ Aircraft Daytime C_n^2 Measurements(Two Realization).	19
7.	Compilation of Land-based (Continental) Daytime C_n^2 Data Base	20
8.	Linear C_n^2 Models for White Sands Measurements with Variable ⁿ Turbulent Layer Height	22
9.	Exponential C_n^2 Models for White Sands Measurements.	23
10.	Dependence of Optical Properties of the Turbulent Layer at White Sands on Layer Thickness.	25
11.	Geometry corresponding to the definition of r_1	28
12.	Residual Wavefront Error Variance for "Ideal" Phase Compensation of an Extended Image.	31
13.	"Ideal" Residual Wavefront Error Variance.	33
14.	Log-normal Distribution of Solar Granule Scale Sizes from Analysis of SPNO Photographic Data.	41
15.	Residual Wavefront Error Variance for a Realistic Adaptive Optic System Phase Compensation of Extended Images.	42

<u>Figure No.</u>	<u>LIST OF FIGURES CONT'D</u>	<u>Page</u>
16.	Log-normal Correlation Scale Distribution Compared to Maui Data where mean = 9.63 cm, $\sigma = 2.23$ cm.	44
17.	LSI ³ Sensor.	47
18.	Detector Arrays as Pupil Dividers.	49
19.	LSI ³ Diffraction Code - simulated waveforms	50
19a.	SCS Algorithm Gate-angle Geometry.	50
19b.	Tilted Gate-angle Geometry	50
20.	MODS Full-Aperture Image Sharpener	61
21.	MODS Numerical Simulation Code	65
22.	Unaberrated image plane distribution for point source input.	72
23.	Image distribution with $.65\lambda$ defocus.	74
24.	Image distribution with $.58\lambda$ astigmatism and curvature of field.	74
25.	Image distribution with $.66\lambda$ astigmatism and curvature of field	75
26.	Image distribution with all three 2 nd order Zernike modes	75
27.	Image distribution with $.7\lambda$ coma in X direction . . .	76
28.	One Step Algorithm.	79
29.	One Step Algorithm.	80
30.	Two Step Algorithm.	83
31.	Two Step Algorithm.	84
32.	Input aberrated image of run shown in Figure 30	85
33.	Iteration #1.	85
34.	Iteration #2.	86

<u>Figure No.</u>	LIST OF FIGURES CONT'D	<u>Page</u>
35.	Iteration #3.	86
36.	Iteration #4.	87
37.	Iteration #20	87
38.	PPSI value for double source aligned with Y axis. . . .	88
39.	p-p Aberration for run for Figure 38.	89
40.	PPSI values for double star at an angle of 37 with Y axis.	90
41.	Corresponding p-p aberration values.. . . .	91
42.	Unaberrated input for run of Figure 38	92
43.	Starting aberrated image p-p aberration $\sim 6\lambda$	92
44.	Iteration #3	93
45.	Iteration #17	93
46.	Unaberrated input for run of Figure 40.	94
47.	Input aberrated image	94
48.	Final image, iteration #20.	95
49.	MODS Using SLM.	97

TABLE

I.	Cartesian Representation of Zernike Polynomials . . .	67
----	---	----

I. INTRODUCTION

1.1 HISTORY OF THE PROGRAM

This represents the final report of the work carried out by Adaptive Optics Associates, Inc. (AOA) under Contract No. F19628-82-C-0035 with AFGL/PHS. This project, and hence this report, consists of two very distinct parts. One is a detailed assessment of the limitations of traditional adaptive optic techniques when applied to imaging of extended features on the solar surface. The second describes and provides the preliminary results of a computer simulation of an alternative approach to the problem of imaging objects that are large compared to the isoplanatic patch size.

As originally proposed, this program was to have consisted of two phases, the first a feasibility study of a subaperture based, correlation tracking method of wavefront detection, the second a breadboard test of the system in field conditions at SPNO. Work on this program proceeded as scheduled and Phase I was successfully completed. The results of this analytic and numerical study of the application of adaptive optics to the problem of solar imaging showed that, under typical conditions, it was not possible to define subapertures that would see a wavefront that was approximately flat. These results are presented here in Section II. Unfortunately, this also showed that the proposed wavefront sensing scheme would not produce useful phase information except under exceptional atmospheric conditions. Therefore, the second phase of the proposed program was not carried out. In its stead, an attempt was made to uncover alternative approaches to the problem. After considerable thought, a possible full aperture image sharpening method was identified. This approach to image sharpening has been termed the Modal Dithering Sharpener or MODS. As will be described below, it utilizes an error signal derived from a full aperture image to drive a servo loop that corrects the pupil wavefront.

At the same time, the contract program was restructured. Two new phases were defined: a detailed analysis of the performance of the new imaging technique refinement of the algorithm, and a numerical simulation of the process to test its feasibility before attempting to breadboard a working system. This program has been carried out and the results are presented in the third and fourth sections of this report.

II. ADAPTIVE OPTIC LIMITATIONS FOR SOLAR IMAGING

2.1 INTRODUCTION

Real-time predetection image compensation of ground-based astronomical telescopes for near point-like images such as stars has been demonstrated⁽¹⁾, but adaptive optics has had very limited success when applied to extended features on the sun⁽²⁾. Even in stellar applications, the success of adaptive optics has been limited to second magnitude or brighter stars due in part to large optical path transmission losses⁽³⁾. The limited success of adaptive optics to sharpen the extended features of the sun was attributed⁽³⁾ to the small size of the isoplanatic patch. Nighttime near zenith measurements on double, second magnitude stars indicated a two to four arc-sec isoplanatic angle which limited the compensated image angle to less than one arc-sec⁽³⁾. More recent measurements⁽⁴⁾ of isoplanatic angle at White Sands and the surrounding area indicate that it has a diurnal variation with average daytime zenith values being close to one arc-sec or even smaller when the jet stream was overhead. These measurements indicate that the usefulness of adaptive optics for solar imaging is even more limited than previously thought.

The community of solar astronomers has expressed considerable

(1) J.W. Hardy, J.E. Lefebvre and C.L. Koliopoulos, "Real-Time Atmospheric Compensation, "JOSA 67, 3, March 1977.

(2) J.W. Hardy, "Solar Isoplanatic Path Measurements," Proc. Sacramento Peak National Observatory Conf., Sunspot, NM, October 1980.

(3) J.W. Hardy, "Solar Imaging Experiment," ITEK Final Report, Contract AFGL-TR-80-0338, September 1980, ADA 102283.

(4) D. Walters, "Diurnal Variation of Isoplanatic Angle," Optical Society of America Annual Meeting, October 1983, New Orleans, Louisiana.

interest in and indeed has forecast the advent of the usefulness of adaptive optics on large, ground-based telescopes for solar imaging of fine scale granularity with high resolution⁽⁵⁾. If feasible, the development of a solar imaging capability could make ground-based telescopes an attractive, cost-effective alternative to high resolution space-based telescopes such as the Solar Optical Telescope (SOT). The advantages of increased data flow, target track time and flexibility if available with compensated, ground-based telescopes would be an obvious boon to the field of solar astronomy. Unfortunately our results indicate that the feasibility of solar adaptive optics (SAO) is severely limited by strong daytime atmospheric turbulence.

Other authors have also expressed some doubt concerning the feasibility of solar imaging. Smithson and Tarbell⁽⁶⁾ (Lockheed) express the opinion that "fully active mirror systems are presently costly, unreliable and of marginal performance for daytime seeing," whereas they claim that "image motion is easy to track with simple tilt mirror systems" using any of "several existing wavefront sensors." They report routine tracking with a 400 Hz bandwidth system of sunspots or pores that are larger than three arc seconds in diameter, and tracking of dark lanes in between granules in very good seeing⁽⁷⁾. They report an uncompensated image jitter of two to five arc-sec in normal daytime seeing (i.e., $r_0 = 2$ to 5 cm at $\lambda = 0.5 \text{ } \mu\text{m}$).

⁽⁵⁾ "Solar Instrumentation: What's Next?" Sacramento Peak National Observatory (SPNO) Conference Proceedings, edited by R.B. Dunn, held at Sunspot, NM, October 1980, published March 1981, for the example the paper by L.E. Cram, SPNO pg. 397.

⁽⁶⁾ R.C. Smithson and T.D. Tarbell, "Sensor Technology for Adaptive Mirror Systems Applied to Solar Astronomy," SPNO Conference Proceedings.

⁽⁷⁾ T.D. Tarbell and R. C. Smithson, "A Simple Image Motion Compensation System for Solar Observations," SPNO Conference Proceedings, pg. 491, March 1981.

Hardy⁽²⁾ (ITEK) also obtained image motion stabilization even in "bad turbulence" using the Real-Time Atmospheric Compensation (RTAC) system at SPNO, but "in all but a few cases, no corresponding improvement in image quality was seen over the compensated patch" because the "isoplanatic patch was much smaller than the wavefront sensor field of view." Occasionally with good daytime seeing, the RTAC could improve telescope (30 cm aperture) performance from three arc-sec to about one arc-sec, whereas under the same conditions simple image motion compensation alone produced only marginal image improvement.

In this report we first examine the potential of adaptive optics by considering the performance of an "ideal minimum bound variance" Hartmann wavefront sensor coupled with a "perfect" zero-fitting error deformable mirror using lossless optical transmission and upper bound quantum efficiencies. Next the same analysis is presented for the AOA proprietary LSI³ wavefront sensor. Finally, we present simulation results that provide a scanning-mode for the LSI³ sensor. But first we present a simple, heuristic model of the properties of atmospheric turbulence in order to acquaint the reader with the basic principles of adaptive optics.

2.2 THE BASIC PRINCIPLES OF ADAPTIVE OPTICS

Real-time diffraction-limited resolution imaging of targets may be obtained from the use of adaptive-optic systems that compensate for atmospheric turbulence. The uncompensated resolution of objects through atmospheric turbulence is limited to λ/r_0 where r_0 coherence diameter⁽⁸⁾ of the laser radiation which depends both on the intensity and extent of the atmospheric turbulence as well as λ , the laser wavelength. Average values of r_0 range from 2 cm in the daytime to 10 cm at night for zenith observations, and are smaller away from zenith. The turbulent atmosphere may be modeled

⁽⁸⁾ David Fried, JOSA 55, 1427, 1966.

as consisting of closely packed tubes of diameter r_0 within which the tilt of the wavefront reflected from the target is well defined, but where the wavefront tilt (i.e., angle-of-arrival) varies slightly from tube to tube. Overall tilt variations of $\pm 1/2 (\lambda/r_0)$ occur. Adaptive optics operates by separately measuring the tilt in each tube in subapertures of the wavefront sensor that are approximately r_0 in diameter. The conjugate of each subaperture tilt, amounting to a variable tilt across the full aperture, is then reconstructed on a deformable mirror. In principle, reflection of the incoming irradiance from this mirror then sharpens the target image up to the diffraction limit of the full aperture. In practice, the diffraction limit is never quite reached due to system errors such as low sensor bandwidth and signal-to-noise as well as atmospheric errors such as wavefront incoherence, anisoplanaticity and irradiance scintillation, and inaccurate reconstruction of the conjugate wavefront at the deformable mirror, the so-called "fitting errors." All of these errors may be represented by variances, σ^2 , that when geometrically summed and expressed in waves, directly indicate the degradation from diffraction-limited performance by means of the Strehl ratio, $S = \exp(-\sum \sigma^2)$, where the summation is over the various types of errors. The resulting telescope resolution is then given by $(\lambda/D)\exp(+\sum \sigma^2)$.

Adaptive optics is effective as long as these errors are sufficiently small to maintain a Strehl ratio close to one. Under conditions of sufficient turbulent intensity and extent, anisoplanatic errors due to extended images that exceed the size of the isoplanatic patch will prevent the effective use of adaptive optics. The isoplanatic patch is usually expressed as the angle that is given by r_0 divided by the (slanted path) scale height of the turbulent atmosphere, as shown in Figure 1. Although the precise definition of isoplanatic patch may differ from this simple model, and several definitions are extant in the literature, the physical behavior predicted by this model is correct. Anisoplanatism may be avoided by gating the field-of-view (FOV) of the wavefront sensor down to the size of the isoplanatic patch. But even then a fundamental limit is obtained when the resolution of each wavefront sensor subaperture $\approx \lambda/r_0$ exceeds the isoplanatic angle r_0/ℓ where ℓ is the distance to the turbulent scale height. Thus adaptive optics fails on extended objects when $r_0 < \sqrt{\lambda \ell}$. For vertical propagation through the SPNO atmosphere, $\ell \approx 5$ Km and $\sqrt{\lambda \ell} = (0.5 \mu\text{m} \times 5 \text{ Km})^{1/2} = 5 \text{ cm}$. Seeing conditions are only better than this limit for airborne or high mountain-based sensor platforms at night, or for horizontal propagation to targets closer than 10 Km for low altitude applications of adaptive-optics. Note that these minimum seeing conditions correspond to an isoplanatic angle $r_0/\ell = 2 \text{ arc-sec}$.

This anisoplanatic limit does not apply to point-like objects such as stellar objects or high contrast target glints whose extent is smaller than the isoplanatic patch. Similarly, for very intense turbulence and very long optical paths in the atmosphere, errors associated with irradiance scintillations will not render adaptive optics ineffective because the so-called "saturated turbulence"

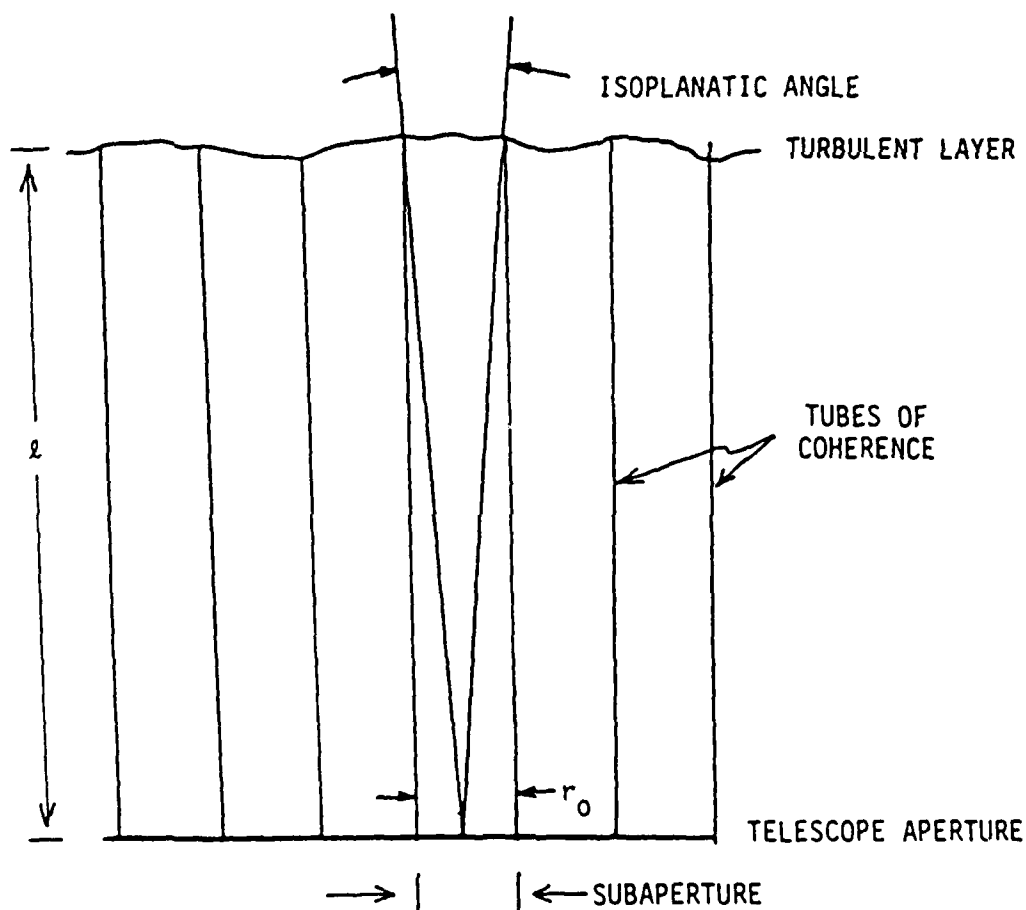


Fig. 1. Model of the coherence properties of the turbulent atmosphere for vertical propagation to or reception from a distant target.

phenomenon limits the error variance due to scintillations to $\sigma^2 \leq 0.25$.⁽⁹⁾ However, adaptive optics requires a sufficient SNR to operate successfully. As a result, adaptive optic sensors do not have sufficient sensitivity in each subaperture to perform real-time phase compensation on the faint stellar objects that are of greatest interest to astronomers. The problem is that in order to do real-time phase compensation, the system integration time must be somewhat less than the scale time of the variable turbulent atmosphere, which is 10 msec or less. Post-detection techniques in current use benefit from very long integration times.

2.3 CHARACTERIZATION OF THE TURBULENT ATMOSPHERE

At any point on the ground the optical properties of the turbulent atmospheric layer may be determined from the direction of the optical path specified only by the zenith angle θ_z and the altitude profile of the turbulent structure function $C_n^2(z)$. From the C_n^2 profile and θ_z , we derive expressions for the coherence diameter r_0 ⁽¹⁰⁾ and the isoplanatic angle θ_p ⁽¹⁰⁾, two parameters that completely determine the optical properties of the turbulent layer at points on the ground. The literature uses two expressions for r_0 , based on plane or spherical optics. We use the plane wave r_0 because it is the reported result of seeing monitor

$$r_0 = \frac{0.423 k^2}{\cos \theta_z} \int dz \cdot C_N^2(z)^{-3/5}, \quad \text{plane wave} \quad (1)$$

$$\theta_p = \frac{1.45 k^2}{\cos^{8/3} \theta_z} \int dz \cdot z^{5/3} C_N^2(z)^{-3/5}, \quad \text{spherical wave} \quad (2)$$

$$k = 2\pi/\lambda, \quad \lambda = \text{wavelength in the visible.}$$

⁽⁹⁾ IR Handbook, pp. 6-20, 1978.

⁽¹⁰⁾ Fried, JOSA 55, 1427 (1966).

measurements⁽¹¹⁾. The spherical wave form of the theory is used to determine the half-angle of the cone defined by the isoplanatic patch.

Because of the $z^{5/3}$ altitude moment-error dependence the spherical wave theory (hence the isoplanatic angle) is sensitive to the high-altitude portion of the C_n^2 profile, whereas the plane wave theory (and hence the coherence diameter) is sensitive to the layer of intense turbulence near the ground.⁽¹²⁾

The geometrical simplicity of this model derives from C_n^2 being a constant in x and y . In fact, above 1 Km in the turbulent layer, the horizontal C_n^2 profile depends on the global wind patterns over distances that are large compared to the height of the layer. Terrain effects on the C_n^2 profile such as variations in ground cover and hills occur on a distance scale that are usually small but can be comparable to the atmospheric layer height. But these effects are normally confined to the first thousand meters of atmosphere. Since the coherence diameter has a strong dependence on the intense ground layer of turbulence generated by these variations, we would expect r_0 to have a relatively higher frequency of variation compared to the isoplanatic angle dependence on global wind patterns.

Due to the dependence of turbulence strength on wind velocity, a meteorologically determined correlation⁽¹³⁾, the jet stream has a dominant effect on the high-altitude C_n^2 profile. But stratification of the C_n^2 profile into sub-layers or plateaus can also be expected on the basis of differing air masses in stratified wind patterns, evident in wind velocity altitude

(11) Shapiro, JOSA 65, 65 (1975).

(12) Miller and Zieske, "Turbulent Environment Characterization", RADC- TR-79-131, July, 1979. AD 072379

(13) Clifford, NOSA, Univ. of Colorado.

profiles⁽¹⁴⁾.

The widely available measurements⁽⁸⁾ of C_n^2 profile using a scintillometer at the Air Force Maui Observatory indicate a ground layer of intense turbulence at low altitudes and plateaus of high altitude turbulence as shown in Figure 2. Other measurements of C_n^2 profile evidence both the jet stream effect and plateau-like behavior⁽¹⁵⁾ ⁽¹⁶⁾, as shown on Figures 3 and 4. What is really shown on these figures is the standard phenomenological and mathematical models which have emerged from the measurements. Several of them attempt to separate the C_n dependence into a polynomial ground layer within one kilometer plus an exponential layer that dominates from one Km to the 10 to 20 Km top of the turbulent layer, plus a quadratic layer of more intense turbulence due to the jet stream. In an exponential atmosphere the isoplanatic angle θ_p is proportional to r_0 , dependent only on the scale height of the exponential atmosphere h_0 or the height of the uniform layer of turbulence h . Insofar as the high-altitude C_n^2 profile

Exponential or Uniform Turbulent Atmosphere

$$\theta_p = \frac{r_H}{1.16h \cos \theta} = \frac{r_H}{1.16h_0 \cos \theta} \quad (3)$$

(14) Valley, Geophysics Handbook, pg. 671

(15) Hufnagel and Stanley, JOSA 54, 52 (1964)

(16) Barletti, et al., JOSA 66, pg. 1380 (1976)

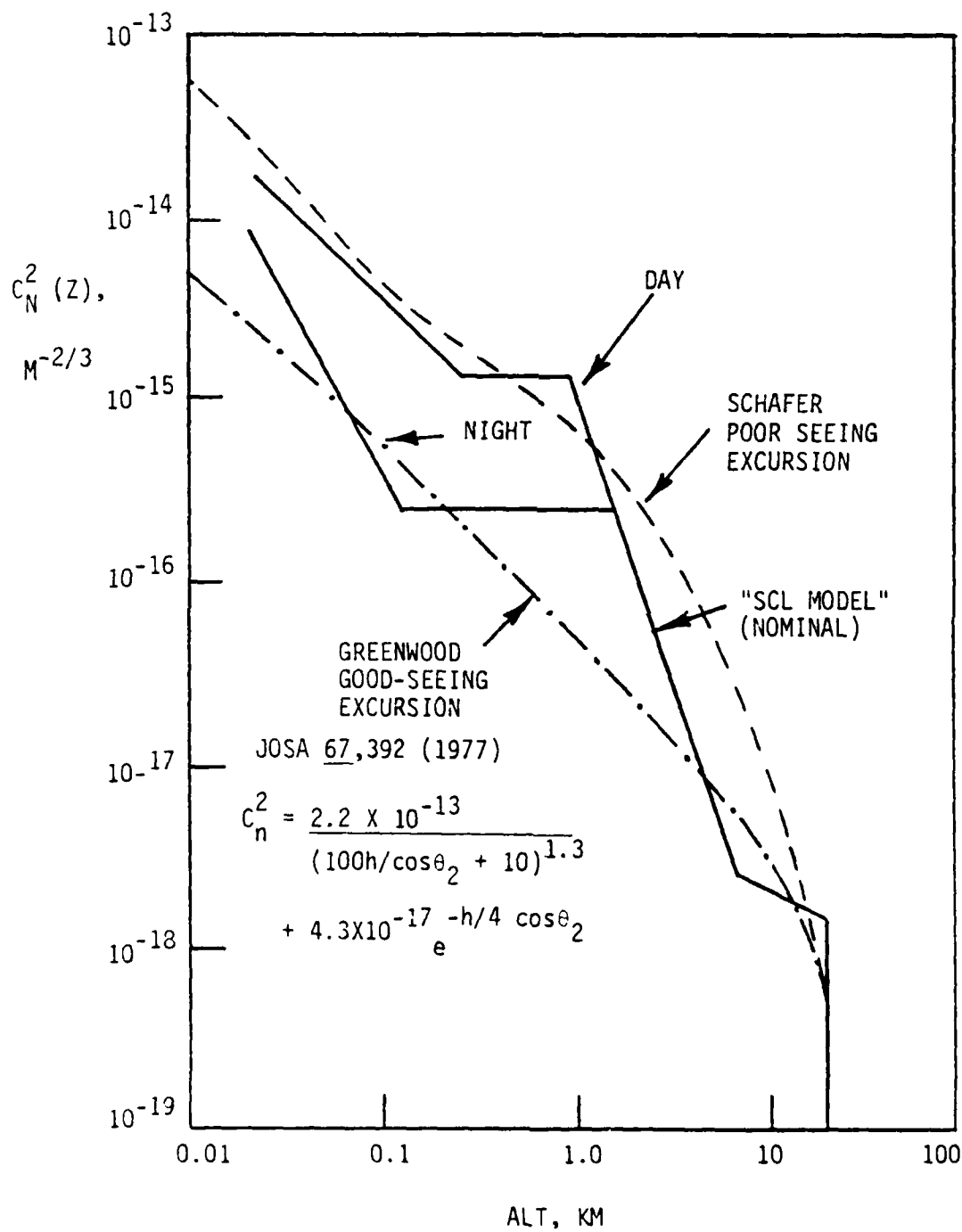


Figure 2. Island-mountain based Maui Observatory Scintillometer C_n^2 Measurements and Modeling.

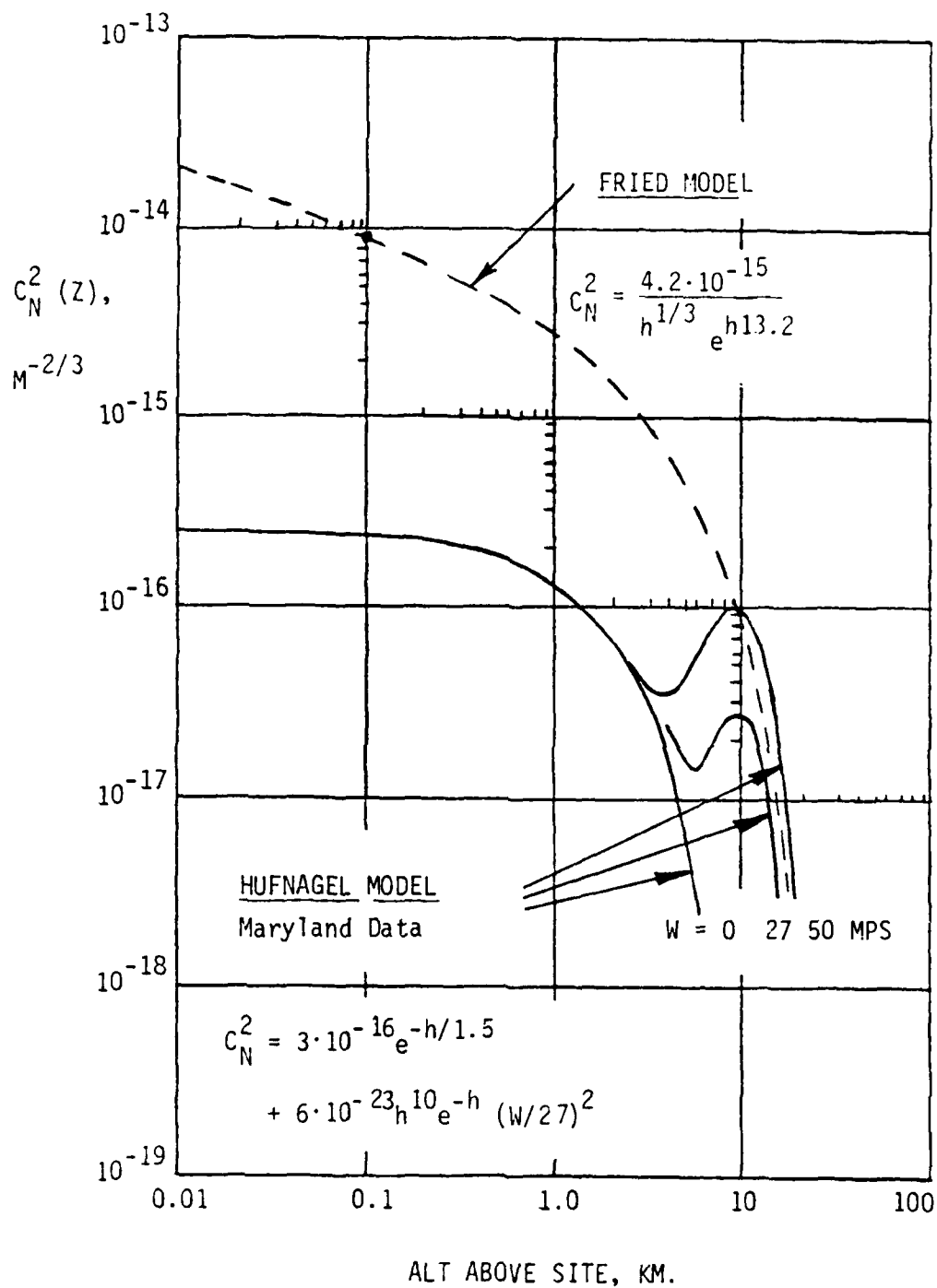


Figure 3. Land based (continental) C_N^2 models.

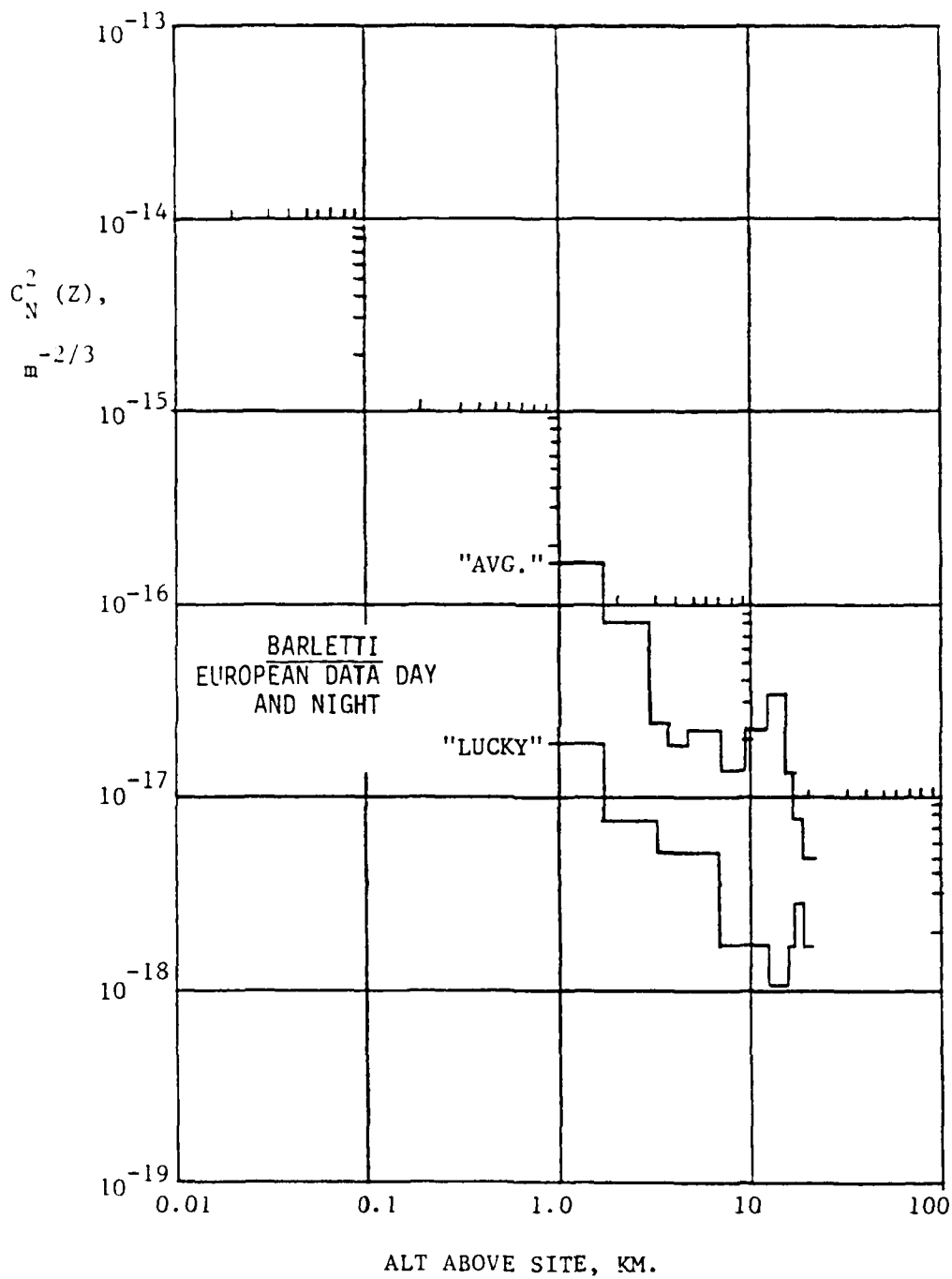


Figure 4. In-situ balloon C_N^2 measurements over Continental Europe.

may be characterized as dominated by a single flat or exponential plateau, we may immediately obtain an estimate of the isoplanatic angle. However, we must be careful to use only contribution to r_0 from the layer being modeled. In the Greenwood and Schafer models of Figure 2, the contributions to r_0 come equally from the ground layer and the exponential layer. Referring to these as r_L and r_H , respectively, Eq. (1) becomes

$$\frac{1}{r_0^{5/3}} = \frac{1}{r_L^{5/3}} + \frac{1}{r_H^{5/3}} \quad (4)$$

For both the Greenwood and Schafer models $r_H = 0.25\text{m}$, the factor of two in C_n^2 offsets the factor of two in scale height, but contrary to intuition the isoplanatic angle for the Greenwood model (1 arc sec) is of one-half the isoplanatic angle for the more intense Schafer model (2 arc-sec), indicating the importance of the height of the turbulence.

We find evidence of a high altitude plateau or layer from 8 Km to 20 Km in both the island based data of Miller-Zieske and Hanson, and the European continent based data of Barletti. It appears that the European "lucky observer" data correlates with the average Maui data at high altitudes. The Hufnagel continental model with 27 MPS jet stream at 10 Km correlates the average European data well. The dependence on the jetstream effect is explicit in the Hufnagel model. It also correlates the Maui high-altitude data very well with a weak jet stream effect, $w \approx 7$ MPS.

It is evident from the available widely used models that even the average optical properties of the turbulent atmosphere are sensitive to ground location, particularly with respect to the jet stream. Since C_n^2 profile measurements are not available for the SPNO observatory, we must rely on nearby measurements at the White

Sands proving grounds. Measurements of r_0 ⁽¹⁷⁾ at a White Sands mountain site indicated a strong diurnal variation, but less strong day-to-day seasonal variations. More recent measurements of the isoplanatic angle published at meetings⁽¹⁸⁾ but not available in the literature also indicate a diurnal variation as well as a jet stream dependence. In the absence of a jet stream the average isoplanatic angle is one arc-sec in the daytime and two arc-sec at night, corresponding to uniform values of $r_0 = 4$ cm in the daytime and average values of $r_0 = 8$ cm at night. Apparently the turbulent layer height is fairly constant at White Sands, at a scale height of $h_0 = 5$ Km, assuming equal ground layer and high altitude contribution to r_0 .

Single realizations of the C_n profile along ascending and descending spiral aircraft paths have been measured over White Sands⁽¹⁹⁾ up to 7 to 8 Km. Four resulting sets of measurements are shown on Figures 5, 6 and 7.

The first, an ascending spiral on 31 March 1978 close to noontime reveals a high degree of fluctuation about a mean that falls off inversely proportional to altitude. There is some evidence of stratification with an intense layer of turbulence at 2 Km and a high-altitude plateau from 3 Km to 8 Km. The two realizations of the C_n^2 profile were taken near noontime on 20 June 78 in an ascending and descending spiral. Although the ground-layer of intense turbulence (up to 100m) varied an order-of-magnitude in the two realizations, the high altitude profiles were similar and indicate plateau-like behavior from 100m to 5 Km. The last flight

⁽¹⁷⁾Walters, Favun and Jones, JOSA 69, 828(1979).

⁽¹⁸⁾Walters, OSA Annual Meeting, New Orleans (1983).

⁽¹⁹⁾ "Atmospheric Conditions at the High Energy Laser System Test Facility (HELSTF), White Sands Missile Range," Atmospheric Sciences Laboratory Interim Report, 10 June 1979 and 8 August 1979, U.S. Army Electronics Research and Development Command, WSMR, NM 88002.

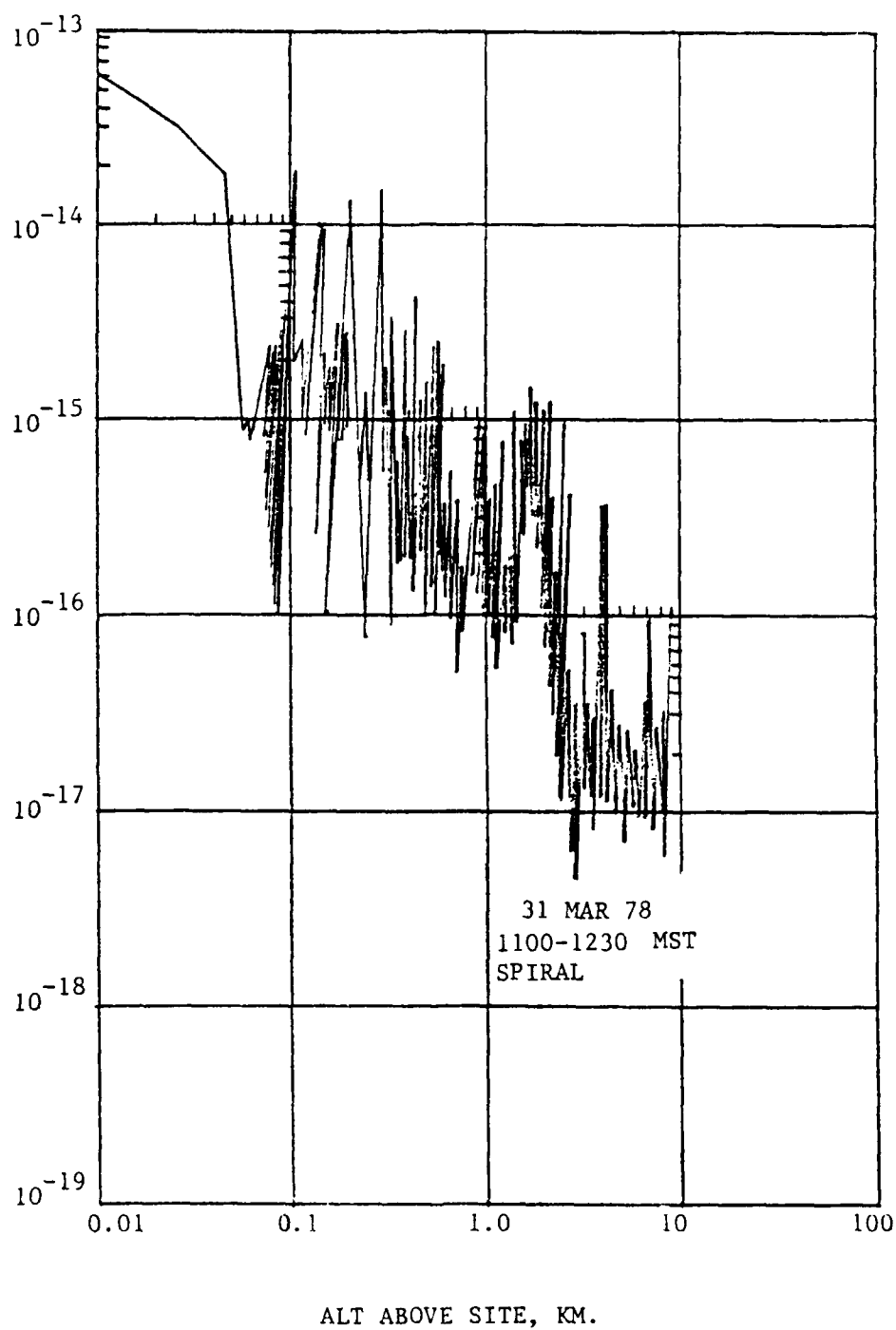


Figure 5. White Sands in-situ aircraft daytime C_N^2 measurements (single realization).

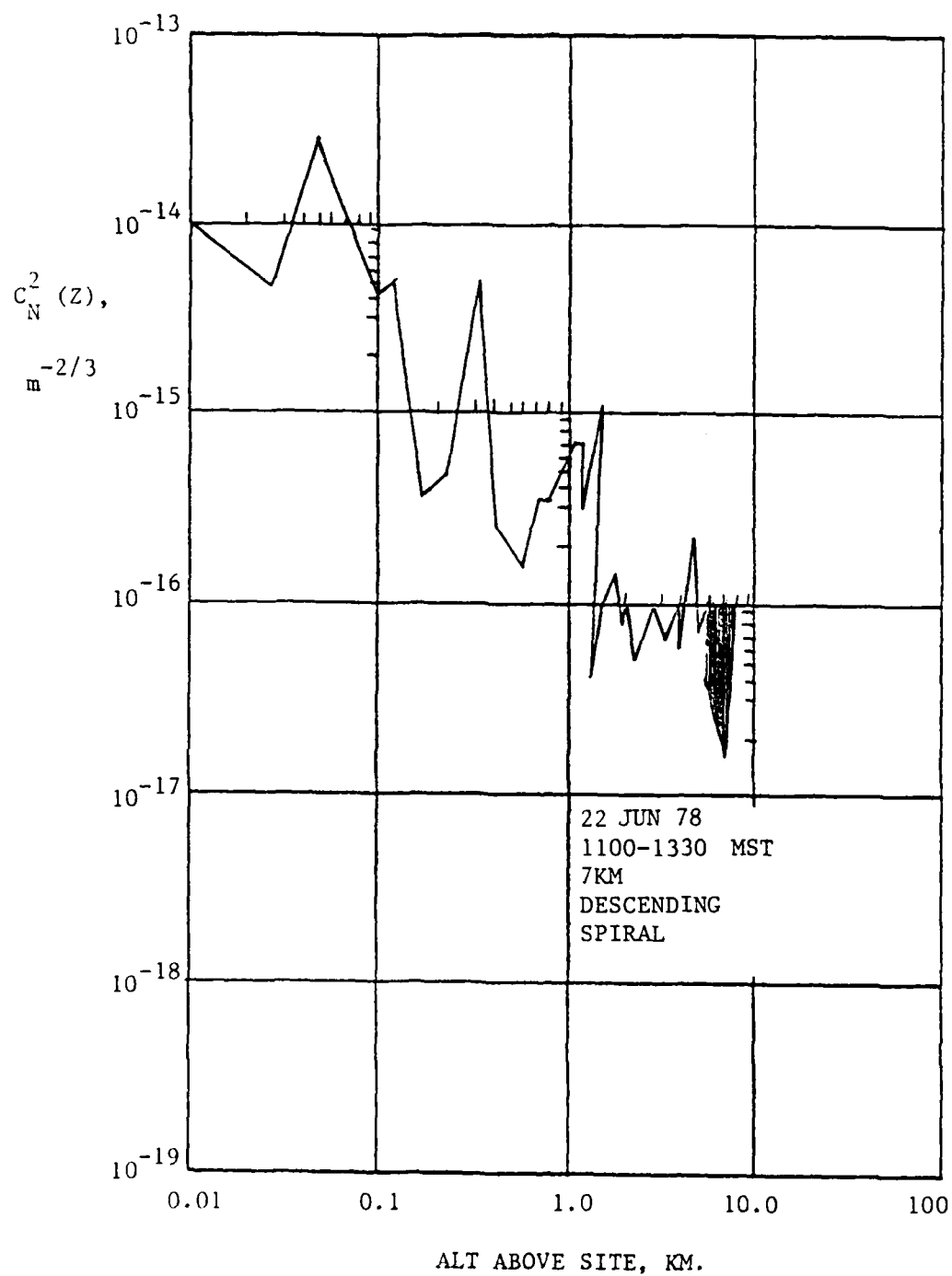


Figure 6a. White Sands in-situ aircraft daytime C_N^2 measurements (single realization).

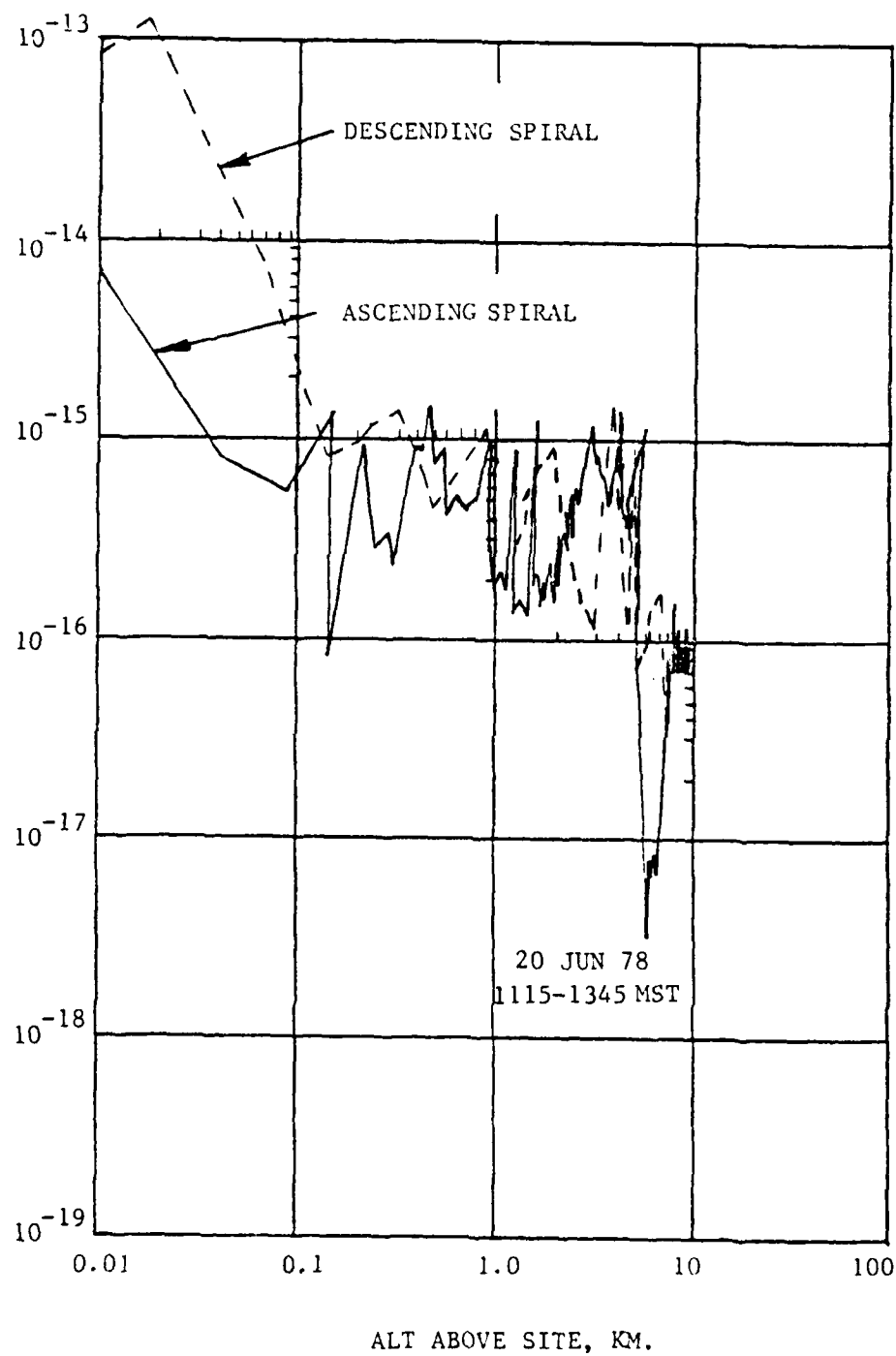


Figure 6b. White Sands in-situ aircraft daytime C_N^2 measurements (two realizations).

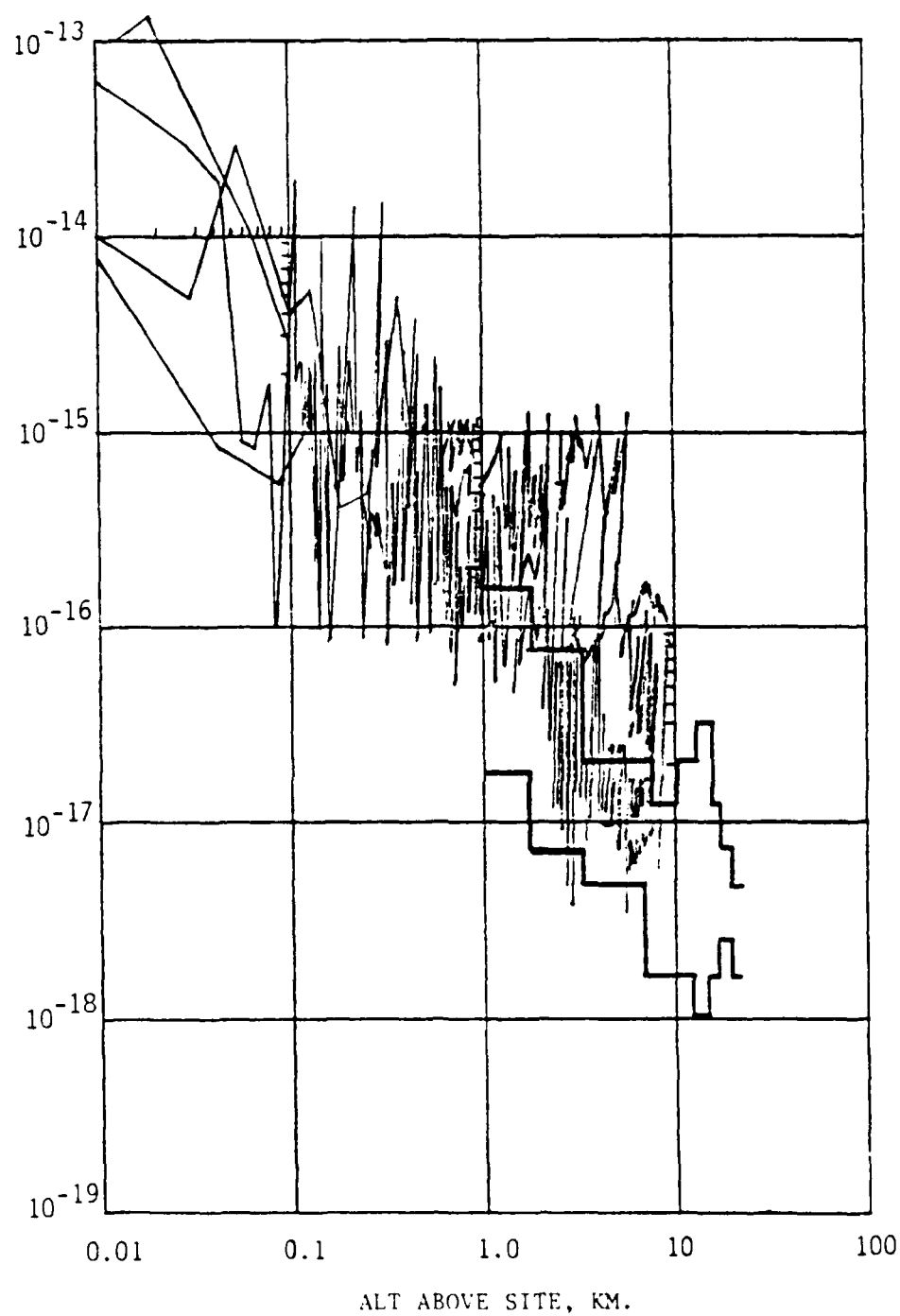


Figure 7. Compilation of land-based (Continental) daytime C_N^2 data base.

on 22 June 78, a descending spiral, indicates a 1 Km ground layer with inverse linear C_n^2 decay, and a $10^{-16} \text{ m}^{-2/3}$ plateau from 2 Km to 7 Km.

In order to obtain a C_n^2 model appropriate for White Sands, and presumably SPNO as well, we have overlaid all of the White Sands data and the European Barletti data on Figure 7. The Barletti data is added in order to infer C_n^2 behavior above the aircraft 8 Km ceiling. Although the single realizations indicate some plateau-like behavior, the average over the four realizations is best fit by a $1/h$ decay throughout the entire turbulent layer, as shown on Figure 8. The Hufnagel model of Figure 3 is much less representative of the White Sands data even though it models the Barletti data quite well. The Schafer model on Figure 2 would also provide a good fit to the White Sands data, although the "exponential atmosphere" models shown on Figure 9 with a 4 Km scale height and an easily distinguished ground layer does not fit the data so well. The Schafer model is a better fit because the inverse linear ground-layer component dominates almost the entire C_n^2 profile. Considering the high degree of fluctuation of C_n^2 about the mean evident in the measurements, it seems best to model the entire layer linearly.

Unfortunately, like the Kalmogorov spectrum, the inverse linear C_n^2 profile is not integrable unless low altitude h_L and high altitude h_H cutoffs are used.

The problem then is to ascertain appropriate values for h_L and h_H , much like one must independently estimate the inner and outer turbulent scale sizes in order to find integrable properties of the Kalmogorov spectrum, i.e.,

$$C_n^2 = \begin{cases} C_n^2(1) / h_L, & h < h_L \\ C_n^2(1) / h, & h_L < h < h_H \\ 0, & h > h_H \end{cases} \quad (5)$$

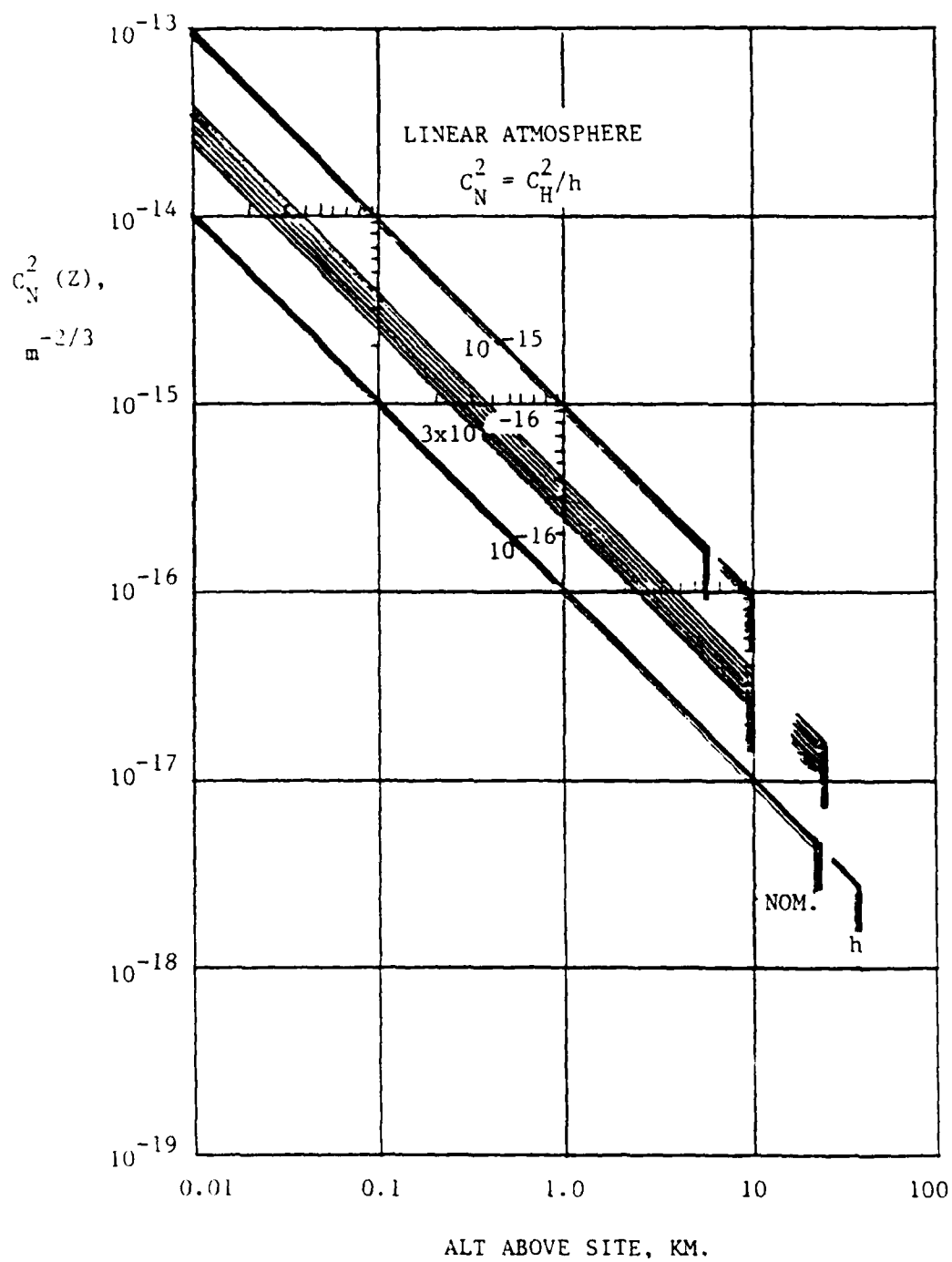


Figure 8. Linear C_N^2 models for White Sands measurements with variable turbulent layer height.

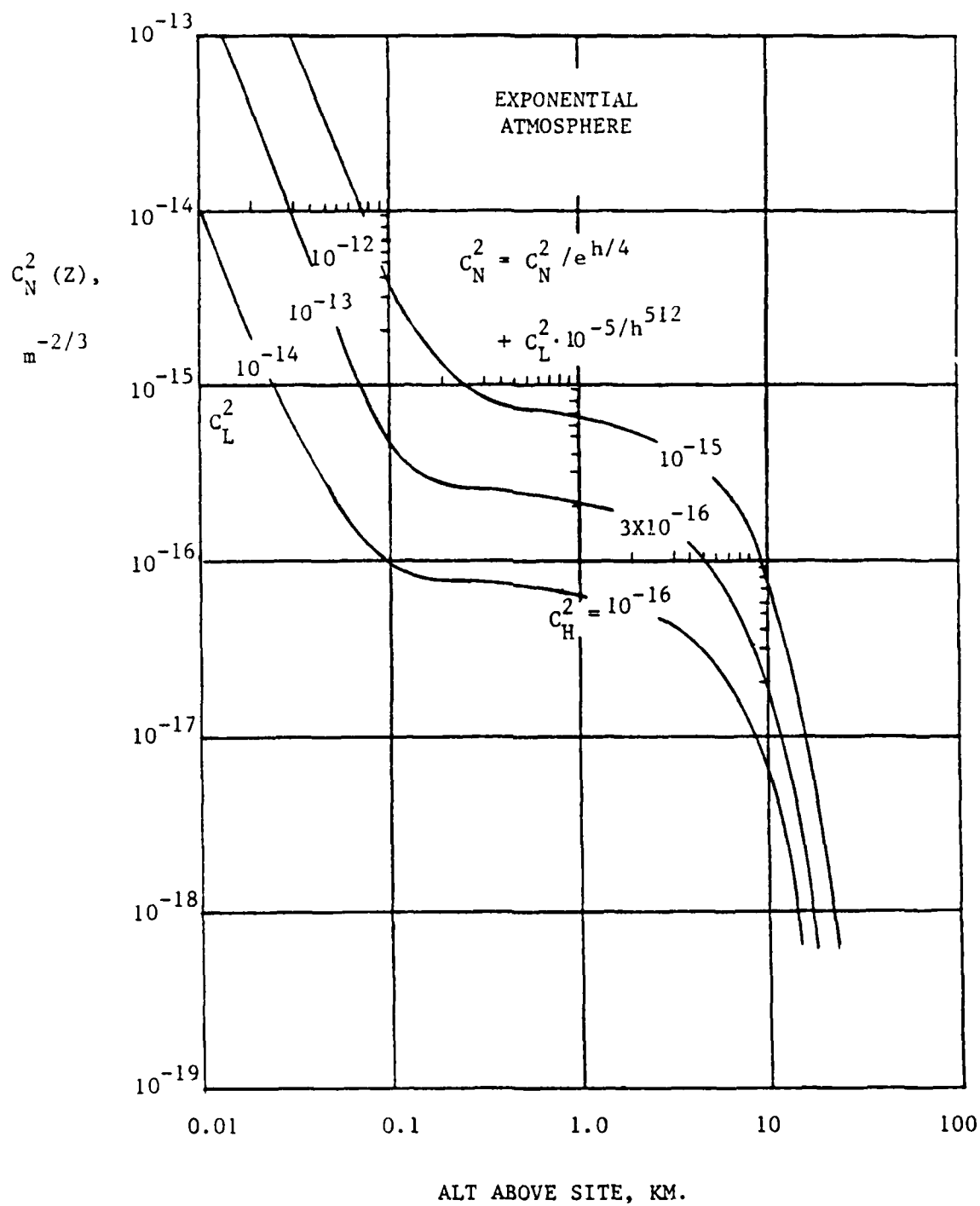


Figure 9. Exponential C_N^2 models for White Sands measurements.

where h is in Km.

We shall assume that the telescope aperture is at a height $h_L = 10\text{m}$ above ground, corresponding to the lowest available C_n^2 measurements. We then obtain the integrable properties for $\lambda = 0.5 \text{ } \mu\text{m}$:

$$r_o = \frac{10\text{cm}}{(C_n^2(1)/10^{-16})^{3/5}} \cdot \frac{1}{\left(1 + \frac{1}{7} \ln \frac{h_H}{10}\right)^{3/5}} \quad (6)$$

$$\theta_p = \frac{r_o \cos \theta}{h} \left(\frac{5}{\ln \frac{h_H}{h_L}} \right)^{3/5} \quad (7)$$

Note that except for a weak logarithmic dependence, this θ_p vs r_o model is equivalent to a uniform or exponential model.

The linear curve-fit of the White Sands data on Figure 9 suggests an average value of $C_n^2(1) = 3 \times 10^{-16}$ with fluctuations from 10^{-16} to 10^{-15} . If we arbitrarily assume a 10 Km turbulent layer thickness, then the average value of r_o is 5 cm which compares well with Walters' 4 cm daytime r_o measurements at White Sands. As shown in Figure 10, r_o is essentially independent of the height of the turbulent layer from 10 Km to 20 Km (20% drop). The isoplanatic angle, as shown on Figure 10, is very sensitive to the thickness of the turbulent layer. In fact, the isoplanatic angles are largely below one arc-sec. For example, the dashed lines indicate the isoplanatic angle corresponding to a $r_o = 4 \text{ cm}$ as measured by Walters. In order to have an isoplanatic angle as large as one arc-sec, the turbulent layer cannot be larger than a 7 Km thickness. Even if we assume SPNO daytime values of $r_o = 5 \text{ cm}$ (similar to the Maui data on Figure 2), a 10 Km turbulent layer thickness results in only a one arc-sec isoplanatic angle at $\lambda = 0.5 \text{ } \mu\text{m}$. Note that both r_o and θ_p scale as $\lambda^{+6/5}$ power so that two arc-sec isoplanatic

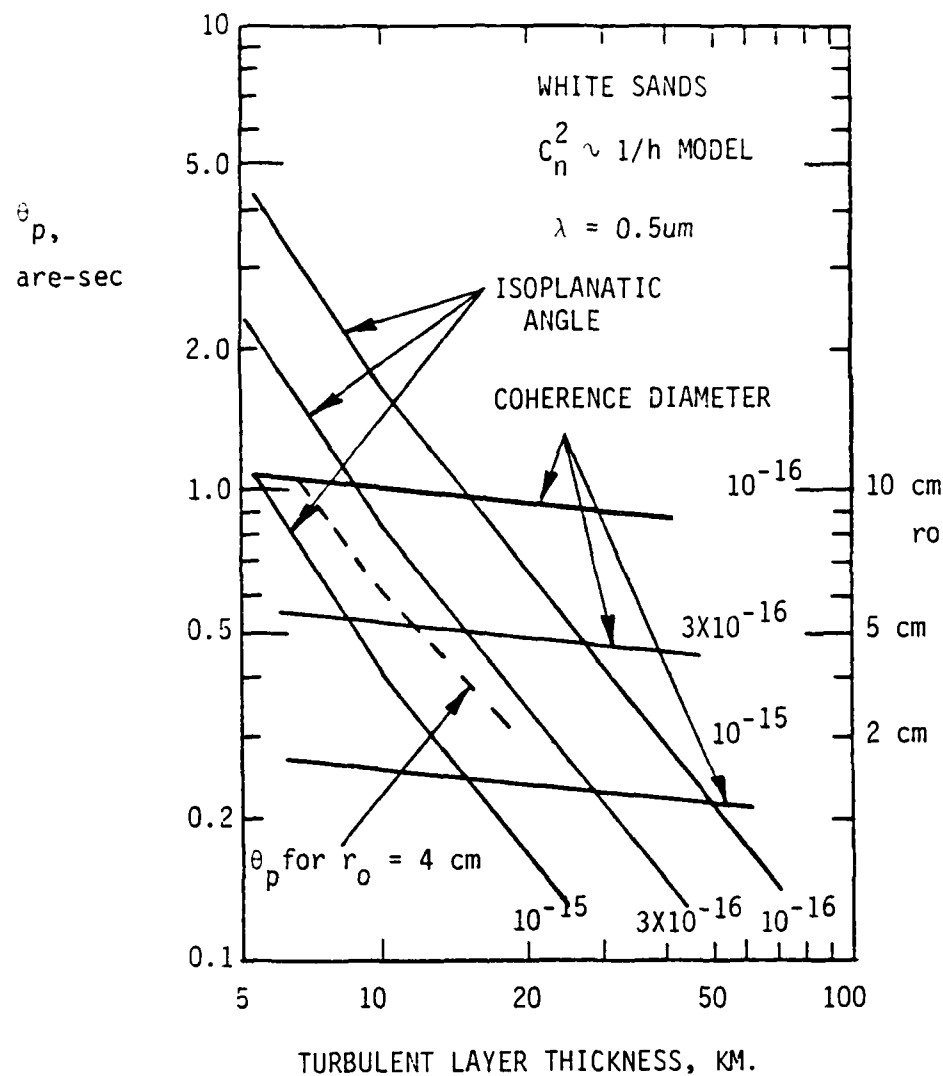


Figure 10. Dependence of optical properties of the turbulent layer at White Sands on layer thickness.

angles result in the long wavelength portion of the visible spectrum.

2.4 WAVEFRONT ERROR ANALYSIS OF AN IDEAL ADAPTIVE OPTIC SYSTEM

A precise estimation of minimum seeing conditions for extended images may be based on standard, simple algebraic expressions for the error variance σ^2 of the wavefront incident on the sensor due to the residual turbulence-induced errors given phase compensation of the incident light. The dominant sources of atmospheric wavefront errors are (a) the spatial incoherence error variance σ_R^2 , (b) the "isoplanatic patch error" σ_p^2 , and (c) the scintillation error variance σ_S^2 . Spatial incoherence errors occur when a subaperture of diameter d samples phase over an extent (in the image plane) greater than the coherence length r_0 of the atmospheric turbulence; isoplanatic patch errors occur when the resolution angle of the subaperture $\theta_R = \lambda/d$ is greater than or comparable to the isoplanatic angle θ_p ; and scintillation errors are significant in heavy turbulence when atmospheric propagation produces amplitude fluctuations in the incident light. The relationships for these errors are:

$$\sigma_R^2 = 0.13 (d/r_0)^{5/3} \quad (8)$$

$$\sigma_p^2 = (\Delta\theta/\theta_p)^{5/3} \quad (9)$$

$$\sigma_S^2 = \frac{0.56 k^{7/6}}{\cos^{11/6} \theta} \int_0^\infty C_n^2(Z) Z^{5/6} dZ \quad (10)$$

Hence we use Fried's definition of r_0 ⁽⁶⁾ and Shapiro's definition of θ_p ⁽⁷⁾, along with the standard relationship for

σ_S^2 (20).

The above equations specify the inherent atmospheric errors. They may be derived rigorously on the basis of two-source wave structure function. In addition to these errors we need to specify the hardware system error variance, namely the sensor (SNR) noise variance σ_N^2 , and the deformable mirror reconstruction or "fitting" error variance σ_F^2 . We shall assume for the case of the "ideal" system that reconstruction of the conjugate phase on the deformable mirror is perfect, that is, $\sigma_F^2 = 0$. For the noise variance of an ideal system where detector noise is negligible we use the minimum bound variance (MBV) for photon-limited noise of a square subaperture

$$\sigma_N^2 = 0.25 (\lambda/d)^2 / \text{SNR}^2 \quad (11)$$

The detector noise variance is most important where the incident signal is weak, as in stellar astronomy.

2.5 EXTENDED IMAGES

Equation (10) may be expressed in a more convenient form by defining a new parameter

$$r_1 = \frac{\lambda}{r_0} \frac{h}{\cos \theta} \quad (12)$$

which is the diameter resolved by an uncompensated telescope at the height h of a uniform atmosphere or the scale height of an

(20) The Infrared Handbook, ed. W.L. Wolfe and G.J. Zissis, Officer of Naval Research, Washington, D.C., 1978, pg. 6-40; also R.R. James, et al., "Strategic Laser Communications Evaluation Algorithm," Naval Ocean Systems Center, CM06 Ser. 813/334, April 1981.

exponential C_n^2 profile. It is also the diameter of a subaperture that just resolves the isoplanatic patch as shown in Figure 11.

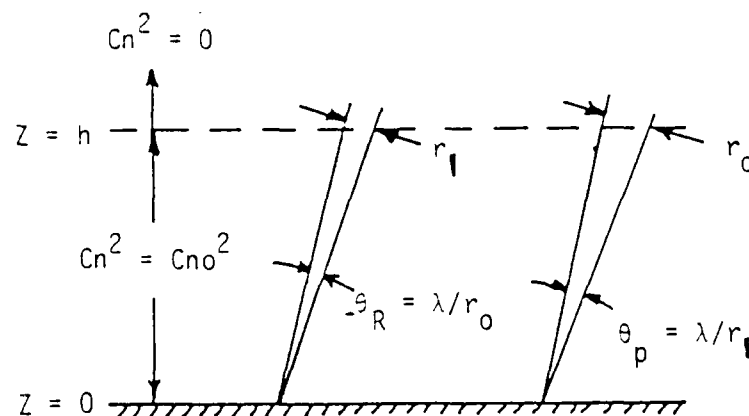


Figure 11. Geometry corresponding to the definition of r_1 . From Eq. (13) the scintillation error variance is

$$\sigma_S^2 = 0.1 \left(r_1 / r_0 \right)^{5/6} = 0.1 \left(\lambda h / r_0^2 \cos \theta \right)^{5/6} \quad (13)$$

Equation (9) for the anisoplanatic error variance only determines the wavefront errors associated with the correlation of two directions in space separated by an angle $\Delta\theta$. This expression is appropriate for essentially point sources in these two directions. For an extended source such as the sun, phase information is received over a solid angle corresponding to the resolution of the system, i.e.,

$$\sigma_p^2 = \frac{1}{\pi \theta_R^2} \int_0^{\theta_R} \left(\frac{\Delta \theta}{\theta_p} \right)^{5/3} 2\pi \Delta \theta d \quad (14)$$

or

$$\sigma_p^2 = 0.17 \left(\theta_R / \theta_p \right)^{5/3} \quad (15)$$

It would be more precise to integrate over the system point spread function (PSF) but at the level of approximation of the present analysis, the above simple analysis suffices.

The next step in the analysis is critical to the determination of the effective system resolution θ_R . We initially choose this to be the resolution of an ideal sensor, e.g.,

$$\theta_R = \lambda / d \quad (1\sigma, \quad 1 \text{ axis definition}) \quad (16)$$

where d is the size of a subaperture. In Section 3.0 we use a system resolution corresponding to the field-of-view (FOV) of the LSI³ sensor. With the present choice for θ_R , and $\theta_p = r_o / h \cos \theta$

Equation (8) becomes

$$\sigma_p^2 = \left(0.17 \frac{\lambda h}{r_o d \cos \theta} \right)^{5/3} \quad (17)$$

As indicated in section 2.3, the White Sands $1/h$ model has a slightly smaller isoplanatic angle.

$$\theta_p = (r_o / h \cos \theta) \cdot (5 / \ln h / 10)^{3/5}$$

where h is the height of the layer ~ 10 Km. Neglecting the weak log dependence, the error variance for $h = 10$ Km is

$$\sigma_p^2 = 0.24 \left(\frac{\lambda h}{r_o d \cos \theta} \right)^{5/3} \quad (18)$$

$$\sigma_p^2 \doteq 0.17 (r_1/d)^{5/3} = 0.17 (r_1/r_o)^{5/3} (d/r_o)^{-5/3} \quad (19)$$

$$\sigma_R^2 \doteq 0.13 (d/r_o)^{5/3} = 0.13 (d/r_o)^{-5/3} \quad (20)$$

$$\sigma_S^2 \doteq 0.1 (r_1/r_o)^{5/6} \quad (21)$$

The results of the residual-wavefront-error-variance computations are plotted on Figure 12. The variance

$$\sigma^2 = \sigma_p^2 + \sigma_S^2 + \sigma_R^2, \quad \text{waves}^2 \quad (22)$$

is a measure of the resolution of the compensated solar imaging system in terms of atmospheric parameters r_1 and r_o , and the subaperture size d . The angular resolution of the compensated solar imaging telescope is given by Eq. (22)

$$\theta_c = (\lambda/D) e^{\sigma^2} \quad (23)$$

where D is the collecting aperture of the telescope. We see that the adaptive-optic compensation systems corrects the wavefront to

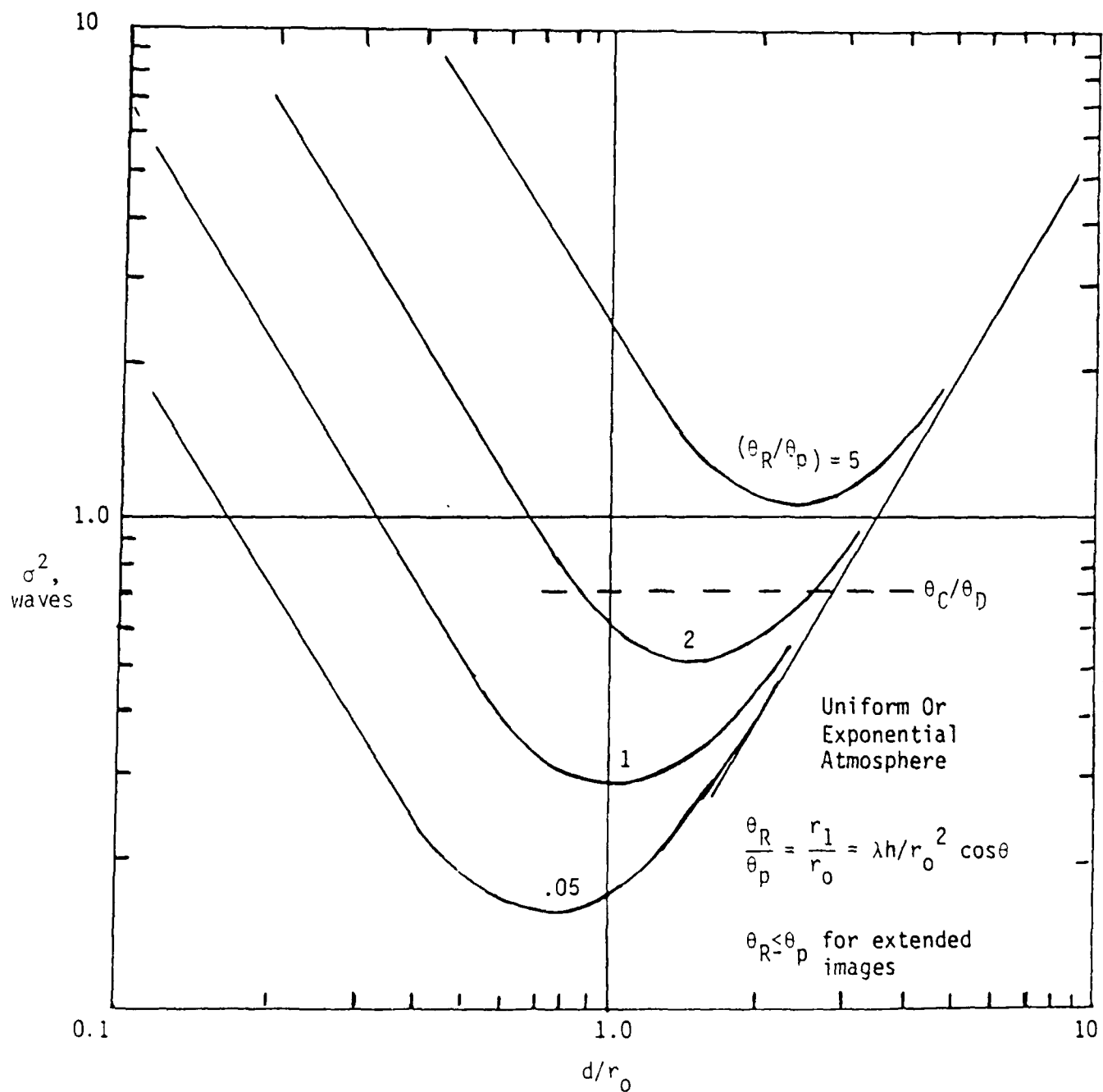


Fig. 12 Residual Wavefront Error Variance For "Ideal" Phase Compensation of an Extended Image.

within a factor of two of the diffraction-limited system when the residual-wavefront-error variance is less than 0.7. Figure 13 indicates this condition (i.e., $\theta_c/\theta_D = 2$ on Figure 12 where θ_c is the compensated system resolution and θ_D the diffraction-limited system resolution) is just achieved when $\theta_R/\theta_p = 2$ at $d/r_0 = 1.5$ if the White Sands model, Eq. (18), were used instead of Eq. (17) for the uniform or exponential atmosphere. Since $r_0\theta_R$ is a full-angle resolution and θ_p is the half-angle of the isoplanatic patch, adaptive optics is not effective when the subaperture cannot resolve the isoplanatic patch in an "ideal" AO system. If we characterize the SPNO turbulent atmosphere by $r_0 = 5$ cm and $\theta_p = 1$ arc-sec, we obtain $\theta_R/\theta_p = 2$; so that an "ideal" adaptive optics system using the optimum subaperture size $d = 1.5 r_0$ appears on the basis of wavefront error analysis to be marginally effective at SPNO.

These results derive from gating the extended solar image down to the size of the isoplanatic patch or $\theta_R = 2\theta_p$. Since the variance of the incident wavefront tip/tilts is given by (long-term turbulence)

$$\sigma_{LT} = 0.45\lambda/r_0, (1\sigma, 1 \text{ axis}) \quad (24)$$

on the average the image in any subaperture will be tilted out to the edge of the isoplanatic patch optical gate. In order to encompass this expected variation in image location from subaperture to subaperture, the optical gate, corresponding to the isoplanatic patch must be twice the atmospheric resolution or larger, or

$$\theta_R/\theta_p \leq 1.0 \quad (25)$$

Thus effectiveness of the "ideal" adaptive optics system is limited by angle-of-arrival noise rather than the wavefront error variances

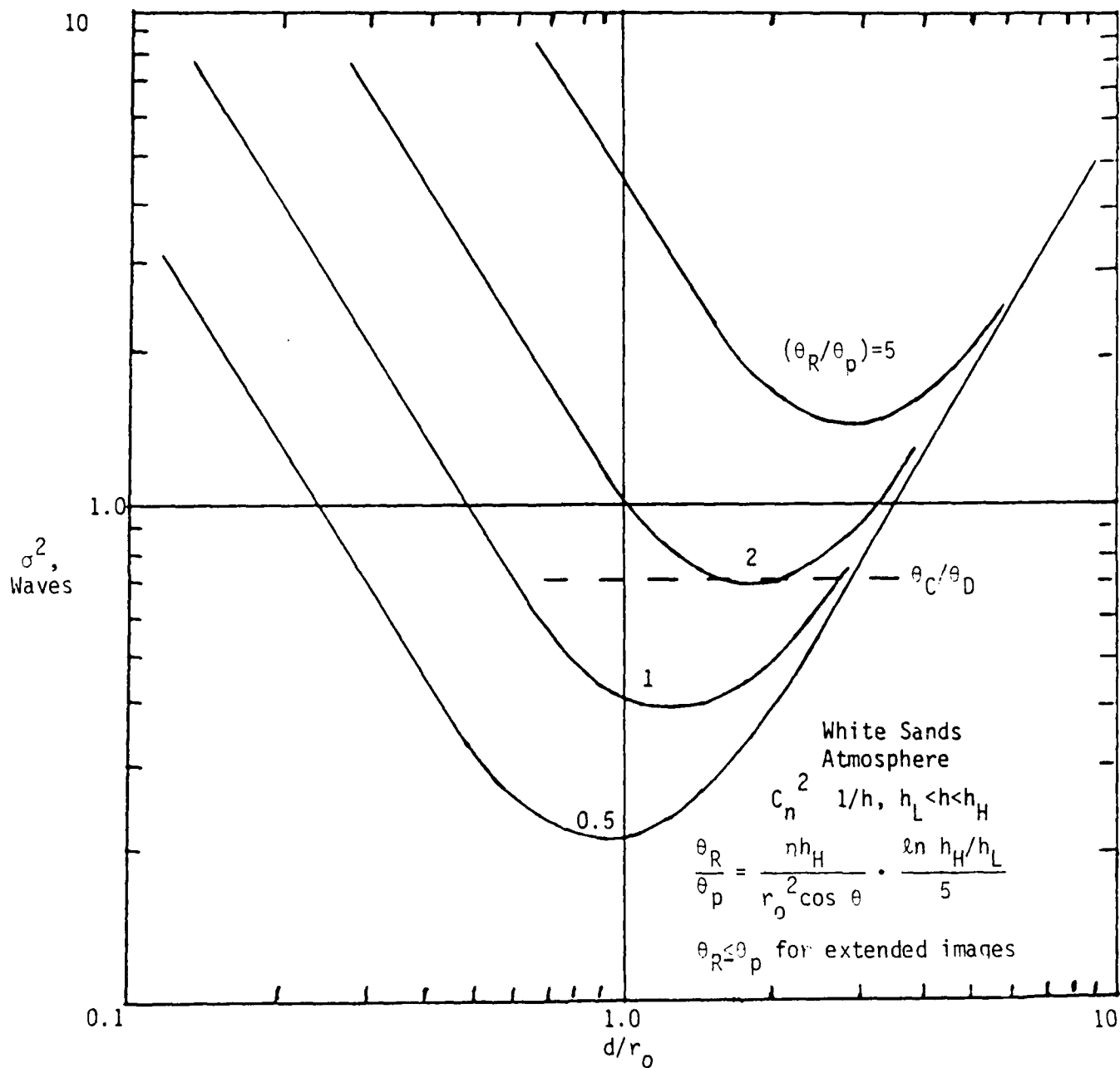


Fig. 13 "Ideal" Residual Wavefront Error Variance.

shown in Figures 12 or 13. If our characterization of the SPNO turbulent atmosphere is correct, namely that $r_1/r_0 = 2$, then even an "ideal" AO system will not effectively phase compensate an extended solar image.

The above analysis is consistent with the results obtained by Shapiro⁽²¹⁾, who examined atmospheric imaging of extended objects. He used communication theory to model the atmospheric turbulence as a wide-sense stationary uncorrelated scatter spatial channel. He found conditions under which the fields from different isoplanatic patches of an extended object may be separated in the image plane and processed individually to obtain a diffraction-limited image. The condition is termed an "underspread" channel and is obtained when the seeing limit can resolve an isoplanatic patch. Explicitly, a channel is underspread when the value of its bandwidth B and its spatial-multipath spread L (i.e., an area) satisfy the condition

$$B \cdot L < 1.0 \quad (26)$$

For overspread channels, $BL > 1$, and all inputs result in distorted outputs, according to Shapiro.

Shapiro evaluates B and L for propagation in a uniform atmosphere:

$$B = 1/\pi r_0^2 \quad (27)$$

$$L = (\lambda Z)^2/\pi r_0^2 \quad (28)$$

where Z = path length. In our notation, $L = r_1^2/\pi$. Thus the condition $BL < 1$ corresponds to the condition:

$$1 - (r_1/r_0)^2 < 1 \quad (29)$$

⁽²¹⁾ J.H. Shapiro, JOSA, 66, pg. 469 (1976)

which is more stringent than indicated by Figure 12. Shapiro's analysis has the advantage of predicting the ultimate resolution of a compensated system.

2.6 STELLAR AND SOLAR POINT-LIKE IMAGES

Anisoplanatic effects do not degrade point images because all of the incident flux of photons lies within the tube of coherence of diameter r_0 regardless of the resolution of the sensor subaperture, as long as the aperture is less than r_0 . In this case the trade-off between large errors for small subaperture sizes and large errors for large subaperture sizes remains except that the anisoplanatic error variance σ_p^2 is replaced by the photon-limited noise variance σ_N^2 , where

$$\sigma_N = 0.5 (\lambda/d)/\text{SNR} = 0.5/\text{SNR, waves} \quad (30)$$

The signal-to-noise ratio in the photon limit is given by \sqrt{N} where N is the number of photons detected in an integration time. In terms of the irradiance ϕ of photons incident on the atmosphere from a star, or the equivalent solar point-like object, the number of detected photons is

$$N = \gamma \eta d^2 \phi t/h\nu \quad (31)$$

where h = photon energy
 γ = the optical transmission coefficient
 η = detection quantum efficiency
 d^2 = area of the square subaperture
 t = integration time.

For an ideal sensor, γ is given by the atmospheric absorption and scattering. At zenith $\gamma \approx 0.8$ ⁽²²⁾. In general it is given by $\exp(-0.7/\cos \theta) = (0.8)^{1/\cos \theta}$. The highest quantum efficiencies in the visible are exhibited by Si N-on-P photo-voltaic and Si P-i-n photo conductor detectors and are in excess of 80% ⁽²³⁾. Therefore, without much loss of realism we assume for the "ideal" sensor that $\gamma\eta = 1.0$.

The dependence of SNR on detector integration time brings a fourth source of error variance into play, the bandwidth error variance σ_{BW}^2 , i.e.

$$\sigma_{BW}^2 = (2.69 t/t_{ATM})^{5/3} / \cos \theta_z, \text{ waves}^2 \quad (32)$$

where t = detector integration time
 t_{ATM} = atmospheric turbulence decorrelation time
 θ_z = zenith angle.

This expression is sometimes expressed in terms of the Greenwood frequency $f_g = 1/t_{ATM} \doteq 50\text{Hz}$ and the system detector bandwidth $f_c = 1/t$.

⁽²²⁾ RCA Electro Optics Handbook, 1974, pg. 154

⁽²³⁾ ibid, pg. 61

Both Eqs. (31) and (32) were neglected in determining the limitation to extended solar adaptive optics because the solar contrast irradiance provides a high SNR for integration times as small as 1 msec, i.e. the total solar irradiance (18) is $1390 \pm \text{W/m}^2$, therefore

$$\begin{aligned} N = \phi t / h\nu &= (1390 \text{ W/m}^2) \cdot (10^{-3} \text{ s}) \cdot (6.6 \times 10^{-34} \text{ Js}) \cdot \\ &\quad (3 \times 10^{10} \text{ cm/s} / 0.5 \times 10^{-4} \text{ cm}) \\ &= 1.39 \text{ J/m}^2 / 0.4 \times 10^{-18} \text{ J/photons} \\ &= 3.5 \times 10^{+18} \text{ photons/m}^2 \end{aligned}$$

The angular area of the solar disk observed will, in general, be comparable to $(\theta_p)^2$. The total area of the sun is about 2.54×10^6 (arc-sec) 2 . Thus the number of photons received in a subaperture is $1.375 \times 10^{12} \cdot \pi d^2 \cdot \pi (\theta_p)^2$.

The zenith solar spectral irradiance at sea level on a clear day at $0.5 \mu\text{m}$ in the visible happens to have the same numerical constant, e.g. $\phi_\lambda = 1400 \text{ W/M}^2 \mu\text{m}$, hence

$$\begin{aligned} \text{Solar } N = \phi t / h\nu &= 1.4 \times 10^8 \Delta\lambda \text{ photons}/ \\ &\quad (\text{cm}^2 \cdot \mu\text{m} \cdot \text{ms} \cdot (\text{arc-sec})^2) \end{aligned} \quad (33)$$

where $\Delta\lambda$ is the width of the spectral filter. It is now clear that even for nanometer filters, $\Delta\lambda = 10^{-3} \mu\text{m}$, and 1 cm^2 subaperture areas, and for $\theta_p = 3 \text{ arc-sec}$, and for a minimum solar contrast of 1%, the number of detected solar photons in 1 ms is more than ample to neglect photon-limited sensor noise as an

error variance source for solar imaging while maintaining a 0.2 rms bandwidth error variance.

By contrast the spectral irradiance of the brightest star, Sirius, at $0.5 \mu\text{m}$ is $10^{-7} \text{ W/m}^2 \cdot \mu\text{m}$, ten orders-of-magnitude less than sunlight. A zero-stellar magnitude star is defined to have a spectral irradiance of $2.65 \times 10^{-8} \text{ W/m}^2 \cdot \mu\text{m}$, or equivalently,

Zero-magnitude Stellar ($0.5 \mu\text{m}$)

$$N = \phi t / h\nu = 6300 \Delta\lambda \text{ photons}/(\text{cm}^2 \cdot \mu\text{m} \cdot \text{ms}) \quad (34)$$

Using the $0.5 \mu\text{m}$ spectral width of Si detectors we then obtain $N = 3100 \text{ photons}/(\text{cm}^2 \cdot \text{ms})$ from a zero-magnitude star for a milli-second integration time.

The equation for overall system error variance is then given by

$$\sigma^2 = \sigma_N^2 + \sigma_S^2 + \sigma_R^2 + \sigma_{BW}^2 \quad (35)$$

where

$$\sigma_R^2 = 0.13 (d/r_0)^{5/3}, \text{ waves}^2 \quad (36)$$

$$\sigma_S^2 = 0.1 (r/r_0)^{5/6}, \text{ waves}^2 \quad (37)$$

$$\sigma_{BW}^2 = 3553 t^{5/3} / \cos \theta_z, \text{ waves}^2 \quad (38)$$

and for stars with $0.5 \mu\text{m}$ Si detection

$$\sigma_N = 0.5/d \sqrt{t/h\nu} = 5.64 \times 10^{-4} (2.5)^{n/2} / dt^{1/2}, \quad (39)$$

waves where d is in cm, t in seconds, $\cos \theta_z \approx 1$ near zenith and n is the star magnitude.

We evaluate the detectable star magnitude using the following nominal conditions:

$$d = r_1 = r_0 = 5 \text{ cm and } t = 2 \text{ ms}$$

$$\text{so } \sigma_R^2 = 0.13, \sigma_S^2 = 0.1, \sigma_{BW}^2 = 0.113$$

$$\text{and } \sigma_N^2 = 3.17 \times 10^{-3} \cdot (2.5)^N \quad (40)$$

For ideal system performance,

$$\sigma^2 \leq 0.7 \text{ as before, therefore}$$

$$\sigma_N^2 \leq 0.36, \text{ for which}$$

$$n \leq 5\text{th magnitude stars.}$$

Thus ideal sensor/perfect deformable mirror adaptive systems are potentially effective for 5 magnitude and brighter stars near zenith.

2.7 SOLAR ADAPTIVE OPTICS USING THE LSI³ WAVEFRONT SENSOR

The high resolution solar images provided by the Sacramento Peak National Observatory (SPNO) include the continuum image and the hydrogen line (0.66 μm) image, plus variations around line-center which indicate a line-width of less than 4 \AA . The line-center image is characterized by contrast striations of 100 μR to 1 mR in lengths, well beyond isoplanatic patch limitations.

The continuum image consists of a continuous granular field with small contrast and an occasional "pore" of very high contrast. The granular field consists of 0.7 to 3 arc-sec size granules with a mean size of 2 arc-sec as shown in Figure 14. Filmed data indicate that the granules individually break up and disappear on the time-scale of each film sequence (~30 sec.). The solar "pores" in the granular field are, in length, about twice this size (4 arc-sec). They are isolated and have an irregular, time-varying shape over the 30 sec. time-scale.

It therefore appears that the isoplanatic angles associated with the SPNO atmosphere are too small (~1 arc-sec) to image either granules in the continuum field or pores in the granular field. These solar features are larger than the sensor field-of-view (FOV) which is optically gated down to the size of the isoplanatic patch.

It is interesting that this condition is consistent with wavefront error analysis of a realistic system. If we extend the results of Section 2.0 to a realistic AO system, the essential difference being the incorporation of "realistic" deformable mirror (DM) technology characterized by a "fitting" error variance

$$\sigma_{\text{FIT}}^2 = k(d/r_0)^{5/3} \quad (41)$$

where $0.3 < k < 0.5$ is typical of state-of-the-art reconstruction of DM phase, the residual total error variance still provides better than 2xDL system performance as shown in Figure 15. The variance on Figure 15 is for a single subaperture. To obtain the full aperture wavefront error variance we must use Fried's relationship:

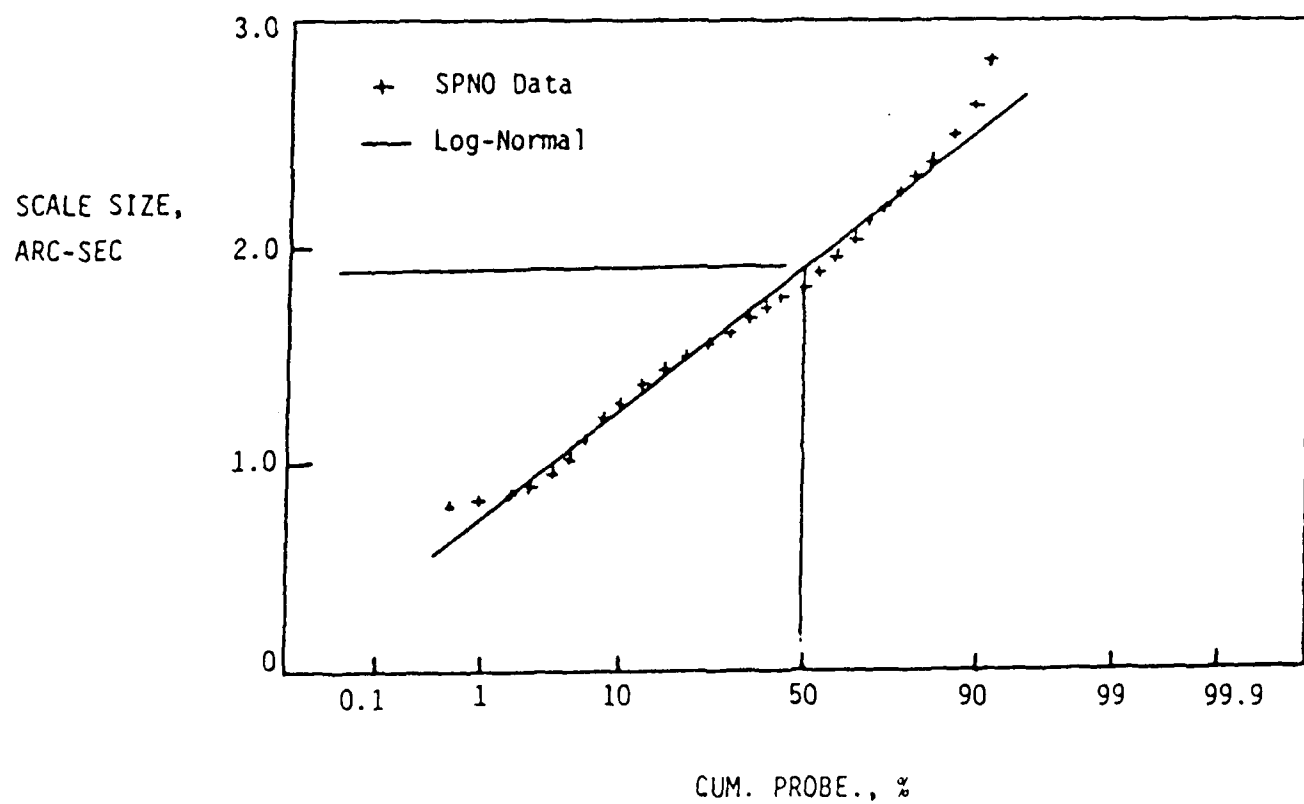


Fig. 14. Log-normal distribution of solar granule scale sizes from analysis of SPNO photographic data.

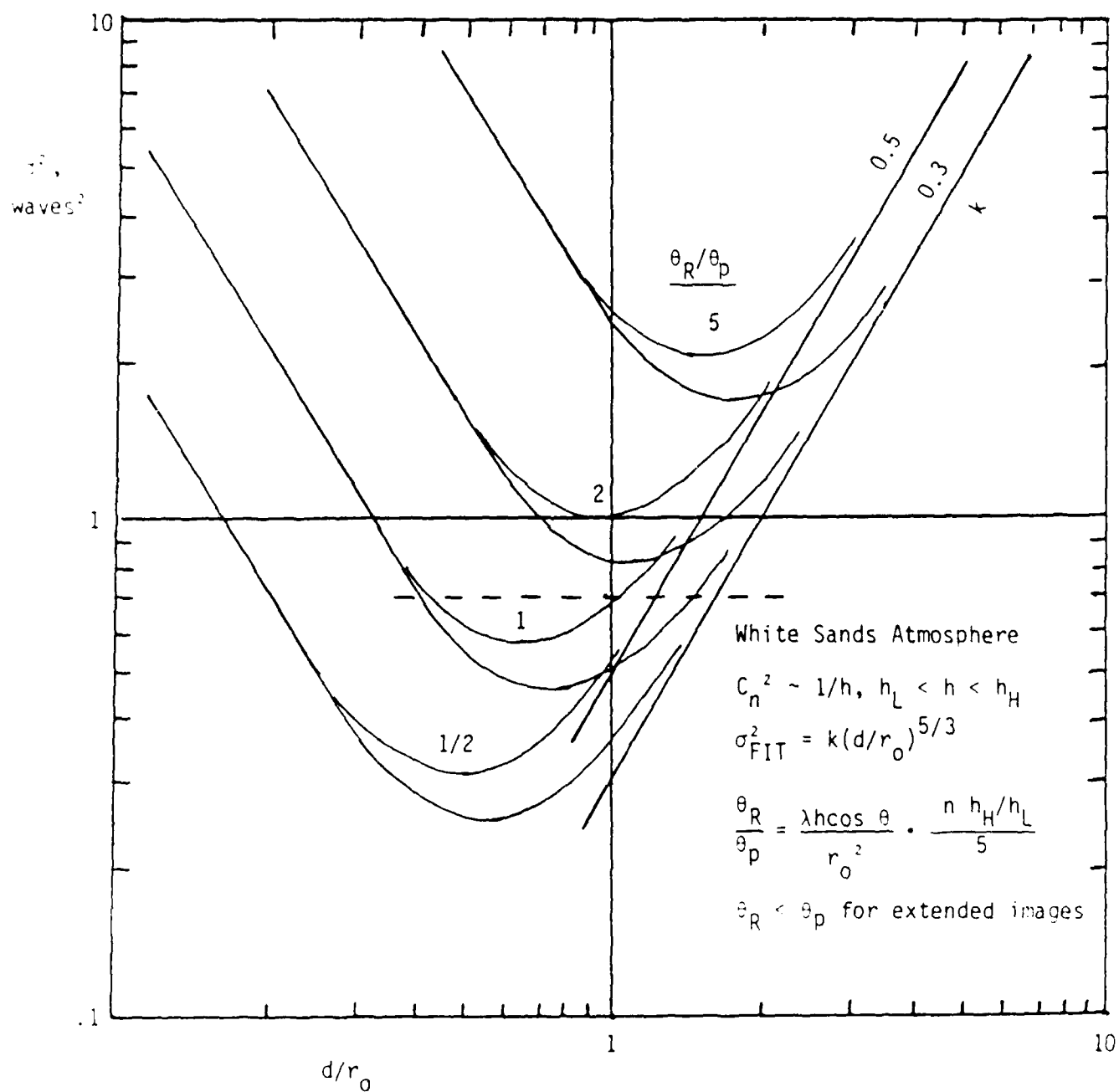


Fig. 15. Residual wavefront error variance for a realistic adaptive optics system phase compensation of extended images.

$$\sigma_F^2 = \frac{2}{3} \sigma_{SUB}^2 \left(1 + \frac{1}{4} \cdot n \cdot N\right) \quad (42)$$

where $N = \pi/4 (D/d)^2 = \pi/4 (75/5)^2 = 175$ is the number of subapertures on the SPNO full aperture. Therefore, $\sigma_F^2 = 1.5 \sigma_{SUB}^2$. Even adding this factor to Figure 15, the $\theta_R \leq \theta_p$ curves are 2xDL or better for a correctly sized subaperture; i.e., $d = 3/4 r_0$. However, for a SPNO atmosphere characterized by $\theta_R \geq 2\theta_p$, a 2xDL performance cannot be realized.

The dependence of θ_R / θ_p on r_0^{-2} suggests that under "good seeing" conditions, better than 2xDL phase compensation can be achieved. The cumulative distribution of r_0 statistics measured with a 0.5 μm seeing monitor at Maui and shown on Figure 16 indicates that r_0 rarely ($< 1\%$) is even 50% larger than the mean. Thus "good seeing" conditions are indeed rare at Maui and probably the same at SPNO. Thus from "extended image" wavefront error analysis, 2xDL AO system performance will be rare at SPNO.

Adaptive optics is still effective on point-like images such as stars because the total image is confined to the isoplanatic patch. But the isoplanatic patch may be comparable to even the smallest solar features, the solar granules and the high contrast pores contained within them. Therefore, there may not be any solar features smaller than the isoplanatic patch. This was the conclusion of studies⁽²⁴⁾ done at AOA some years ago. As a result of these considerations, we decided that adapted optics could only be useful for compensated solar imaging if the small sensor FOV could be scanned across the solar surface. As discussed in the following section, we are only able to obtain a limited scanning ability.

⁽²⁴⁾ Shao, Feinleib, Bowker, Schmutz and Tubbs, SPNO Conference, March 1981, pg. 471.

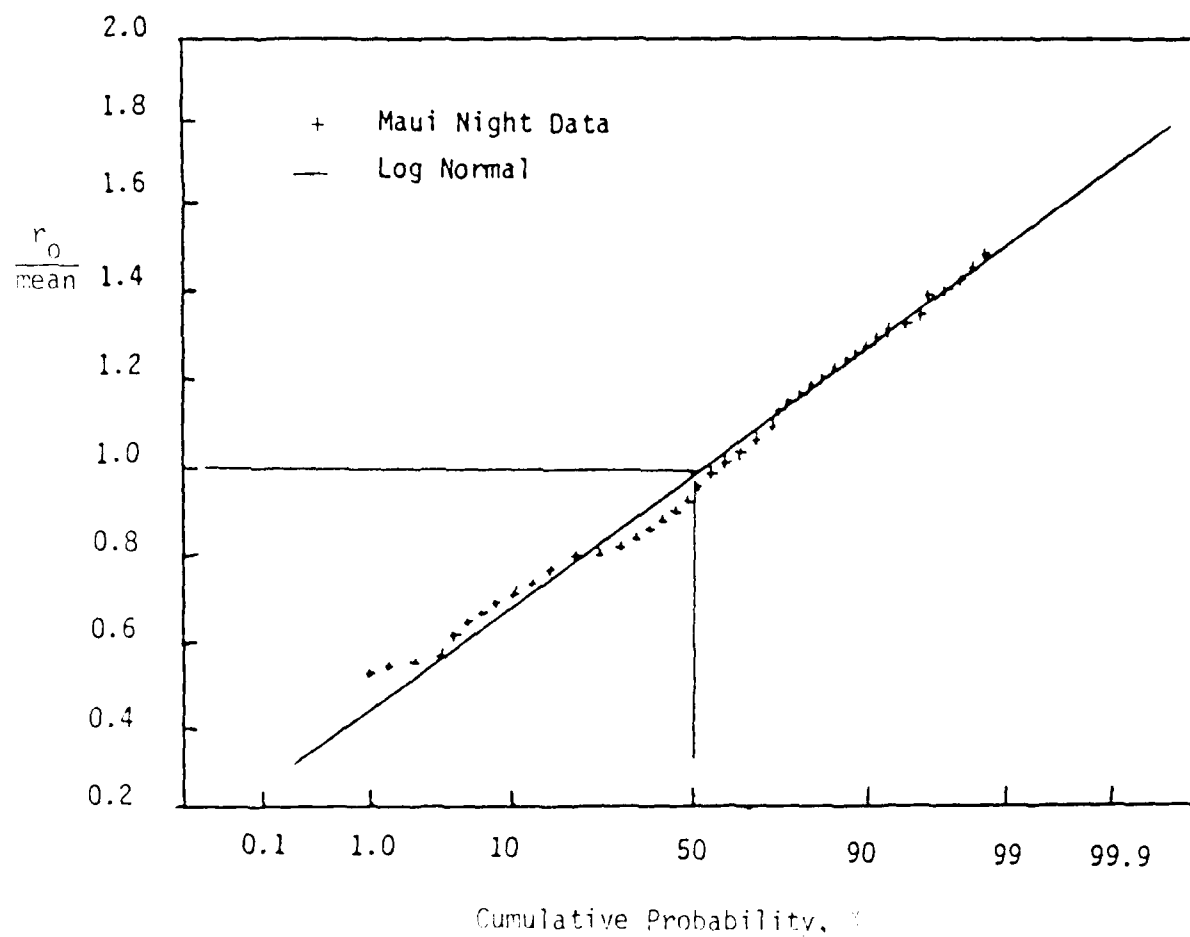


Fig. 16. Log-normal correlation scale distribution compared to Maui data where mean = 9.63 cm, σ = 2.23 cm.

2.8 LSI³ EDGE TRACKER

In order to obtain adaptive-optic image enhancement on images which extend beyond the isoplanatic subaperture field-of-view (FOV), AOA has proposed the development of an LSI³ "Edge-Tracker" to replace the usual LSI³ centroid algorithm where each subaperture is a quad cell centroid tracker. The basic LSI³ sensor configuration is retained where the detector plane of each subaperture is divided into four (or more) detectors and image is nutated in a circle of radius r . The processor algorithm is modified so as to drive the track towards the edge of the image rather than its centroid. We propose to accomplish this by essentially processing the opposing set of quadrant detectors. One set would use the normal processor algorithm such that the track would be driven towards the bisector of the image that balances the detector outputs of these two opposing detectors. The orthogonal set of detectors would have a modified processor algorithm where the gain of one detector is larger than the other. This creates an imbalance such that an otherwise centroid tracker is driven off-center in the direction of the quad cell with the larger gain. The amount of gain, a variable, would determine how "close-to-the-edge" a track is obtained, and the orientation of the quad cell with respect to the center of the image would determine the track point along the edge of the image. Therefore it is desirable that the orientation of the quadrant boundaries with respect to the image symmetry is also a variable. If so, then adjustment of quad cell gain and orientation may provide a means to adjust the track point around the edge of an arbitrary image. Such a tracker would provide a limited scan capability on isolated high contrast images such as solar pores or sunspots.

A separate fast-tracking mirror (FTM) is required to maintain a centroid track on the image feature. This is possible because the size of the isoplanatic patch depends on the size of the aperture used to process the image; in fact, it is inversely proportional to the processing aperture such that the residual wavefront rms error

variance is given by⁽²⁵⁾

$$\sigma_x = \frac{\lambda(\theta h)^{0.88}}{D^{1.047} r_o^{5/6}} \quad (43)$$

where θ is the radius of the FTM field-of-view. If we wish to track sunspots at $\lambda = 0.5 \mu\text{m}$ up to $100 \mu\text{R} = 20 \text{ arc-sec}$ in diameter in a $h = 10\text{Km}$, $r_o = 5 \text{ cm}$ atmosphere, the residual tilt error is

$$\sigma_x = \frac{0.3 \text{ arc-sec}}{D^{1.047}} \quad (44)$$

Therefore stabilization of large, isolated images is possible if the tilt is averaged over aperture diameters approaching one meter. Note that adaptive optics with $D \approx 5 \text{ cm}$ and $\sigma_x \approx 7 \text{ arc-sec}$ does not work.

2.9 THE LSI³ SENSOR

The LSI³ Sensor concept is illustrated in Figure 17. Although the optical configuration appears very different from the basic Hartmann test, the LSI³ is essentially a derivative in which the quad cell detecting element is replaced by a four-sided prism element, and the subaperture dividing elements are the detector elements of the four detector planes. The figure illustrates a four subaperture system. In general the four detector planes will be comprised of many more than four detector elements; there will be at least one detector per subaperture in each array. The figure shows that the light from subaperture "a" of wavefront W is imaged onto each of the four detectors labelled "a" in the figure.

⁽²⁵⁾ Valley, APP OPT 19, 514 (1980). Eq. (43) is obtained using asymptotic expressions available in this paper.

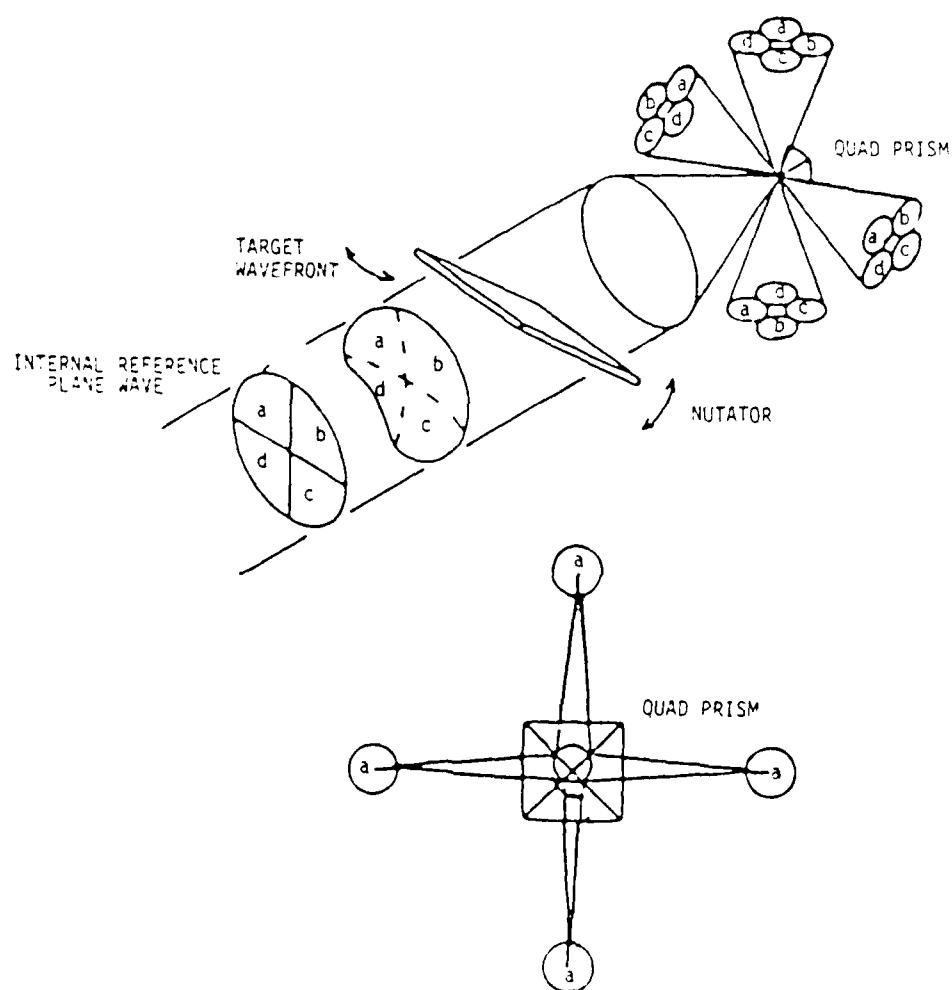


Fig. 17. LSI³ sensor. The basic optical configuration of the LSI³ sensor is depicted. The detail shows how the quad prism performs a quad cell position measurement for a selected subaperture.

Assuming this to be true, as will be shown later, it is then readily seen that the four detector signals from the "a" detectors can then be processed as a quad cell to determine the tip and tilt of the wavefront of a subaperture "a". Similarly, the tips and tilts of each of the other subapertures, "b", "c" and "d", can be measured by their respective detector sets. The final result is a wavefront measurement analogous to the Hartmann test.

A reference plane wave is alternately measured and a comparison of the target wavefront and reference is made. This is done to reduce many of the mechanical alignment tolerances to which the Hartmann test is extremely sensitive. The nutation of both target and reference wavefronts is used as an additional aid in the tolerancing and also to produce an AC modulated signal for more efficient signal processing.

In Figure 18, the assumption that the single quad-prism performs a similar function as a quad cell detector for each subaperture is verified. The focal lengths of the lenses are chosen so that the portion of the input wavefront corresponding to subaperture "a" is imaged onto the two shaded detectors. These two detectors correspond to two of the "a" subaperture quad cell detectors; the remaining two detectors are in arrays that are above and below the illustration. Figure 19 illustrates pictorially the light intensity of the subaperture "a" point spread function as it nutates around the prism tip. Each detector "a" receives that portion of the intensity distribution reflecting from its respective prism face. These four detectors are seen to have a similar response to the tip and tilt of a subaperture wavefront as a quad cell.

It is thus seen that any incoming wavefront can be divided into any number of subapertures by changing the density of detectors in each of the four detector planes. No other changes to the sensor -

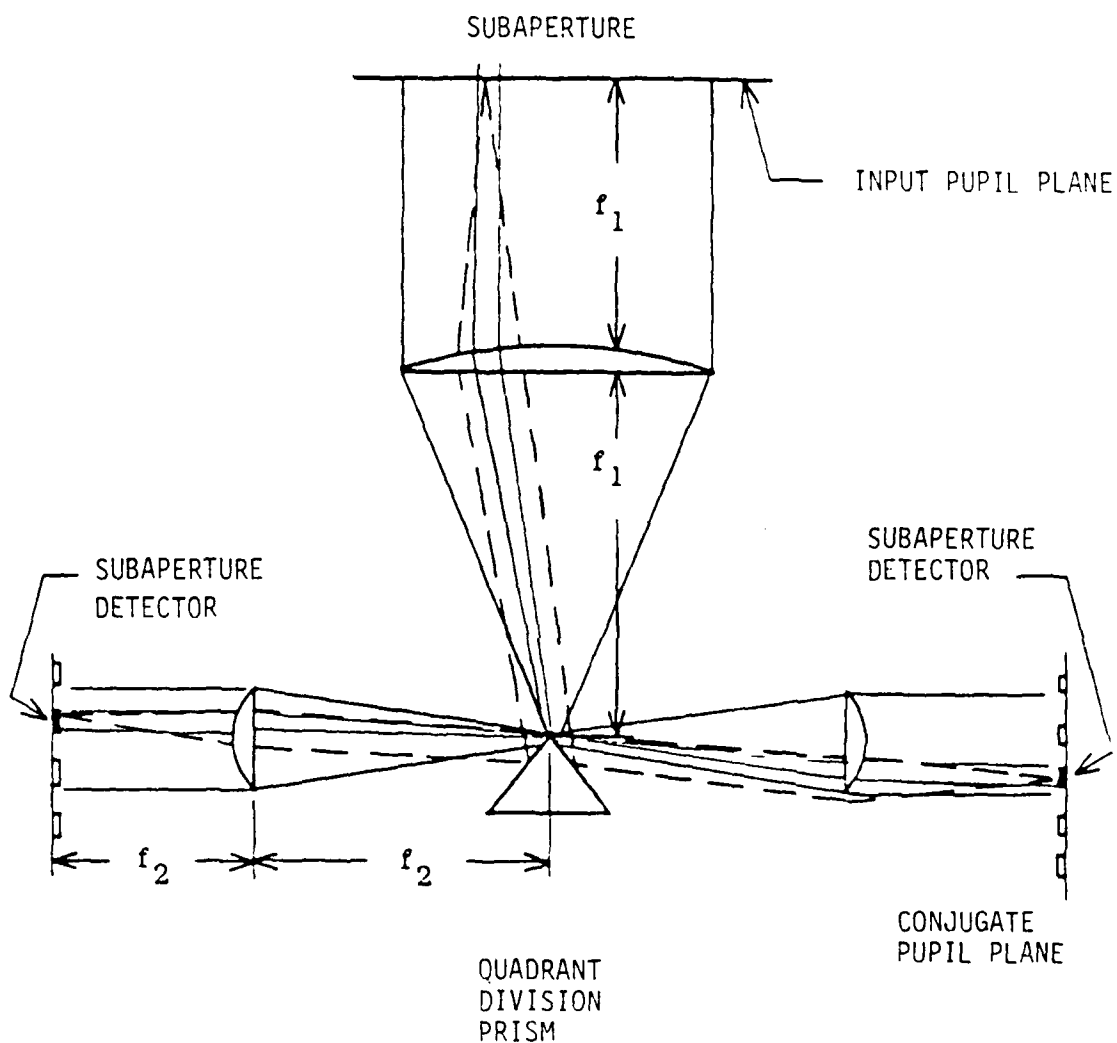
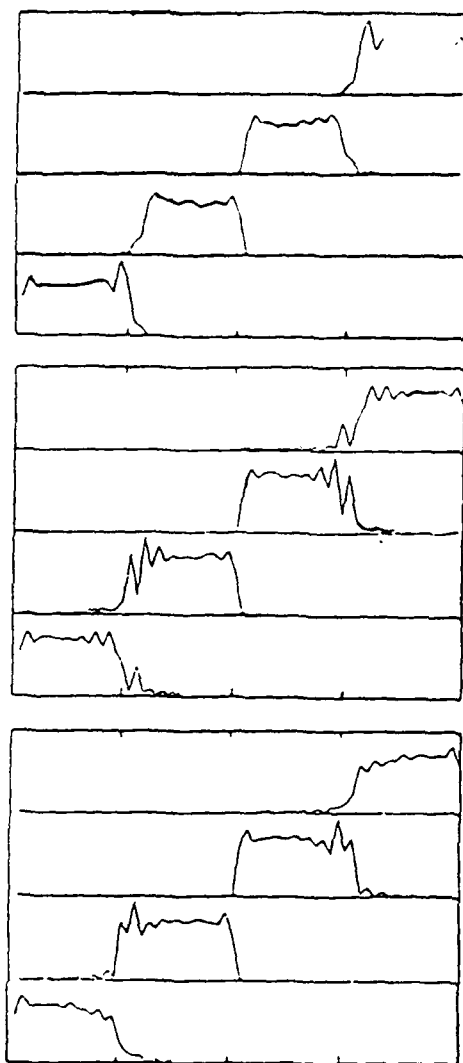
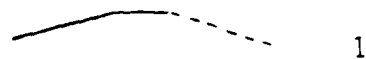


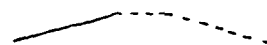
Fig. 18. Detector arrays as pupil dividers. In each quadrant channel a single detector element is projected onto the input pupil plane and defines a subaperture. The 4 detector elements, one from each channel, which map onto the same input subaperture, form a quadrant detector which may then be used to determine the wavefront tilt in that subaperture.



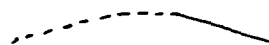
SUBAPERTURE



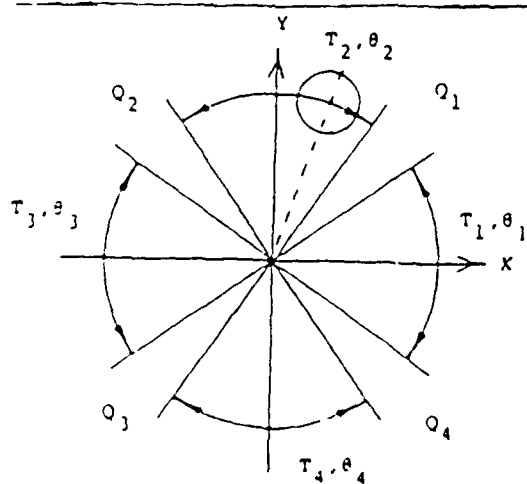
1



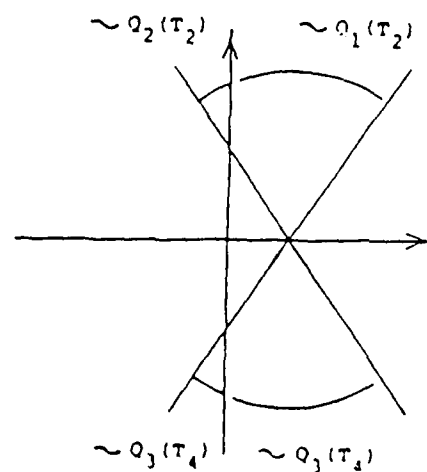
2



3



19a. SCS algorithm gate-angle geometry.



19b. Tilted gate-angle geometry.

Fig. 19. LSI³ diffraction code - simulated waveforms.

the optical nutator or quad divider prism - are required. It is also evident that there is no longer a requirement that the detector planes be made up of a special arrangement of detectors such as the dense array of quad cells required for the I³ Sensor. The feature greatly simplifies the design of a large scale wavefront sensor system.

The LSI³ thus appears to be a leading candidate for a wide range of adaptive optics applications. It retains many of the performance advantages of the Hartmann sensors, and also incorporates a key feature of the shearing interferometer, i.e., that the detector planes are simple detectors. There are, however, several unexplored problems which must be answered to ensure the viability of the concept. Of immediate concern is the ability to align the four detector arrays and the prism so that there is an exact mapping of each subaperture wavefront onto its corresponding four detector set. The number of alignment degrees of freedom is limited, so that it is no longer feasible to align detectors individually as the number of detectors increases. Instead, present systems under development at AOA make use of the reference input system to automatically align the optical axis with the prism, and then to use suitable fiducials to align the detector planes relative to one another. The saving grace is that the detector planes are well suited to current CCD or other integrated detector array technology and thus the physical fidelity of the array configuration can be relied upon for alignment.

A more subtle question is the effect of diffraction from the prism on the detected signal from each subaperture. Going back to Figure 16, it is clear that with only one subaperture as shown, the detected signal is a simple intensity division with perhaps some small light losses due to diffraction from the prism edges. However, in the general case, the focused light spot on the prism is a coherent superposition of the light from all the subapertures.

The first order effect is to treat each subaperture intensity distribution separately since each subaperture is geometrically imaged onto its own set of detectors. The diffraction of light from the prism edges is a second order effect which tends to spread the light from each subaperture into neighboring detectors. This could be a source not only of subaperture signal loss, but also of crosstalk from subaperture to subaperture and x to y channels among the subapertures.

2.10 DIFFRACTION EFFECTS

Some progress has been made in exploring the diffraction problem in the LSI³ Sensor. Generally it is not a simple effect to investigate either theoretically, by simulation, or experimentally because there is a large number of possible cases to be tried before a definitive conclusion can be reached. It is important to determine if the effect of a tip or tilt in one subaperture spreads into other subapertures. To do this by simulation, a single subaperture wavefront is defined by a 32x32 grid. The diffraction pattern is calculated by a Fourier transform at the prism. This diffraction pattern is then nutated on the prism in 32 increments and then the intensity at a subaperture detector is calculated by an inverse Fourier transformation and integration over 32 nutation steps. On the computer available for this work, a Data General Nova, a single case required 12 hours to calculate so that very few cases could be run in a reasonable time. Nevertheless, a sufficient number of cases were run to demonstrate a range of diffraction phenomena and some results are described below.

An example of the temporal detector response of a simulated array of three adjacent subapertures is shown in Figure 19. Each blocked group of pair responses is the 4-detector quad cell response for a single subaperture. The particular subaperture is identified to the right by a solid line where subaperture 1 has a small, positive tilt, subaperture 2 has zero tilt, and subaperture 3 has an equal,

small, but negative tilt. The detector response is oscillatory, suggestive of the coherent ringing in half-plane diffraction solutions. Similar behavior has been observed experimentally with the LSI³ sensor but experimental results are not available for publication.

Since image or tip/tilt information derives from the detector response as the nutated, focused spot crosses the LSI³ pyramid edges, it was originally conjectured that the modulation of the signal by diffraction effects might seriously interfere with accurate tip/tilt measurements. Simple analysis indicates that scattering from slightly rounded pyramid edge (~10 μm radius) is insignificant, amounting to a spreading of 1% of the signal across the detector array. However, diffraction at the edge of the beam reflected from the flat surfaces of the pyramid appeared to be a 25% effect, perhaps leading to significant crosstalk in the x and y tilt axis (tip and tilt) and crosstalk between subapertures. Therefore we conducted an analysis in which LSI³ simulated measurements of tip/tilt were compared to the known input tip/tilts across each subaperture.

2.11 LSI³ ALGORITHM

The results of LSI³ simulations revealed an unexpected benefit from use of the LSI³ algorithm, namely its ability to capitalize on the symmetry of the detector response shown in Figure 19 so that diffraction effects are cancelled out during tip/tilt measurement.

The SCS algorithm can be defined by reference to figure 19a. A focal spot corresponding to the target image is nutated on a quad cell. The quadrants are labeled $Q_1 - Q_4$. Four intervals in the nutation cycle are also defined, as periods $T_1 - T_4$, or nutation angular intervals $\theta_1 - \theta_4$, which are equivalent since with circular nutation the spot velocity is constant. Measurements of spot centroid displacement are made at different times for the two axes: x-displacement (tilt) is measured during periods $T_1 - T_3$, while y

(tip) is measured during T_2 and T_4 . The algorithm defines the spot position, and therefore input tilt, by a numerator proportional to displacement and brightness, and a denominator proportional to brightness only; i.e., a tip measurement is given by

$$X_{NUM} = (Q_1(T_2) - Q_2(T_2)) - (Q_4(T_2) - Q_3(T_2)) + (Q_4(T_4) - (Q_3(T_4))) - (Q_1(T_4) - Q_2(T_4))$$

$$X_{DEN} = (Q_1(T_2) + Q_2(T_2)) + (Q_4(T_2) + Q_3(T_2)) + (Q_4(T_4) + (Q_3(T_4))) + (Q_1(T_4) + Q_2(T_4))$$

$$\Delta Y = \frac{X_{NUM}}{X_{DEN}}$$

The motivation for this definition can be seen by separately examining the effect of each term. The differences $Q_1(T_2) - Q_2(T_2)$ and $Q_4(T_4) - Q_3(T_4)$ correspond to measuring the intensity imbalance between right and left half-planes, during those times when the spot is expected in those quadrants, which occurs due to spot displacement. The imbalance occurs because a shift of the spot appears as a shift in the center of the nutation circle, as shown in Figure 19. The imbalance between the signals integrated from each quadrant can be interpreted as proportional to the differences in arc lengths bounded by the integration intervals and quad cell boundaries, as shown in the figure. The property of the SCS algorithm to cancel diffraction effects derives from the subtraction of the difference term measured at T_4 from that measured at T_2 plus the observed symmetry in detector responses on Figure 19.

The other numerator terms $Q_4(T_2) - Q_3(T_2)$ and $Q_1(T_4) - Q_2(T_4)$ are the power differences seen when the focal spot is not present in the

respective quadrants. For an ideal, sharply bounded spot, the second set of terms should represent differences only in background radiation or detector responses, and serve to cancel these contributions from the first set, so that the background-cancelling terms make the LSI³ algorithm an AC algorithm. The position information is impressed on a carrier at the nutation rate. Out of band noise, particularly 1/f noise, is rejected by the same cancelling action that removes background illumination.

The function of the denominator is to normalize the output to spot brightness. It can be seen as a sum of left and right half-plane terms, rather than a difference as in the numerator. Background cancelling terms are still present.

For spots whose radii exceed the size of the nutation radius or for less well bounded spots (such as the Airy pattern or Gaussian distributions commonly encountered), the spot intensity is never wholly absent from a quadrant even though nutation may have moved the spot farthest away from that quadrant during a cycle; in these cases spot power as well as background power is cancelled from the numerator, and modulation is therefore an important consideration. The results of the LSI³ simulation indicate that sensor response is linear (i.e., diffraction effects are completely cancelled) only when the nutation radius exceeds the spot size.

In summary, the diffraction simulations have demonstrated that in spite of significant diffraction effects, the properties of the LSI³ algorithm are such that

1. there is no crosstalk in tip/tilt measurements or between subapertures;
2. sensor response is linear provided nutation radius exceeds spot size;
3. the proportionality between input/output tip/tilts

decreases with increasing nutation radius, as expected,
and

4. the proportionality and instrument sensitivity depends
on subaperture spot size rather than full aperture spot
size.

III. MODS FULL APERTURE IMAGE SHARPENING

3.1 FULL APERTURE EXTENDED OBJECT ERROR SIGNAL ALGORITHM

The foregoing study of the performance of standard adaptive optic systems clearly demonstrates that any technique that utilizes subapertures of a size comparable to the isoplanatic patch will fail for daytime imaging of extended objects such as the solar surface. This realization leads us to consider image sharpening methods that use the full aperture image to derive the correction element drive signal. Such methods eliminate the problem associated with the large diffraction limit of small subapertures. A number of different techniques for image sharpening have been proposed⁽²⁶⁾. However, most of these depend upon the presence of a point-like source in the object plane. In general, this condition will not be satisfied during imaging of the sun's surface because of the relatively low contrast present in that scene and therefore a different approach is necessary.

The most important constraint on the selection of a sharpening algorithm results from our lack of specific a priori information on the structure of the solar surface. Thus any algorithm for calculating the quality of the image cannot make reference to the "ideal" image as a test of that quality. Rather, an error signal must be derived that in some sense indicates the quality of the image relative to the theoretical performance of the imaging system without regard to the nature of that image.

One physical quantity that is well defined for any imaging system is the modulation transfer function (MTF). If one could measure the transfer function of the imager including the atmospheric aberration and compare this function with the theoretical MTF of the imager, the strength of the atmospheric

(26) O'Meara, T.R.J., Opt. Soc. Am, 67, 306.

aberration could be determined.

It can be shown that, for any mode of aberration satisfying the condition

$$F < D/\lambda \quad (47)$$

where D is telescope aperture, F is the spatial frequency measured in cycles per radian and λ is wavelength, the overall MTF of the aberrated optical system is less than the unaberrated MTF at all frequencies. Stated differently, this requirement is that the mode not lead to image spatial frequencies above the diffraction limit of the aperture. Since, in general, for the solar imaging case we will not be applying modal correction at frequencies close to this limit, it follows that the value of the spatial power spectrum of an atmospherically distorted solar image is everywhere less than the power spectrum of the undistorted image.

To show this we begin by examining the performance of an imaging system in the isoplanatic regime. For no aberration of the incoming wavefront, the MTF (\mathcal{H}) of a telescope is given by

$$\mathcal{H}(f_x, f_y) = \frac{J_1(f_x, f_y)}{J_0(f_x, f_y)} \quad (48)$$

where J_0 is the spatial power spectrum of the object intensity distribution and J_1 is the power spectrum of the image. Unfortunately, we cannot directly measure the transfer function without knowing J_0 . However, it is clear that \mathcal{H} is bounded from above by J_1 since J_0 is at most equal to unity at a given spatial frequency.

It is also well known that the transfer function \mathcal{H} is given as well by the autocorrelation of the complex pupil function. In the absence of any aberration, the pupil function is identically equal

to unity at all points (this assumes that the pupil functions are normalized so that the intensity is uniform and equal to 1). Thus, the autocorrelation function is simply the area of the intersection of the entrance pupil with one displaced by the image plane equivalent of the pupil spatial frequency. If we add an arbitrary phase aberration to the system due to transmission through the atmosphere, the pupil function G may be represented as

$$G = e^{ikP(X,Y)} \quad (49)$$

where $P(X,Y)$ is the phase function over the pupil. In this case the autocorrelation function is given by

$$L(f_x, f_y) = \iint e^{ikP(y+\Delta x, y+\Delta y)} e^{-ikP(x', y')} dx' dy' \quad (50)$$

For any phase function, the value of the product of the two pupil functions can never be greater than unity. Thus at any spatial frequency, the value of the autocorrelation function cannot be greater than that found in the absence of aberration. It follows then that the MTF of the optical system is maximized at each frequency by removing the aberration. Further, if a new quantity is defined that is the integral of the MTF over all allowed spatial frequencies, it is clear that that quantity is also a maximum when the incoming wavefront is unaberrated. This is exactly the property we desire for the error signal in a servo loop. If the integral of the MTF is forced toward a maximum, we can say that independent of the properties of the object being imaged, the wavefront aberrations will be forced toward zero. It is not necessary to know either the distribution of spatial frequencies in the source or the ideal transfer function of the imager to utilize this error signal. We

only require that the power spectrum of the source not change on a timescale comparable to the update time of the servo loop. For the case of atmospheric compensation of the solar image, this requirement is easily met, since the timescale of changes on the solar surface is much slower than that of the variation in the aberration.

3.2 MODS SERVO SYSTEM

Having settled on this algorithm for the generation of an error signal, it became necessary to define the complete MODS system both as it would be realized in a real-time operating environment and in the form of a numerical simulation to be used for initial testing of sensitivity and stability. As implied by the name, the MODS system depends upon a dithering technique. In many respects, it is similar in concept to the multi-dither processes such as described by O'Meara. However, rather than utilizing the independent elements of an active optical ditherer to define the pupil dither function, we decompose the pupil into a set of orthogonal modes, applying independent dithers to each mode. In the case discussed here, Zernike modes were used, though there is no reason that a different set of orthogonal modes could not be chosen.

A schematic representation of the system is shown in Figure 20. The input beam from the telescope passes first through the correcting element and then a portion is split off and is sent on to the MODS image quality detector. As indicated in the figure there is a high-speed correlation tracker loop closed around the MODS system. This is necessary because the MODS detector is not sensitive to translations of the image, only to higher order aberrations. However, it should be noted that since the MODS system relies on a full aperture image, that same detected image may be used as input to the correlation tracker. This is because, on average, the ditherer will not introduce tips and tilts into the beam, those being orthogonal to the other Zernlike modes. Thus, the



61

correlation loop does not require splitting off any light from the input beam.

Within the MODS module itself, the light passes first through an active dither element. The number of individually addressable elements required is determined by the highest order mode that one would want to correct. It is necessary that that mode be adequately represented on the surface of the ditherer. After the dither element, the input beam is imaged onto a two-dimensional detector that can be framed at a rate at least several times faster than the timescale over which the atmosphere changes significantly. This detector must include a region of the image plane that encompasses a single isoplanatic patch. In addition, the resolution of the detector should be close to the diffraction limit of the telescope in order to adequately sample the sharpened image. Thus, the number of pixels across the detector is given by the ratio of the resolution limit of the telescope to the size of the isoplanatic patch. The signal from this detector is then processed to yield the desired error signal. This requires that the power spectrum of the image be calculated. Since, for a typical solar telescope in average daytime conditions the size of the detector array is of the order of 32x32 pixels, a considerable amount of numerical calculation must be done to arrive at the true 2-D power spectrum. To save calculation time, we suggest that this process be treated as 64 parallel 1-D Fourier transforms rather than the full 2-D transform. While the results of these two calculations are not identical, we show in the simulations reported here that they are operationally equivalent and the 1-D version offers a significant computational advantage. Once the power spectrum is calculated, it need only be summed to produce the needed error signal. The normalization of the power spectrum is taken to be such that the power in the zero frequency bin (i.e., D.C.) is unity.

When the MODS system is in operation, the ditherer has applied to it drive signals that cause each Zernike mode to be modulated at a fairly low level (on the order of a few tenths wave amplitude). These modes may be modulated separately or they may be multiplexed in the frequency domain. In either case, the derived error signal is synchronously detected and individual error signals for each mode are produced. These error signals are used to calculate updates for the correction element.

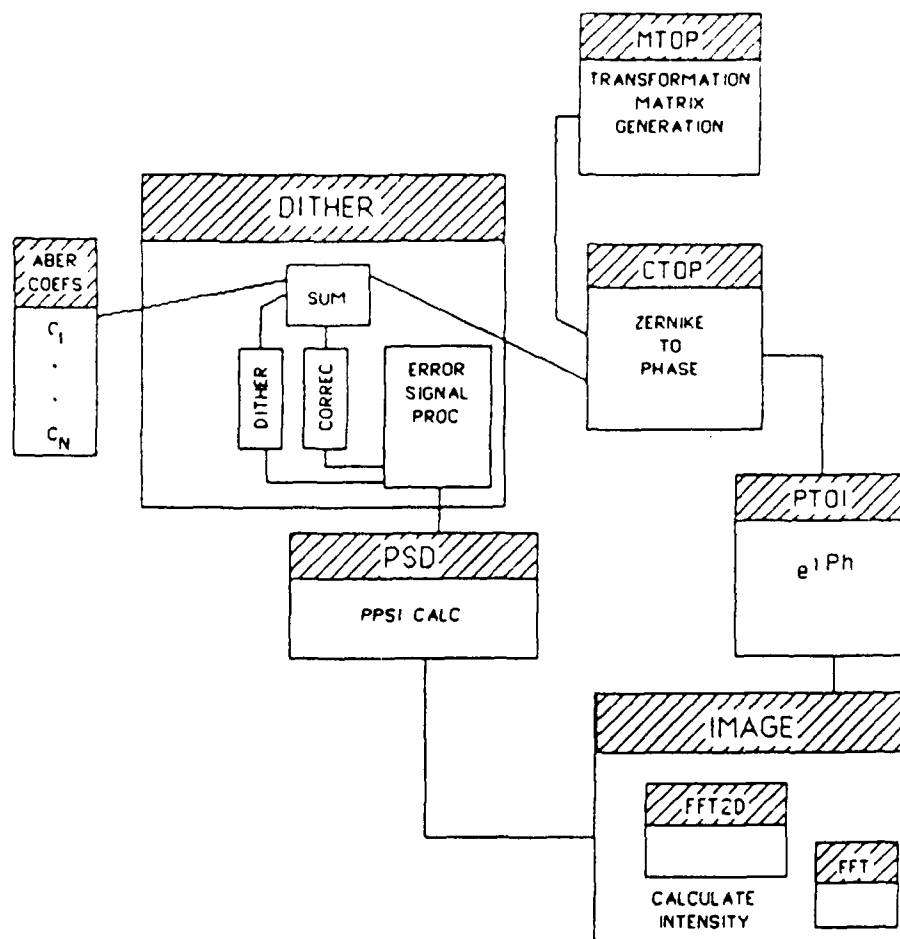
3.3 NUMERICAL SIMULATION OF MODS

In order to make the problem of the simulation of the MODS concept a tractable computation for the Data General Nova computer available for the task, it was necessary to make some simplifications in the system. Perhaps the most significant of these simplifications stems from the need to simulate the imaging device, i.e., the telescope. This is done by performing the true 2-D Fourier transform of a complex pupil function that includes the effects of the aberrations, the corrector element and the ditherer. Because of the memory space limitations of the Nova, it was necessary to restrict the size of the complex array over which the pupil function was defined to 64x64 elements. The coarseness of this sampling prevents us from adequately representing large aberrations of the pupil function. This may be seen if one considers that the amplitude of the phase aberration appears as a spatial wavenumber in the expression for the pupil function. Large amplitudes in phase require high spatial frequencies in the pupil function and thus fine sampling of that function for good numerical representation. Tests performed with this code indicate that phase aberration amplitudes must be limited to less than 3 waves in the lower order modes to avoid this problem.

Within this 64x64 pupil array, a square aperture was defined with a size of 32x32 elements. Outside this aperture the pupil function was forced to be zero. This has the effect of defining the

scale of the image plane. The Fast Fourier Transform (FFT) routine assumes that the input function is periodic with a period equal to the size of the input array. Therefore, the lowest frequency features that may be represented in our 32 element wide aperture have a period of 1/2 of the 64 element array, or equivalently, a frequency of 2 cycles per 64 elements. Since the output of the FFT is, in fact, the spatial power spectrum of the pupil function, the intensity of pixels in the image may be thought of as power at the corresponding spatial frequencies. The low frequency cutoff in the pupil plane relates to the smallest resolvable sizes in the image plane. Our choice of the 2:1 ratio of array size to aperture defines the peak to first null size of the "diffraction limited" (flat pupil wavefront) spot produced by the simulated telescope to be two pixels.

Referring to Figure 21, we may follow the numerical simulation, through one update cycle. It begins by defining the pupil function. For ease of representation and computational convenience, we have chosen to decompose the pupil function into Zernike components. This allows us to completely specify the pupil function using a very limited amount of storage space. Once again, because of the coarseness of the input digitization, we include only Zernike modes of the first three orders. Written out in cartesian coordinates there are nine polynomials. Their representations and their related optical aberrations are given in Table I. There is a problem associated with this choice of representation. The Zernike polynomials are orthogonal on the unit circle and not over the unit square aperture used in this simulation. This leads to crosstalk between the various modes. However, since only a single mode is dithered at any given moment in this simulation, we do not have a problem separating the effects of the modes. For the real-time system, it would be necessary to utilize a different decomposition of the pupil function that is orthogonal over the aperture of the



MODS NUMERICAL SIMULATION CODE

Figure 21. Schematic representation of numerical simulation code. Program names are indicated in shaded boxes. Refer to Appendix for code listing.

Three components must be included in the pupil function. First is the aberration. This is input into the program as a set of Zernike polynomial coefficients. Next, the vector of corrector element updates from the last loop is applied. These are again represented as Zernike coefficients and are summed with the input aberration. Finally, the modal dithering is applied. This is another area where the numerical simulation differs from the proposed real-time system. Rather than frequency multiplexing the different dither modes, each mode is dithered sequentially. This was done because in the digital simulation to properly represent N modes in temporal frequency space would have required 2^N calculations of the image plane intensity distribution, whereas the sequential dithering requires only $2N$ such calculations per update. Thus, the update cycle begins by dithering the lowest order mode first plus the dither amplitude, then minus the same amount, then proceeds to dither each subsequent mode in the same way.

After all three phase components are summed, the complex pupil function is calculated. The Zernike polynomials are defined such that they range from +1 to -1 over the unit circle. On the square aperture they cover a larger range. Nevertheless, the pupil function has been defined such that the range +1 to -1 in Zernike value corresponds to $+\pi$ to $-\pi$ in phase.

The simulation was run with two different input unaberrated wavefronts. Initially, a plane wave was input by setting the pupil function equal to $1+0i$ at all points, in the absence of any phase aberration. In the second phase of testing, a source consisting of two points of variable separation and position angle was used. This was realized in the simulation by applying an amplitude modulation to the pupil function. This allows the definition of extended objects independent of the phase aberration.

Once the pupil function is defined on the 64×64 array, a two dimensional FFT is performed. The result of this operation is the image plane function related to the given pupil function. The

squared modulus of this function yields the image intensity distribution. This result is contained in the same 64x64 array used to input the pupil function. A 32x32 sub-section of this array, centered around the "optical axis" (defined by the location of the zero spatial frequency component) is extracted and is used for the further processing. Because of the scaling of the image plane (two pixels being equal to an angular displacement of λ/D), and the desire that the image segment be

TABLE I
CARTESIAN REPRESENTATION OF ZERNIKE POLYNOMIALS

Order	Expression	Name of Aberration
1	X	Tip
	Y	Tilt
2	$2(X^2+Y^2)-1$	Defocus
	X^2-Y^2	Astigmatism & Curvature of Field
	$2XY$	
3	$3X^3+3XY^2-2X$	X-Coma
	$3Y^3+3YX^2-2Y$	Y-Coma
	X^3-3XY^2	
	$3YX^2-Y^3$	

smaller in size than an isoplanatic patch, we may say that this

simulation applies roughly to a telescope that provides 16 diffraction limited resolution elements within a typical isoplanatic patch. For daytime conditions, this is equivalent to a clear aperture of about 0.6m and an image segment of about 3 arc-seconds width. It should be remembered that this part of the simulation is not part of the real-time system. That is, the telescope will perform the Fourier transforms at no computational cost.

Once the image segment is defined, calculation of the error signal may proceed. First, it is necessary to construct the power spectrum of the intensity distribution. As was mentioned above, it was decided not to utilize a true 2-D FFT routine here, but rather to split the operation into many parallel 1-D FFTs. Ordinarily, a 2-D FFT is computed by doing 1-D FFTs in one direction, writing the result back into the input array, and doing the FFTs in the other direction. The only difference here is that the result is not written back. This does not gain us any speed in the simulation because the Nova is not capable of parallel processing. However, in the real-time system, a considerable savings in time may be obtained. The calculation of this power spectrum is the bottleneck in the processing of the servo loop and trimming time from that step is quite important. In the simulation, as each FFT is done, its result is summed into a one dimensional array that, finally, contains the desired function that is in some sense the power spectrum of the image. Since we do not perform the true 2-D transform, but rather a one dimensional calculation, the resulting pseudo-power spectrum has reduced sensitivity to spatial variations in the image that are at an angle to the coordinate axes.

The pseudo-power spectrum is then normalized so that the power in the zero-frequency bin is set to unity. This vector is then integrated over the range of spatial frequencies from DC to the diffraction limit of the imager and the result stored. The process is then repeated from the point of the definition of the phase function. The sign of the dither of the selected mode is changed

and a new pseudo-power spectrum integral (PPSI) is calculated. The difference of these two PPSIs gives two pieces of information that are used to update the phase correction. First, the size of this quantity indicates the sensitivity of the image quality to variations in the chosen mode. This allows the introduction of thresholding into the servo loop in the sense that modes that produce almost no variation in image quality will not be updated at all preventing spurious wandering of the correction values. Second, the sign of the PPSI difference gives also the sign of the correction to be applied to the dithered mode. If the size of the PPSI increases when the coefficient of the Zernike mode is increased, that implies that the correction to be applied to that mode must be positive.

The foregoing process is repeated for all Zernike modes, that is, seven pairs of positive and negative dithers. Once this cycle is complete, the resulting PPSI differences for each mode are examined. For those that exceed a predetermined threshold, a correction update is calculated. The sign of the correction is known from the sign of the PPSI difference. The size of the correction is based on the absolute value of the PPSI of the input, aberrated wavefront image. That value is differenced from the theoretical best performance PPSI for the imager to yield a quantity that must be minimized in order to perfectly sharpen the image. The size of this quantity is used to modify the size of the correction step as the image approaches the ideal. In the simulation, the size of the correction step, the PPSI difference threshold and the size of the dither amplitude were all tied to the value of this absolute image quality measure. Their connection, however, was not in a continuous fashion, but rather as the size of the difference of the PPSI from the ideal passed various levels, the sizes of these quantities were all changed by fixed multiplicative factors. It was found that using only a two phase system, that is implementing only one change in the size of the correction step, etc., gave adequate

performance.

After the correction updates were all calculated, the entire process was begun again. In addition to the steps outlined above, a routine was added to the loop that presented a visual display of the image at every correction update. Running on a Nova with hardware floating point, the real elapsed time for one update was about 55 minutes.

IV. RESULTS OF THE MODS SIMULATION

4.1 TESTS OF SIMULATION CODE

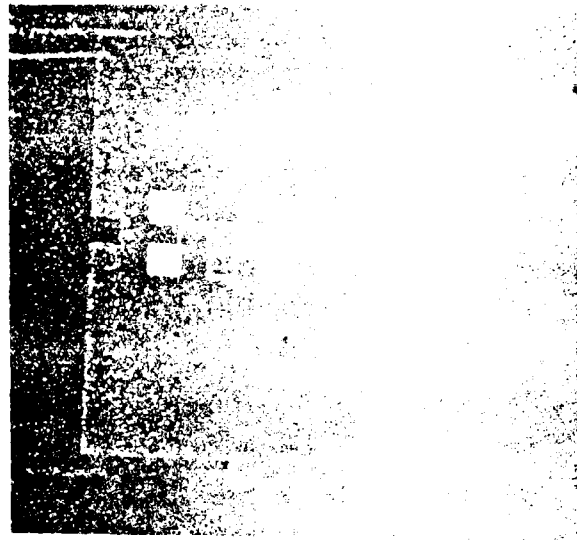
Once the simulation code had been brought to an operating condition, it was necessary to test its physical correctness by attempting to simulate a number of imaging situations with known results. The first of these was the simple imaging of point source. An unaberrated plane wave was input into the imaging simulator and the resulting image plane intensity distribution examined. This image is depicted in Figure 22. The image produced by an ideal square aperture is given by the product of two sinc functions, one in each dimension. The spacing of maxima and minima, and the intensity as a function of position are all very readily calculated. By examining the numerical values of intensity produced by the simulation, it was possible to determine the extent of numerical error introduced by the calculation. The quantities tested were the position and intensity of the image maximum, the total power in the image, and the separation of minima. All of these quantities were within 0.7% of the values predicted by theory, indicating that roundoff errors are not a problem in this calculation.

Next, tilt was introduced into the wavefront by altering the first Zernike coefficient. The size of the tilt was set to one wave over the full aperture in X and two waves in Y. The resulting image is shown in Figure 22. The displacement of the blur spot is exactly the predicted two pixels. A combination of tilt and tip with different values for each was then tried, and again the result confirmed that the image simulation was operating correctly.

The next tests were aimed at checking the performance of the PPSI calculation. For the unaberrated image, the PPSI value agreed with theory at the 1.2% level. Further, the introduction of tip or tilt to the wavefront did not alter the PPSI value significantly.

By introducing various amounts of other aberrations into the

unperturbed image plane distribution for point source input. Field of view is $\sim 3^\circ$. Intensity is coded by random color sequence and is represented logarithmically. This is the 2-D sinc function.



Introduction of 1 λ tilt and 2 λ tilt into unperturbed input. Image shifts 2 and 4 pixels in x and y , respectively.

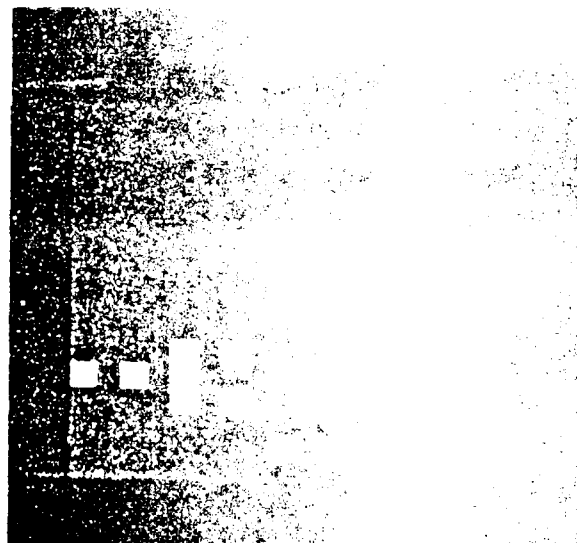


Figure 2

input wavefront it was possible to determine the sensitivity of the error signal algorithm to wavefront distortions. It was found that, very roughly, the decrease in the PPSI value for a given aberration was dependent only on the size of that aberration and not on its form. There were differences in sensitivity of the order of a factor of two between certain modes probably due to the way the PPSI is calculated via 1-D FFTs. One important finding of this phase of the testing was the discovery that the presence of any large aberration obscures the effects of other aberrations. This may be understood if one considers the shape of the MTF as a function of aberration strength. As the aberration is increased, the high frequencies are very rapidly depressed. If further aberrations are added, they have only a minimal effect on the MTF since it is already reduced to nearly zero at the higher frequencies and they act in a multiplicative way on the MTF. This effect leads to the unfortunate property that the PPSI increases in sensitivity to image quality as one approaches the unaberrated case. This means that extreme care must be taken in adjusting loop gains and step sizes if instability is to be avoided. In addition, it leads to a problem if one attempts to update all the correction Zernike coefficients at one time. If we consider a case in which, say, there are several waves of defocus combined with smaller amounts of other aberrations, dithering one of the minor aberrations will not produce a significant effect on the PPSI and thus the correction derived will not have meaning. It was this effect that lead to the inclusion of the thresholding in the calculation of the correction update. If a given mode has only a very small effect on the PPSI its correction coefficient is left unchanged. For some choices of threshold, this produces a situation in which initially, while there are large aberrations present, only the one or two most important are updated. As these aberrations are reduced, the PPSI becomes more sensitive to the other modes and more complete updating may be started. Figures 23 through 27 show typical image plane distributions for various aberrations.

Figure 23. Image distribution
with $.65\lambda$ defocus.

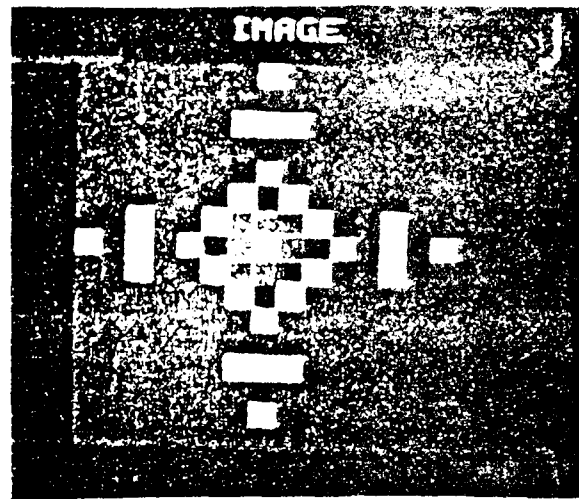


Figure 24. Image distribution
with $.58\lambda$ astigmatism
and curvature of field.

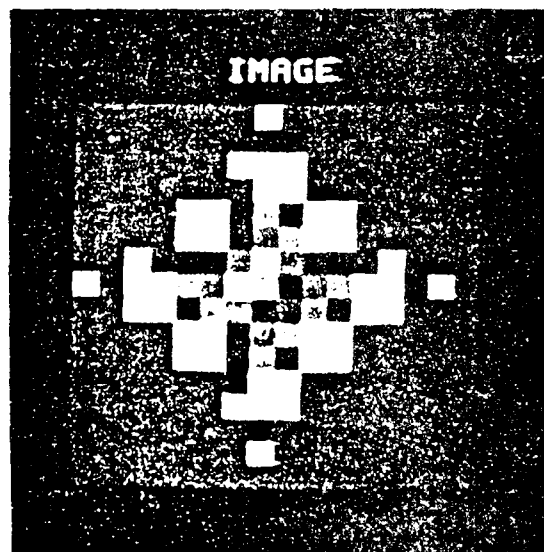


Figure 25. Image distribution with $.66\lambda$ astigmatism and curvature of field.

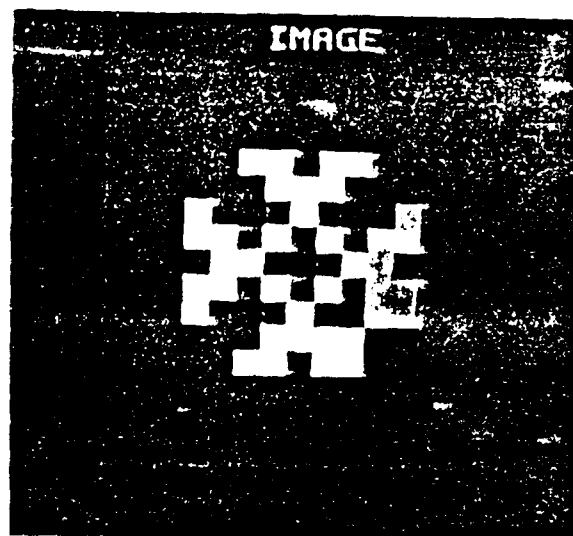


Figure 26. Image distribution with all three 2nd order Zernike modes. Total aberration $\sim 2\lambda$.

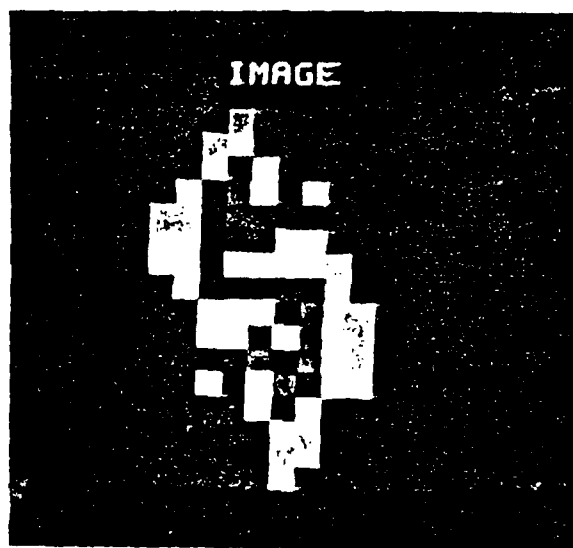
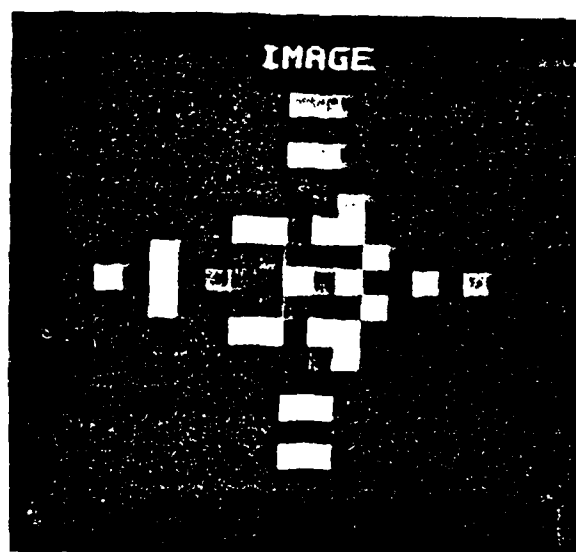


Figure 27. Image distribution
with $.7\lambda$ coma in X
direction.



4.2 TESTS OF THE LOOP SIMULATION

Once being assured that the PPSI error signal was indeed a useful indicator of image quality, testing of the complete image sharpening system could proceed. It is routine DITHER that actually implements the correction update procedure. It is the routine that controls the program flow, keeps track of the values of the error signals and of the Zernike coefficients. It is in DITHER also that the value of the error signal thresholds and the effective loop gains are set.

Specifically, after the calculation of the differential PPSIs resulting from the dithering of each mode, they are each compared with their respective thresholds and for those that exceed the threshold value, a sign is recorded. Then the value of the PPSI for the present, undithered wavefront is computed and this number is subtracted from the ideal PPSI value. This difference is multiplied by a gain factor to yield a quantity which, when combined with the present correction step size in various ways, yields the correction update. It is also used to alter the values of the other parameters. Thus, there are three vectors of length equal to the number of modes being updated and two scalars that may be adjusted in attempting to achieve stable convergence in the update loop. These are: (vectors) the dither amplitudes, the PPSI thresholds, and the correction step size; (scalars) the ideal PPSI value and the gain factor.

Many combinations of these parameters were tested in the full update loop and several successful systems were identified. By no means was the whole parameter space examined because of the large amount of time occupied in running the simulation for each choice of parameter values.

In its initial form, the dither amplitudes and threshold values were not changed from their input values. Only the correction step size was a function of the size of the difference of the PPSI from ideal.

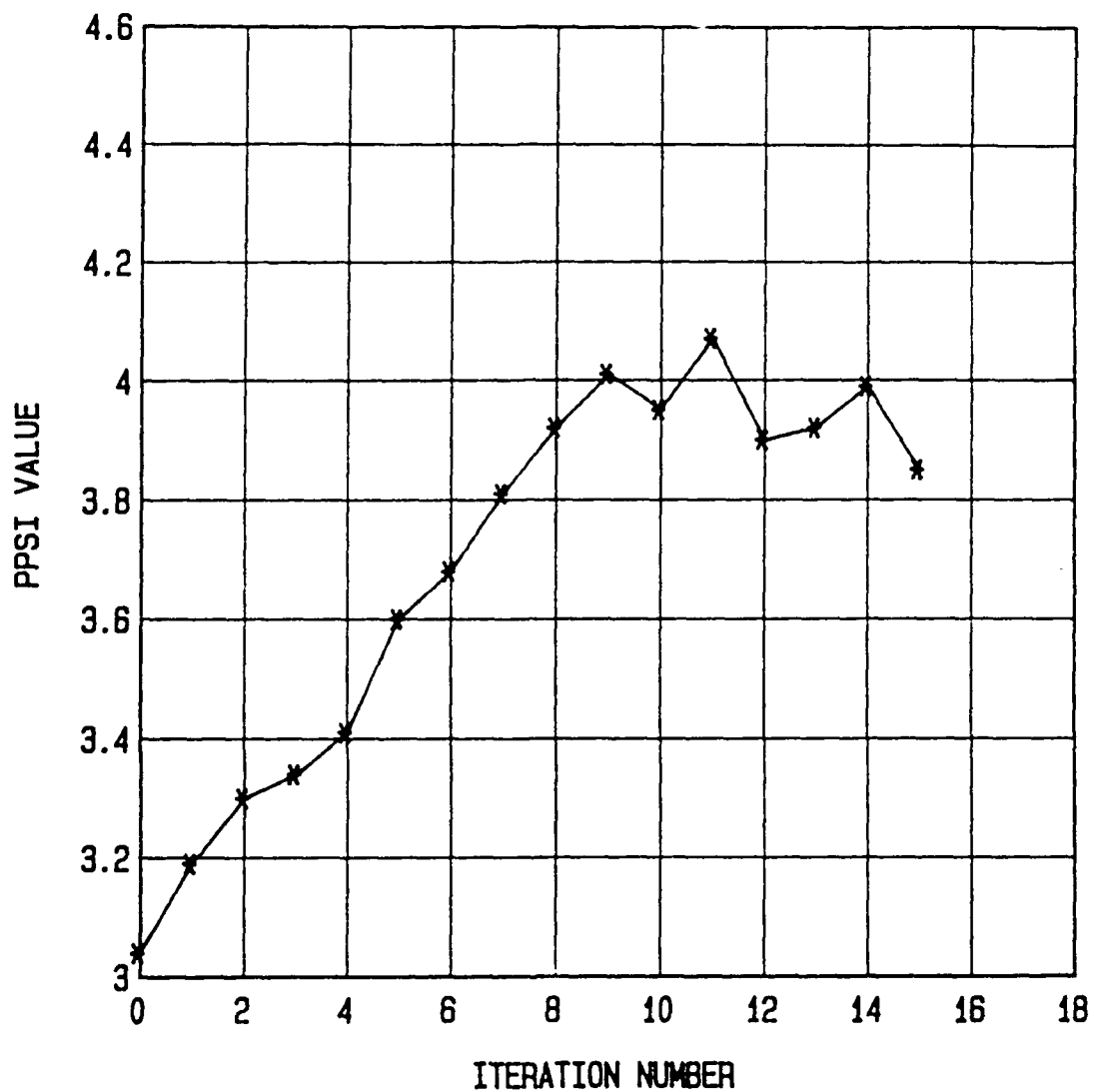
A typical test of the system would begin with an aberrated wavefront defined by a set of input Zernike coefficients. Total peak-to-peak aberration in these wavefronts ranged from one wave to about six waves in the worst cases. Six waves of aberration is roughly equivalent to a seeing disc of one arc-second for the 0.6m telescope. Unfortunately, this is somewhat smaller than the typical daytime condition seeing that we would like to correct. However, as previously mentioned, due to the discrete sampling of the pupil plane we cannot represent larger aberrations correctly. Indeed, six-wave aberration must be in the lowest modes in order to prevent anomalous behavior.

After adjustment of the parameters, it was shown that stable convergence could be achieved for a range of input aberrations. Typically, the value of the PPSI would rapidly approach the ideal value taking only three to five iterations to reduce the value of the p-p aberration from four to six waves down to less than one wave. It was found that once the aberrations have reached this level, both the dither amplitude and the correction step size were too large. The modes being updated would step on either side of ideal and the PPSI would cease to improve. This behavior is shown in Figures 28 and 29, which is a plot of the PPSI values and the corresponding aberration amplitude for a typical run.

A significant improvement in the system performance was achieved by implementing the update of the dither amplitude, step size, and threshold level on the basis of the current value of the PPSI. Once the PPSI went above a preset level, the sizes of all of these parameters were multiplied by constants less than unity. The values of these constants were chosen on the basis of experiment and once again are the result of a very limited search of the parameter space.

In the final form, the simulation was able, for most input aberrations, to achieve convergence to within 0.25 waves p-p after 10 to 15 iterations. Further, the simulation showed itself to be stable in that it could run for 50 iterations without wandering more

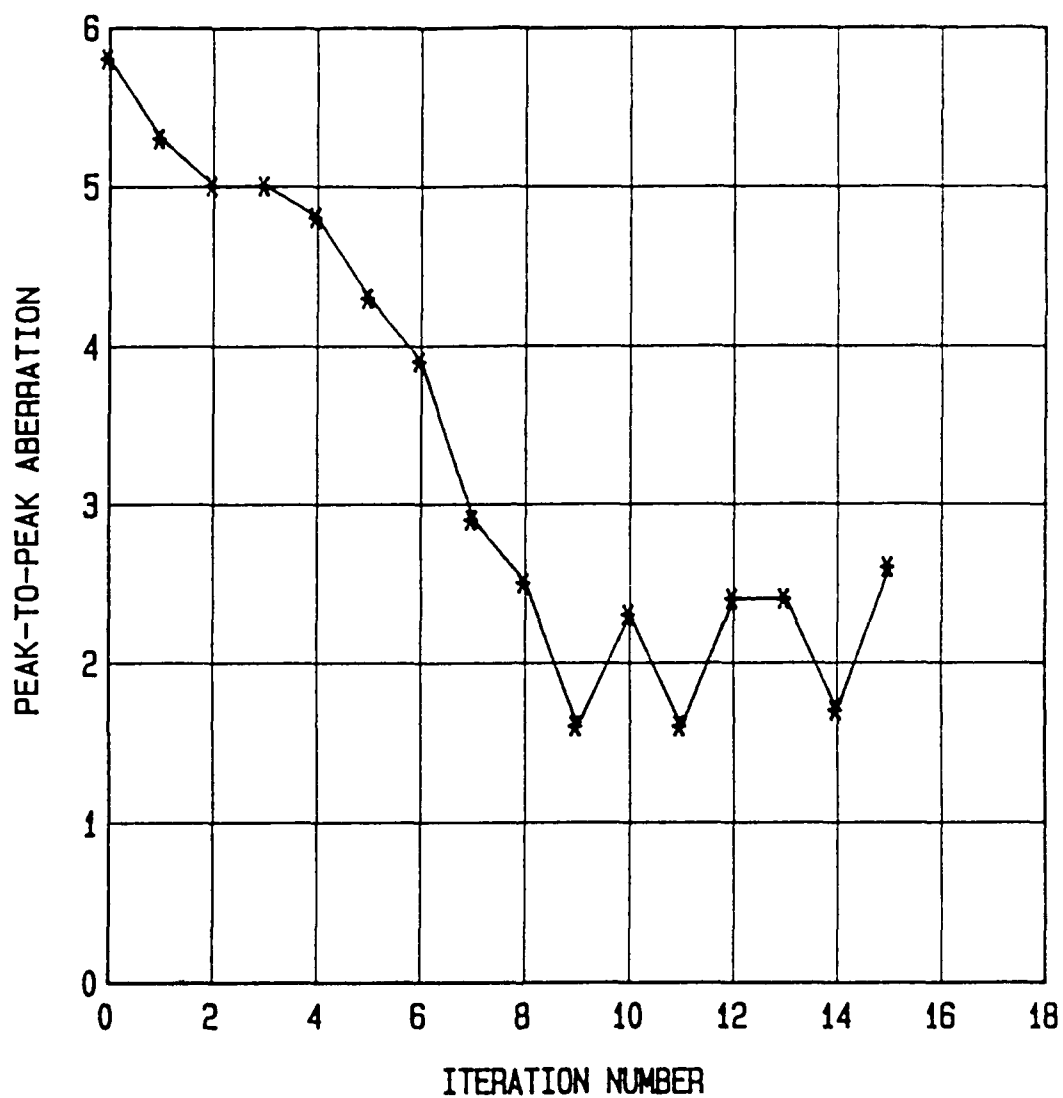
POINT SOURCE



ONE STEP ALGORITHM

Figure 28. Plot of the value of the pseudo-power spectrum integral error signal as a function of iteration number using the one-step algorithm. At the 9th iteration, algorithm goes into oscillation. Ideal value for PPSI is 4.35.

POINT SOURCE



ONE STEP ALGORITHM

Figure 29. Plot of the peak-to-peak aberration as a function of iteration number for same runs as Figure 28.

than 0.15 waves from its best solution. In terms of seeing disk size, this is equivalent to a reduction from about 1 arc-second to 0.18 arc-second, just 4% above diffraction limited performance. Figures 30 and 31 show the convergence of the PPSI and of the p-p aberration. Figures 32 through 37 give the image plane distribution at various points along the run.

4.3 PERFORMANCE ON IMAGING EXTENDED OBJECTS

Since the application of the MODS system would be for imaging of the solar surface, testing of its performance on extended objects was of primary importance. The realization of an image plane filling source is difficult in the finite digitization of the pupil plane, so instead, simulated double stars were utilized in this testing. The separation and position angle of the stars can be specified by applying a modulation to the amplitude of the pupil function. This modulation is independent of the phase aberration and is very easily added to the existing code. Double stars of various separations aligned along one of the coordinate axes were used as input objects. The input parameter values required some adjustment to achieve convergence in these tests. Further, it was found that the MODS system lacked sensitivity to certain aberrations for the special case of alignment along an axis. Any aberration that leads to a spreading of the image along the line connecting the stars was not corrected for as well as those perpendicular to that axis. This was confirmed by changing the position angle of the stars but using the same initial aberration. For angles other than those of lines of symmetry of any of the modes, the convergence was satisfactory. Figures 38 through 41 show the PPSI values and peak-to-peak aberrations for two runs using double point sources. For the second run, the position angle was rotated through an angle of $36^{\circ} 87$. Figures 42 through 48 show the image plane distributions at several points during these runs. Overall, the performance of the system was similar to that for point sources, although the final image quality was marginally worse. The average p-p wavefront error

in the final state of several runs was 0.32 waves. Once again, this is very close to diffraction limited performance.

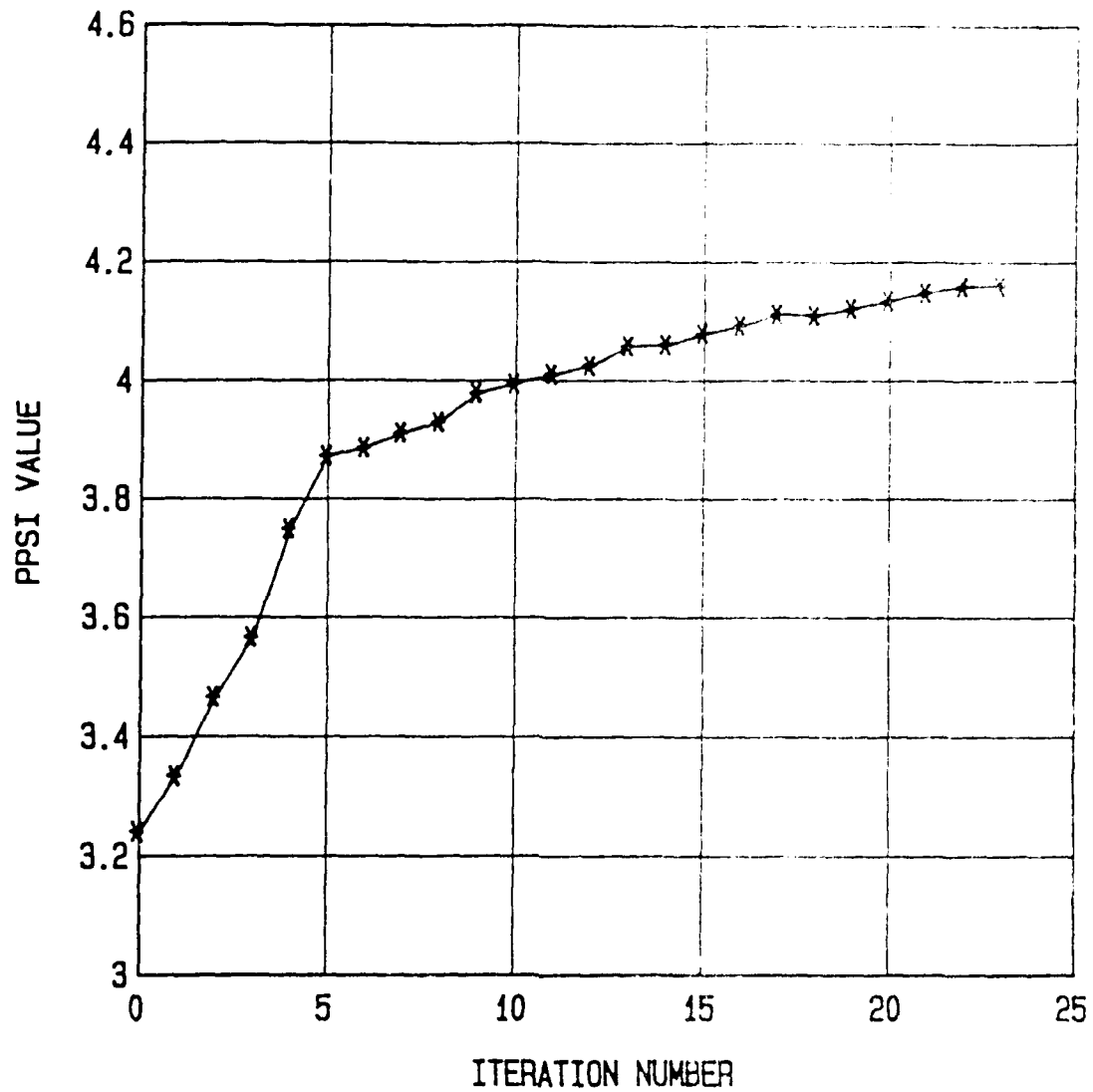
Theoretically, the performance of MODS should be independent of the source, since the entire effect of an extended source may be represented by the multiplication of the diffraction limited MTF of the imager with the spatial power spectrum of the source. This operation does not affect the relative sensitivity of the PPSI to wavefront distortions. However, this is not the case for the real-time system because of the presence of noise in the system. It is likely that the observed reduction in simulated system performance on extended objects is due to the increased importance of numerical errors relative to the size of the error signals. This makes clear the need for very high signal-to-noise imaging in the real-time system.

4.4 SUMMARY

In conclusion, we may say that the MODS system simulation shows that it is possible to achieve significant image improvement under conditions of moderate atmospheric turbulence. We have shown that the system converges to the desired wavefront correction from a fairly wide range of input aberrations. Further, this convergence is rapid and stable. It is quite likely that further testing of MODS would identify better choices for the loop parameters that would lead to improvements in performance.

For the simulated 0.6m telescope, we have shown that MODS will improve the image plane resolution by a factor of more than five under conditions of 1+ arc-second seeing. This improvement is achieved in less than 15 update cycles. We have also shown that MODS will form as well on extended objects, provided there is sufficient signal-to-noise in the detected image.

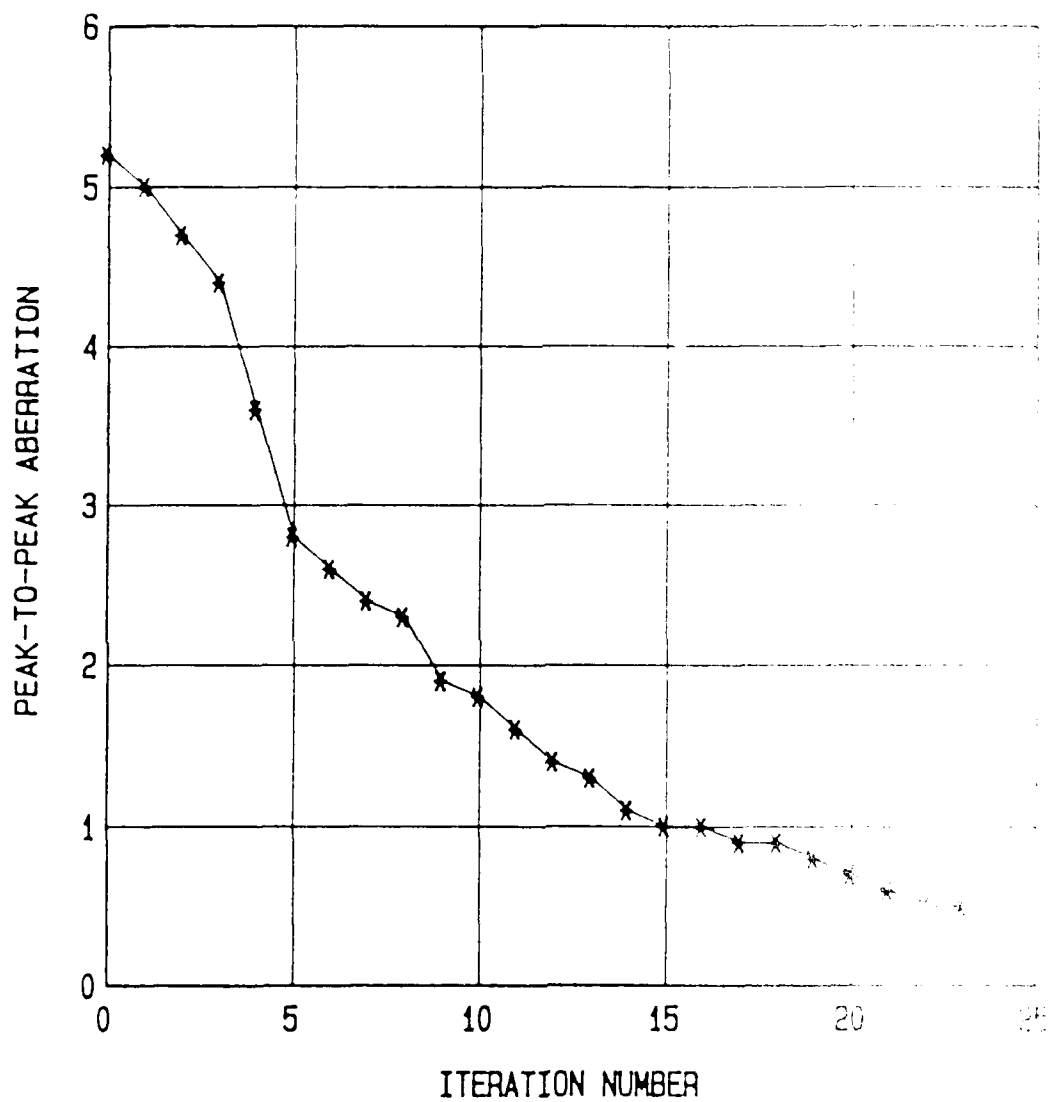
POINT SOURCE



TWO STEP ALGORITHM

Figure 30. Plot of PPSI value vs. iteration number for two-step algorithm.

POINT SOURCE



TWO STEP ALGORITHM

Figure 31. Plot of p-p aberration for same run as Figure 30.

Figure 32. Input aberrated image of
run shown in Figure 23.
Total p-p aberration of
26. (scaling of inten-
sity different from
previous figures).



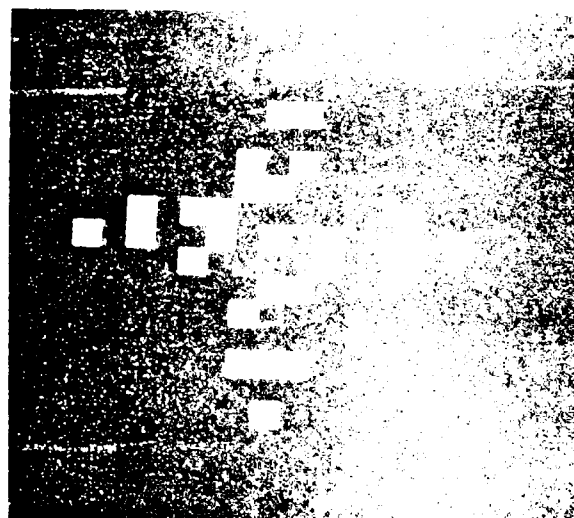
Figure 33. Iteration #1.



Figure 34. Iteration #2.



Figure 35. Iteration #3.



AD-A155 434

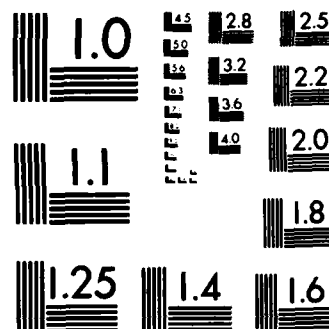
SOLAR ADAPTIVE OPTICS(U) ADAPTIVE OPTICS ASSOCIATES INC 2/2
CAMBRIDGE MA A WIRTH ET AL. SEP 84 AFGL-TR-84-0262
F19628-82-C-0035

UNCLASSIFIED

F/G 3/1

NL





MICROCOPY RESOLUTION TEST CHART
NATIONAL BUREAU OF STANDARDS-1963-A

Figure 36. Iteration #4.

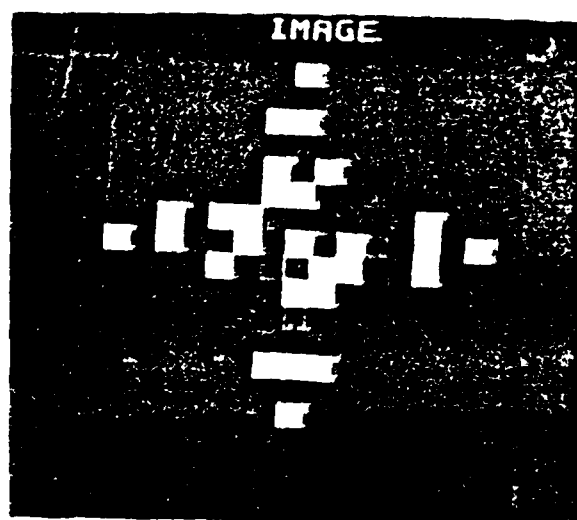
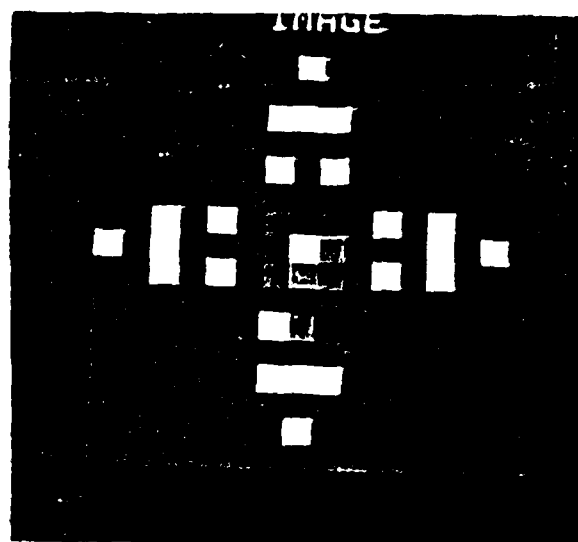


Figure 37. Iteration #20.



EXTENDED SOURCE

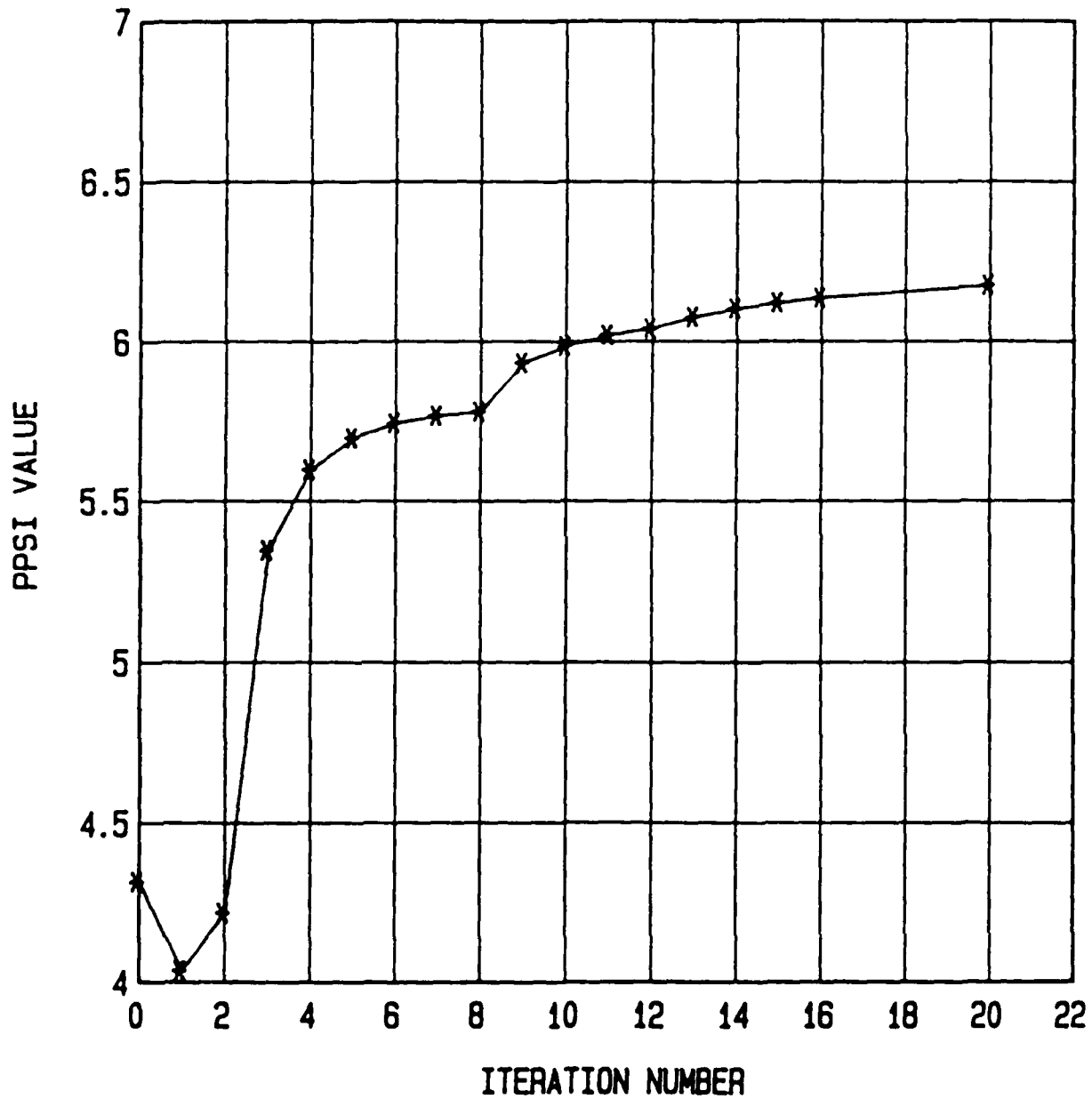


Figure 38. PPSI value for double source aligned with Y axis.

EXTENDED SOURCE

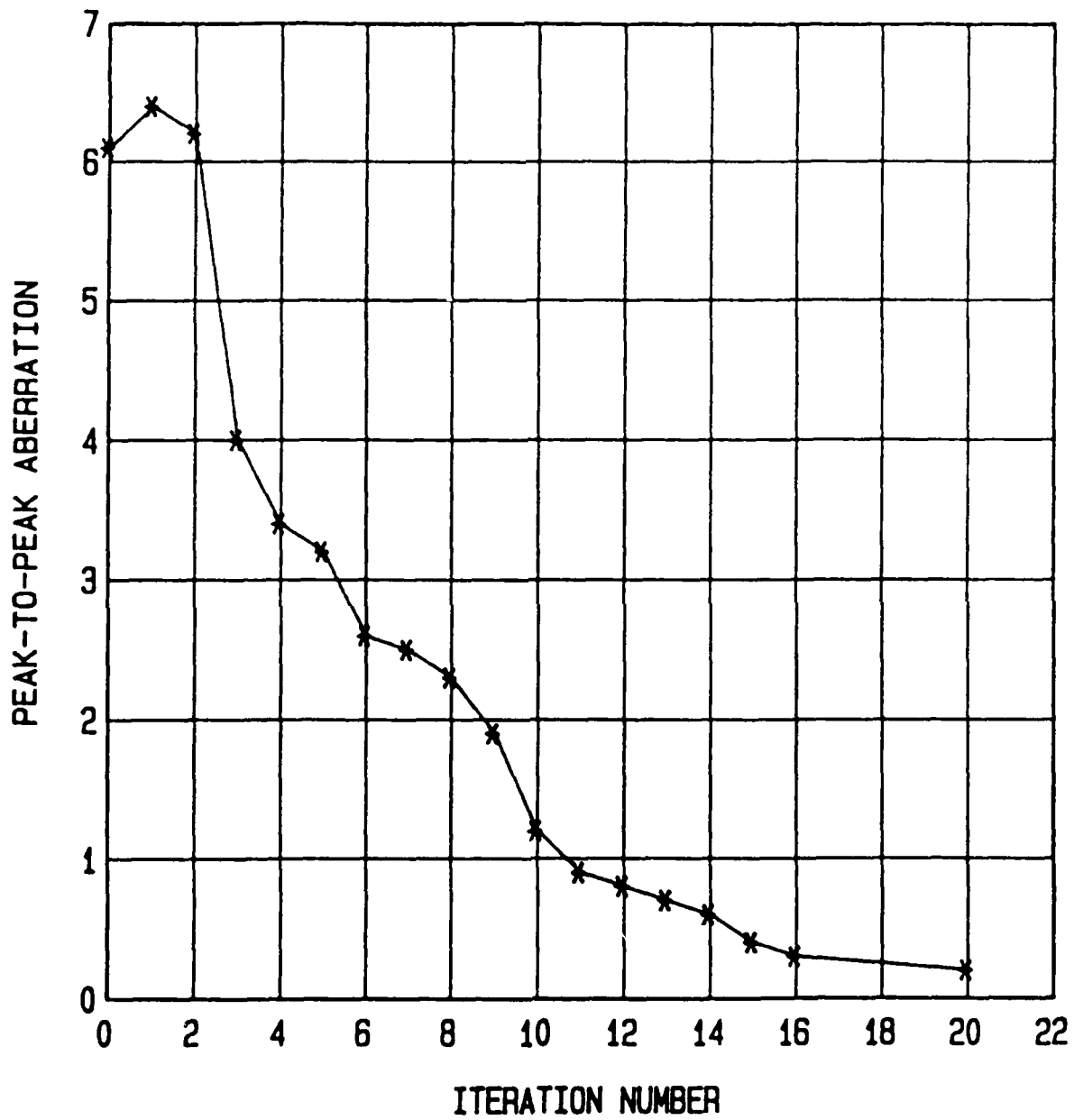


Figure 39. p-p aberration for run of Figure 38

EXTENDED SOURCE

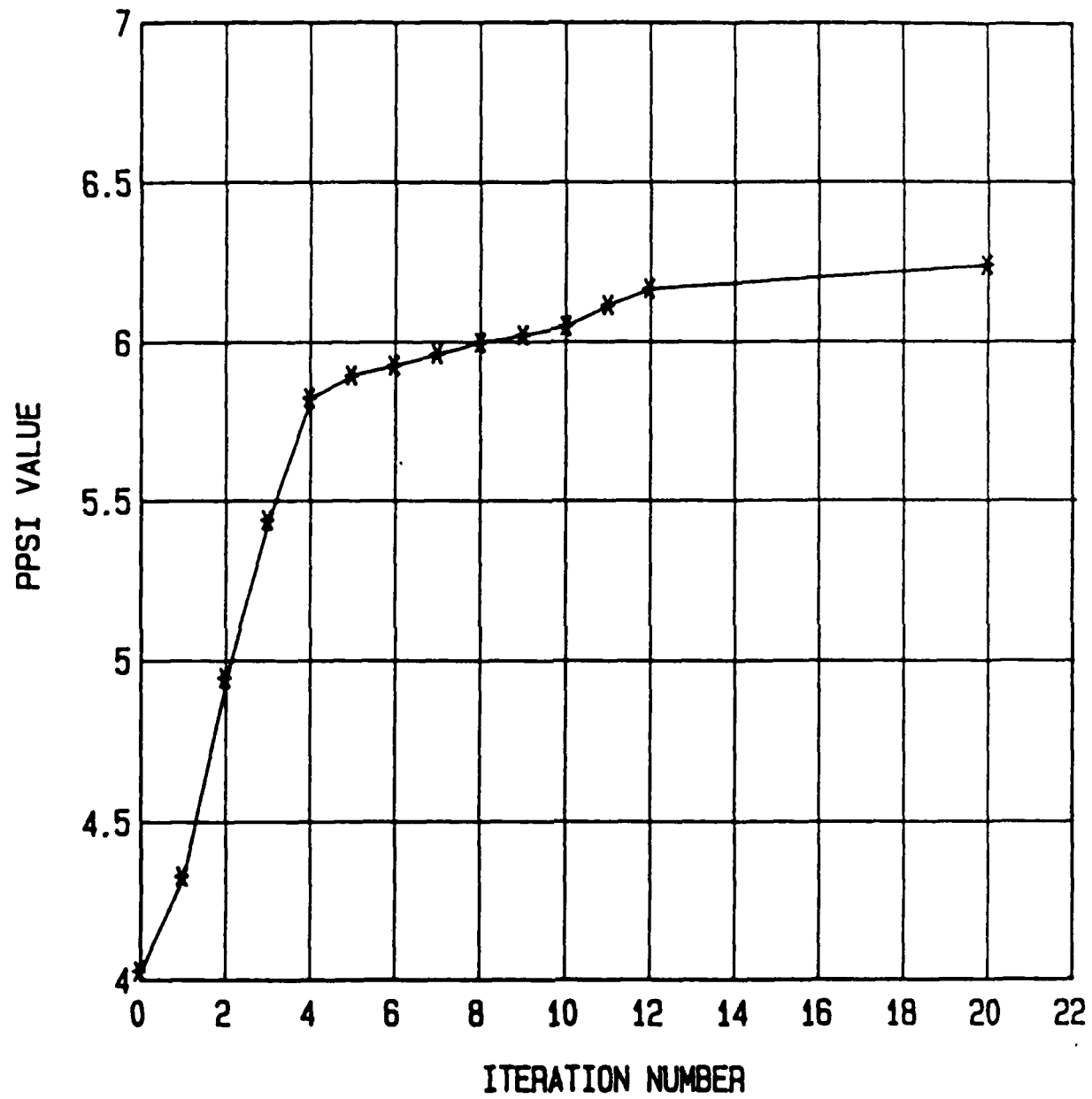


Figure 40. PPSI values for double star at an angle of 37° with Y axis.

EXTENDED SOURCE

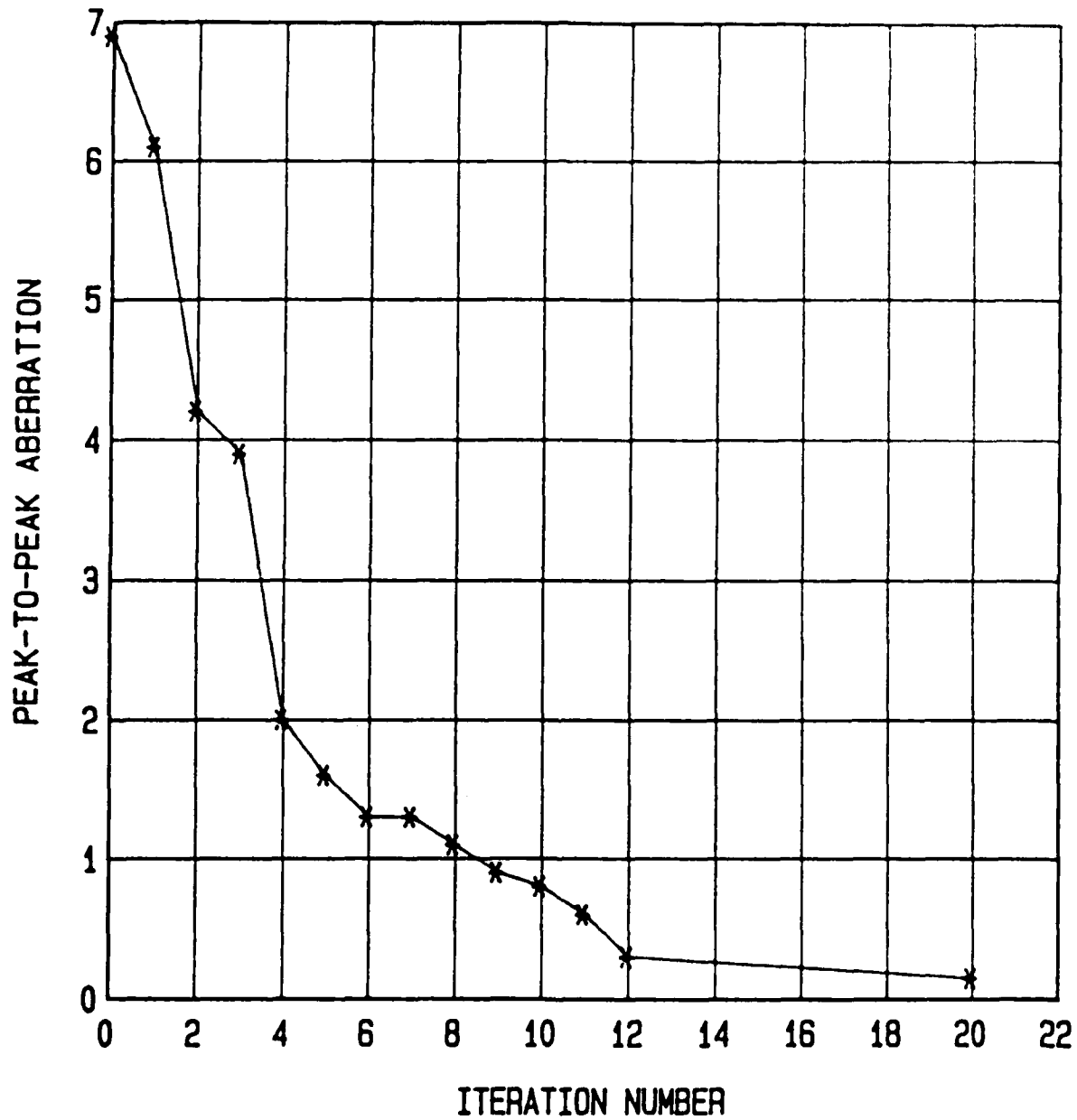


Figure 41. Corresponding p-p aberration values.

Figure 42. Unaberrated input for run of Fig. 38. Separation is 2λ or ~ 0.6 .

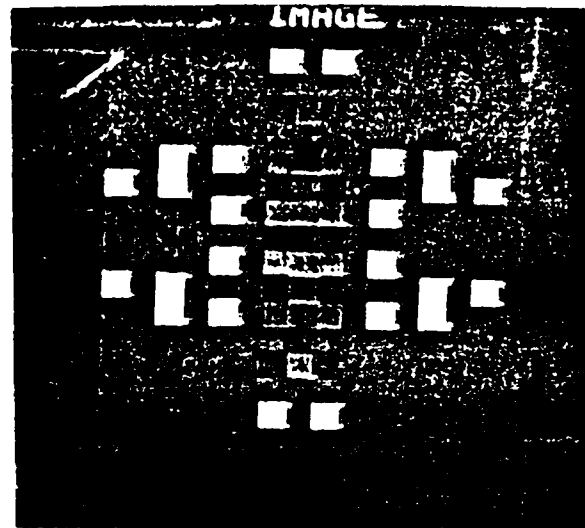


Figure 43. Starting aberrated image p-p aberration $\sim 6\lambda$.

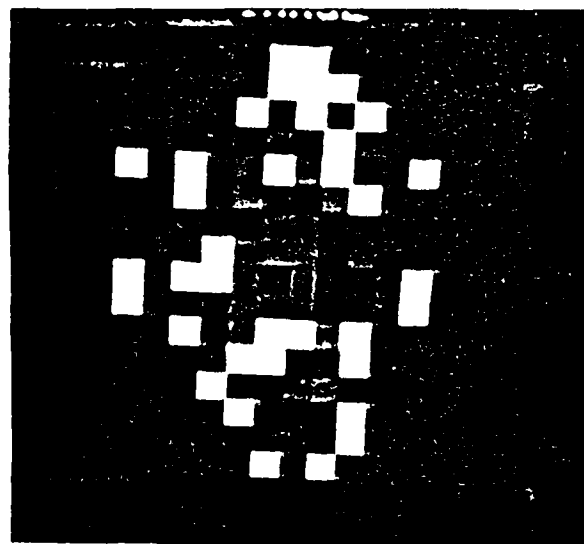


Figure 44. Iteration #3.

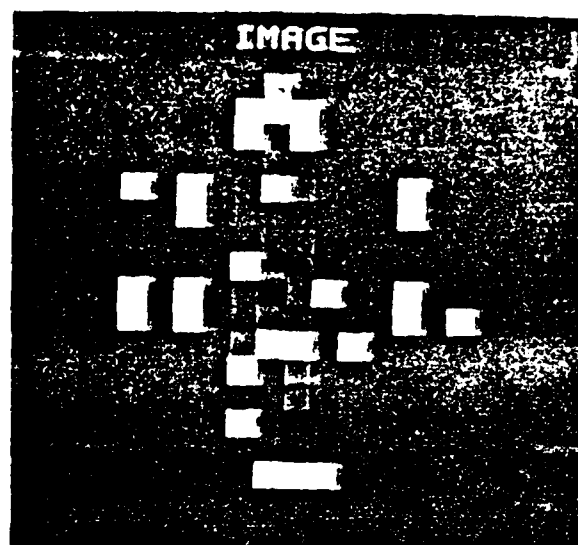


Figure 45. Iteration #17.

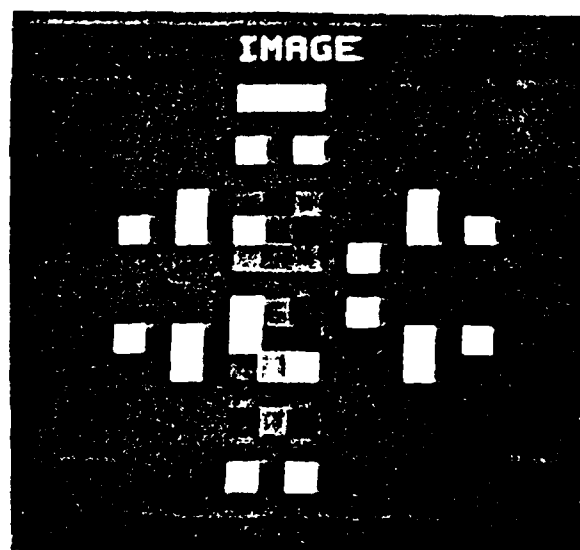


Figure 46. Unaberrated input for
run of Figure 40.
Separation of 2.5λ on
 $0''.75$, position angle
 $36^\circ 8$.

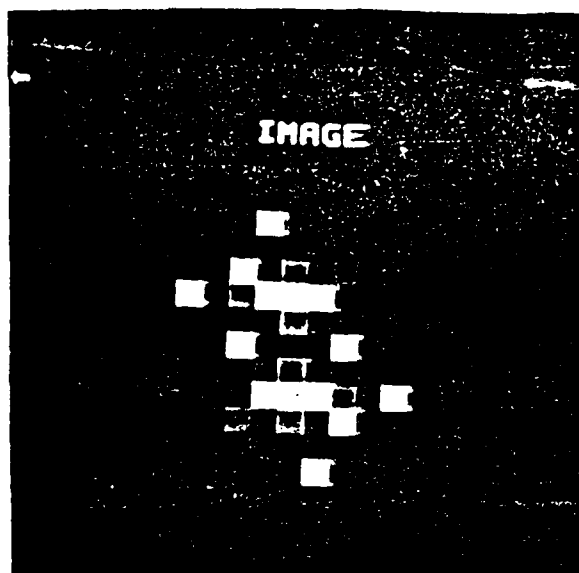


Figure 47. Input aberrated image.

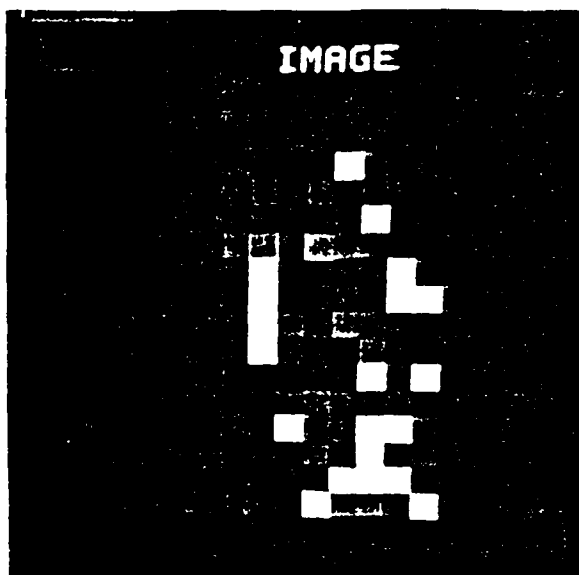
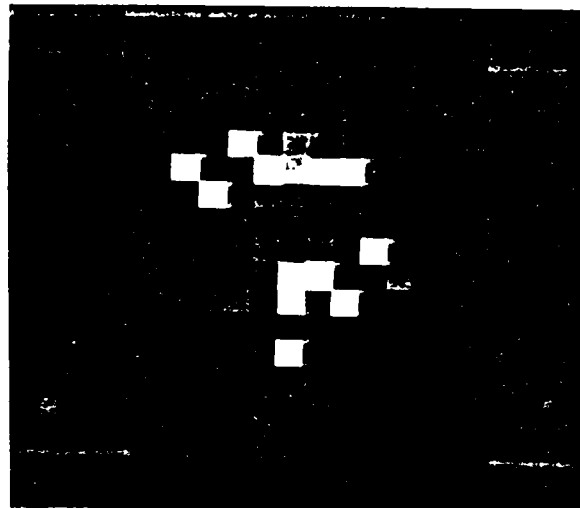


Figure 48. Final image,
Iteration #20.



V. CONCLUSIONS

5.1 DESCRIPTION OF SOLAR ADAPTIVE OPTICS PROJECT

This project has broken into two well defined parts. In the first, a theoretical study of the application of traditional adaptive optic techniques to the problem of daytime imaging of extended sources, it was shown that any wavefront correction scheme that relies upon subapertures of a size comparable to the isoplanatic patch size will fail under typical conditions. This explains why all attempts at solar imaging with adaptive optic correction have not performed as well as might have been hoped. Faced with this serious limitation of subaperture based systems, a second part of this project was defined that sought a full aperture wavefront correction method that would operate with extended sources. Such a technique was defined and a numerical simulation constructed to test the feasibility to the system. This system, termed MODS for Modal Dithering image Sharpener, was shown to perform successfully in this simulation. As the name implies, MODS is related to the multidither technique of image sharpening. No wavefront sensing is done; rather hill climbing servo loops are used to maximize image sharpness by applying corrections to a Zernike modal decomposition of the pupil wavefront. Tests of the MODS simulation show that it is possible to obtain a fivefold improvement in resolution in a small number of loop updates. The MODS system thus shows promise for extended object imaging under conditions of moderate atmospheric turbulence.

5.2 REAL TIME MODS OPERATION

Based upon the performance of the numerical simulation of MODS, we may conclude that it may represent a practical way to approach the problem of high resolution solar imaging. The question then becomes whether or not it is implement MODS in a real time system.

The essential problem is calculating the PPSI error signal rapidly enough to update the corrector on atmospheric variation timescales. This requires that the typical convergence time, for all modes corrected, be on the order of one millisecond. Current technology limits the framing speed of a 32x32 detector to roughly 50 kHz. Assuming that the quantum efficiency of the detector is approximately 50%, photon statistics limit the signal-to-noise, to ≈ 70 for a 1 \AA passband. It must be remembered though that the PPSI is, in a sense, a sum of the intensity in the whole picture. Thus the S/N of the PPSI is higher than that of a single pixel. If frequency multiplexing of the dither modes is used, the highest frequency allowed will be set by the requirement that the PPSI be well sampled over a single cycle. If we take the upper frequency to be, say, 12 kHz, we could dither about seven modes at 1.5 kHz spacing. The first seven Zernike modes include all the second and third order aberrations and represent more than 90% of the aberration power in atmospheric turbulence⁽²⁷⁾. The frequency of the lowest mode would be 32 kHz, still above the atmospheric timescale.

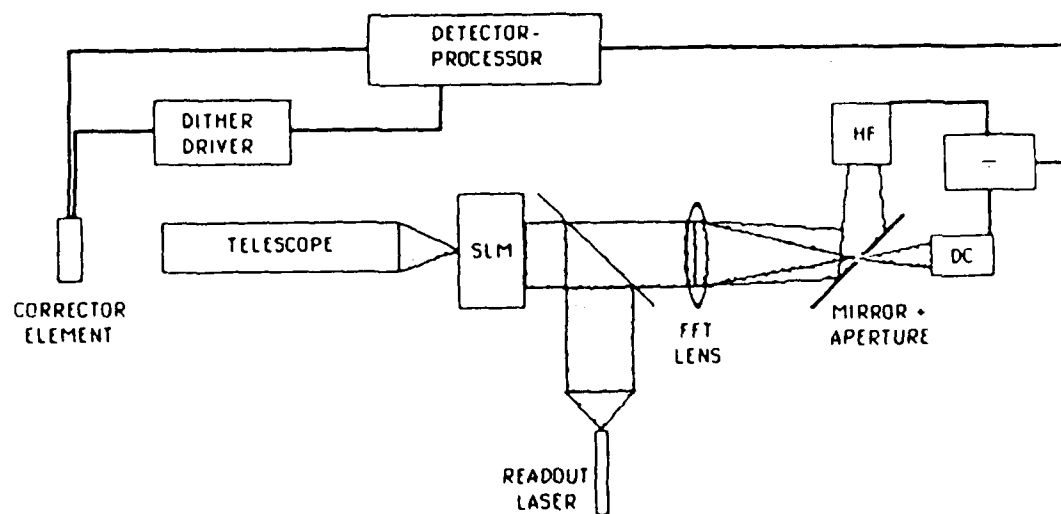
The major processing need then is the ability to compute the PPSI at a 50 kHz sustained rate. This means that we require a 32 point FFT result to be calculated in less than 20 μs . This may easily be achieved with a microcoded processor with the option of expandability to larger vector sizes. If dedicated hardware is used, the time for a 32 point FFT may be reduced to the 1 to 2 μs range. By utilizing 32 or 64 of these processors in parallel, the PPSI may be calculated in the requisite time. An alternate processing technique that should be explored is the use of directed optical processing to calculate the PPSI. There are available optically driven Spatial Light Modulators (SLM). Such

⁽²⁷⁾ Tyler, G.A. Tech. Rep. BC223; The Optical Sciences Co., Feb. 1984

a device would be well suited to this application, provided it could be framed at a high enough rate. There are currently under development devices that will perform at close to 1 kHz, not quite fast enough for this application since we require several PPSI calculations per update cycle. There is, however, a tradeoff between resolution and speed and since our application is low resolution, we may be able to gain the required speed without requiring great advances in present technology. Ideally, the device would not be framed at all, but used in an integrating mode with a time constant, set by the resistivity of the crystal, of about 30 μ s. This would allow the system to run continuously with synchronous analogue detection of the error signal for each frequency.

Figure 49 is a schematic representation of a system using the MODS algorithm, but doing a significant part of the processing with a Spatial Light Modulator. After passing the collimated input beam through both the correcting element and the ditherer (shown as one in the figure), the light is imaged onto the cathode of the SLM. This generates an identical image in the refractive index of the crystal in the SLM. This image is read out with a collimated beam in the Fabry-Perot amplitude modulation mode. This beam is then imaged by a second lens system to generate the spatial power spectrum of the original image. This power spectrum is divided by the mirrored aperture into its DC and higher frequency components. These two signals are detected by diodes or PMTs and the resulting outputs divided to yield the error signal for the servo loop. If the various modes are dithered at different frequencies, and a synchronous detector is used for each of these modes, it will be possible to update all modes simultaneously. This approach to the MODS system eliminates the need for a super-fast processor to do the FFTs.

With either approach, the remaining parts of the MODS system are not computationally demanding and may be fairly directly



MODS USING SLM

Figure 49. Schematic representation of MODS system implemented with optical processing to compute PPSI.

implemented. It seems, therefore, that it is within the realm of present technology to construct an operating MODS system that would achieve significant improvements in the imaging performance of solar telescopes. The MODS approach may also be applicable to other problems involving imaging of extended, low contrast sources. Because the PPSI error signal is derived from a full aperture image and is a sum of intensities, MODS is suited to comparatively low light level operation. In the case of solar imaging, bandwidths of less than 1 \AA are easily accommodated.

END

FILMED

7-85

DTIC